Towards an automated dislocation density measurement in the SEM : Benefits and limits of the R-ECCI method

Julien Gallet

Julien Gallet. Towards an automated dislocation density measurement in the SEM : Benefits and limits of the R-ECCI method. Materials. INSA de Lyon, 2023. English. NNT : 2023ISAL0017 . tel-04220639

N°d'ordre NNT : 2023ISAL0017

THESE de DOCTORAT DE L'INSA LYON,
membre de l'Université de Lyon

Ecole Doctorale N° ED34
Matériaux Lyon

Spécialité/ discipline de doctorat :
Matériaux

Soutenue publiquement le 06/03/2023, par :
Julien Gallet

Towards an automated dislocation density measurement in the SEM: benefits and limits of the R-ECCI method

---

Devant le jury composé de :

Sauvage, Xavier	Professeur	Univ. Grenoble Alpes	Président
Mussi, Alexandre	Maître de conférence	Univ. Lille	Rapporteur
Sauvage, Xavier	Professeur	Univ. Rouen	Examinateur
Perez, Michel	Professeur	INSA-Lyon	Directeur de thèse
Cazottes, Sophie	Maître de conférence	INSA-Lyon	Co-directrice de thèse
Chaise, Thibaut	Maître de conférence	INSA-Lyon	Co-directeur de thèse

Département FEDORA – INSA Lyon - Ecoles Doctorales

SIGLE	ECOLE DOCTORALE	NOM ET COORDONNEES DU RESPONSABLE
CHIMIE	**CHIMIE DE LYON** **https://www.edchimie-lyon.fr** Sec. : Renée EL MELHEM Bât. Blaise PASCAL, 3e étage secretariat@edchimie-lyon.fr	**M. Stéphane DANIELE** C2P2-CPE LYON-UMR 5265 Bâtiment F308, BP 2077 43 Boulevard du 11 novembre 1918 69616 Villeurbanne **directeur@edchimie-lyon.fr**
E.E.A.	**ÉLECTRONIQUE, ÉLECTROTECHNIQUE, AUTOMATIQUE** **https://edeea.universite-lyon.fr** Sec. : Stéphanie CAUVIN Bâtiment Direction INSA Lyon Tél : 04.72.43.71.70 secretariat.edeea@insa-lyon.fr	**M. Philippe DELACHARTRE** INSA LYON Laboratoire CREATIS Bâtiment Blaise Pascal, 7 avenue Jean Capelle 69621 Villeurbanne CEDEX Tél : 04.72.43.88.63 **philippe.delachartre@insa-lyon.fr**
E2M2	**ÉVOLUTION, ÉCOSYSTÈME, MICROBIOLOGIE, MODÉLISATION** **http://e2m2.universite-lyon.fr** Sec. : Bénédicte LANZA Bât. Atrium, UCB Lyon 1 Tél : 04.72.44.83.62 secretariat.e2m2@univ-lyon1.fr	**Mme Sandrine CHARLES** Université Claude Bernard Lyon 1 UFR Biosciences Bâtiment Mendel 43, boulevard du 11 Novembre 1918 69622 Villeurbanne CEDEX **sandrine.charles@univ-lyon1.fr**
EDISS	**INTERDISCIPLINAIRE SCIENCES-SANTÉ** **http://ediss.universite-lyon.fr** Sec. : Bénédicte LANZA Bât. Atrium, UCB Lyon 1 Tél : 04.72.44.83.62 secretariat.ediss@univ-lyon1.fr	**Mme Sylvie RICARD-BLUM** Institut de Chimie et Biochimie Moléculaires et Supramoléculaires (ICBMS) - UMR 5246 CNRS - Université Lyon 1 Bâtiment Raulin - 2ème étage Nord 43 Boulevard du 11 novembre 1918 69622 Villeurbanne Cedex Tél : +33(0)4 72 44 82 32 **sylvie.ricard-blum@univ-lyon1.fr**
INFOMATHS	**INFORMATIQUE ET MATHÉMATIQUES** **http://edinfomaths.universite-lyon.fr** Sec. : Renée EL MELHEM Bât. Blaise PASCAL, 3e étage Tél : 04.72.43.80.46 infomaths@univ-lyon1.fr	**M. Hamamache KHEDDOUCI** Université Claude Bernard Lyon 1 Bât. Nautibus 43, Boulevard du 11 novembre 1918 69 622 Villeurbanne Cedex France Tél : 04.72.44.83.69 **hamamache.kheddouci@univ-lyon1.fr**
Matériaux	**MATÉRIAUX DE LYON** **http://ed34.universite-lyon.fr** Sec. : Yann DE ORDENANA Tél : 04.72.18.62.44 yann.de-ordenana@ec-lyon.fr	**M. Stéphane BENAYOUN** Ecole Centrale de Lyon Laboratoire LTDS 36 avenue Guy de Collongue 69134 Ecully CEDEX Tél : 04.72.18.64.37 **stephane.benayoun@ec-lyon.fr**
MEGA	**MÉCANIQUE, ÉNERGÉTIQUE, GÉNIE CIVIL, ACOUSTIQUE** **http://edmega.universite-lyon.fr** Sec. : Stéphanie CAUVIN Tél : 04.72.43.71.70 Bâtiment Direction INSA Lyon mega@insa-lyon.fr	**M. Jocelyn BONJOUR** INSA Lyon Laboratoire CETHIL Bâtiment Sadi-Carnot 9, rue de la Physique 69621 Villeurbanne CEDEX **jocelyn.bonjour@insa-lyon.fr**
ScSo	**ScSo*** **https://edsciencessociales.universite-lyon.fr** Sec. : Mélina FAVETON INSA : J.Y. TOUSSAINT Tél : 04.78.69.77.79 melina.faveton@univ-lyon2.fr	**M. Bruno MILLY** Université Lumière Lyon 2 86 Rue Pasteur 69365 Lyon CEDEX 07 **bruno.milly@univ-lyon2.fr**

*ScSo : Histoire, Géographie, Aménagement, Urbanisme, Archéologie, Science politique, Sociologie, Anthropologie

Remerciements

Durant ces trois années de thèse, j'ai eu l'occasion de rencontrer de nombreuses personnes qui m'ont aidé soit en me prodiguant des conseils en me soutenant au cours de cette expérience autant scientifique qu'humaine.

Il me serait difficile de commencer ses remerciements sans parler avant tout de Sophie Cazottes, qui m'a parfaitement encadré et conseillé lors de la réalisation de ce projet et sans qui il n'aurait jamais pu atteindre l'avancée qu'il a aujourd'hui. Elle a toujours su m'écouter et m'aider peu importe le problème que je pouvais rencontrer. Je souhaite également remercier Michel Perez pour ces longues discussions sur la microscopie électronique, pour son aide et son savoir-faire et pour m'avoir permis de prendre le recul nécessaire sur toutes les notions complexes que j'ai eu à traiter. J'ai également pu avoir de longues discussions avec Thibaut Chaise que je remercie aussi, qui a toujours su prendre le temps pour m'écouter et m'expliquer les détails sur la mécanique des matériaux mais également pour le recul qu'il m'a apporté sur le concept de dislocation et leur place dans le domaine des matériaux et dans les modèles mécaniques. A eux trois, ils m'ont guidé et ce document peut être lu aujourd'hui grâce à eux.

Je tiens également à remercier les membres du jury qui ont accepté de prendre du temps pour évaluer mon travail en participant à ma soutenance et d'enrichir les résultats via les remarques et questions qu'ils ont apporté durant nos échanges. Je remercie plus particulièrement Alexandre Mussi qui m'a transmis sa passion et son intérêt pour la microscopie des dislocations.

Le laboratoire MATEIS a su m'accueillir et j'ai pu y rencontrer de nombreuses personnes qui m'ont toutes aidé. Tout d'abord, un grand merci à Cyril Langlois, qui m'a formé au MEB et sur les méthodes d'acquisition et de traitement de données CHORD. Je tiens également à souligner l'aide précieuse apportée par Thierry Douillard, qui a toujours été disponible pour m'expliquer les subtilités des microscopes et qui m'a souvent aidé à faire face aux différents problèmes techniques que je rencontrais durant les acquisitions. Sans lui, les différentes images obtenues au MEB seraient de moins bonne qualité. Plus généralement, j'aimerais remercier les différentes personnes qui m'ont apporté leur aide technique à différents moments de ce projet. Je remercie notamment Kader pour sa réactivité et son efficacité lorsque j'avais besoin de faire usiner des pièces et Bérangère Lesaint pour les divers conseils et formations qu'elle m'a donnés sur la préparation d'échantillon mais aussi pour les discussions qu'on a pu avoir.

Je tiens également à remercier les doctorants qui m'ont précédé, notamment Clément Lafond et Gabriel L'hôte. Je les remercie tout d'abord pour leurs travaux, sans lesquels cette thèse n'aurait pas pu naître, mais également pour leurs conseils et leur aide durant ces trois années. Je voudrais également remercier Ronan Henry sur qui j'ai pu compter pour me guider et conseiller au sein de l'équipe SNMS. Il serait difficile de remercier les doctorants sans parler d'Akkiz et de sa joie de vivre, toujours prête à écouter et à discuter de tous les sujets possibles. Ta présence nous a manqué durant cette dernière année.

Merci à tous les doctorants de ma promotion, notamment à Romain pour avoir partagé mon bureau et cette aventure avec ses doutes et ses difficultés, pour nos discussions sur tous les problèmes que l'on rencontrait. Nos échanges m'ont souvent permis de trouver les solutions appropriées. J'ai pu également compter sur le soutien indéfectible de Justine au sein de l'équipe METAL et de nos longues discussions sur nos projets respectifs et sur l'aquarium de son bureau.

Je voudrais aussi adresser un remerciement plus général à l'ensemble des équipes SNMS et METAL, notamment Lucian Roiban pour ses blagues et sa joie de vivre ainsi que Philippe Steyer pour sa bonne humeur lorsqu'on le croisait dans les couloirs de SNMS. Merci également à tous ceux que j'ai pu croiser dans la salle café de l'équipe METAL et à tous ceux que j'aurais omis de citer.

Pour finir, je tiens à remercier ma famille et mes proches qui ont su être à l'écoute et qui m'ont permis de venir faire cette aventure dans la chaleur étouffante du Sud et bien loin des températures du Nord que je chérie tant. Mais je tiens à conclure ces remerciements par la personne la plus importante pour moi, Lynda, qui a accepté de tout abandonner pour me suivre si loin, qui a su m'épauler et me supporter durant toutes ces années de thèse, avec les fous rires qu'on a pu partager mais également le stress et les inquiétudes que la thèse engendrait.

Merci.

Résumé en français

Afin de prédire le comportement mécanique des matériaux métalliques, il est important de déterminer plusieurs quantités physiques, dont la densité de dislocation qui a un impact majeur sur les propriétés mécaniques. Des travaux récents ont montré qu'il est possible de réaliser ces observations à l'aide d'un microscope électronique à balayage. En effet, cette méthode a l'avantage d'être appliquée sur des échantillons massifs et de permettre l'observation de plus grandes surfaces. Cependant, une étape d'orientation de l'échantillon est nécessaire, et le traitement de l'image est réalisé manuellement. Cela rend l'approche longue et fastidieuse. La méthode R-ECCI est basée sur l'acquisition d'une série d'images à différents angles de rotation et permet d'éviter l'étape d'orientation de l'échantillon. Un profil d'intensité est obtenu, qui est représentatif de la nature du pixel considéré (dislocation, défaut ou matrice).

L'objectif de ce projet de thèse était de développer une méthode de caractérisation automatique de la densité de dislocation, en utilisant un algorithme de type clustering appliqué sur les profils. Les images sont traitées de manière automatisée et la densité de dislocation est calculée. La première partie du projet a porté sur le développement de la méthodologie d'acquisition des images et du logiciel de traitement des données et a permis de déterminer les limites et les points forts de la méthode. Dans une deuxième partie, une comparaison quantitative avec les méthodes de mesure existantes (TEM, DRX, HR EBSD ...) a été effectuée. Outre le fait que chacune de ces méthodes ne détecte pas les mêmes populations de dislocations, des résultats complémentaires en termes de limites de détectabilité ont été obtenus. Enfin, les résultats obtenus sur un alliage connu ont été comparés à ceux obtenus par un modèle de prédiction micro-mécanique, et un bon compromis a été trouvé, ce qui permet de valider l'approche globale de R-ECCI.

Contents

Introduction

In the 1930s, E.Orowan, M.Polnyi and G.Taylor [TAY 34] put forward the idea that topological defects, called “dislocations‘’, were responsible for the deformation in crystalline materials. This theory was confirmed experimentally by P.B. Hirsch in the 1950s with the first observation of dislocations with a Transmission Electron Microscope (TEM) [HIR 70]. The study of dislocations and their physical properties, especially their density, is an important step in understanding the mechanical properties of materials. Indeed, plasticity is generated by the movement of dislocations through a material under stress. During the deformation of a material, the number of dislocations increases and the deformation flow, driven by the movement of these dislocations, is blocked. Indeed, all dislocations interact with each other and eventually stop when their number becomes too large. When this density of dislocations increases sufficiently for all dislocations to become immobile, cracking or rupture phenomena appear. Therefore, in addition to being a scientific challenge, the study and observation of dislocations is also an industrial challenge.

Mechanical models capable of reliably and accurately predicting the behavior of metal parts during their life cycle represent a considerable advance for any materials-related industry. During the manufacturing process of metallic parts, whether they are destined for aeronautics, nuclear or building industries, they undergo numerous mechanical and/or thermal transformations. These different transformations will have an impact on the microstructure and especially on the dislocation density. The dislocation density will affect the mechanical properties of the material such as yield strength, work hardening, toughness, *etc.* Although the dislocation density is an important microstructural value for mechanical models, it is also one of the most difficult values to measure accurately.

Traditional methods for the measurement of the dislocation density are X-Ray Diffraction (XRD), Electron BackScattering Diffraction (EBSD) or Transmission Electron Microscopy (TEM). However, these methods have limitations. For TEM, the samples undergo several modifications during preparation in order to reach a thickness small enough for the electrons to pass through (in the order of ten nm). There are several processes to do this: crystal growth on a substrate that is then removed (chemically or mechanically) or a mechanical reduction of the thickness from a bulk material. In most cases, it is necessary to carry out an additional treatment (ion bombardment, chemical or electrolytic polishing) in order to obtain the largest possible observable area (several microns). These different transformations make it difficult to prepare the samples.

From EBSD orientation maps, the dislocation density can calculated using the disorientation angles between neighboring pixels This method can be performed on bulk samples. However, it only considers dislocation clusters with a non-zero resultant Burgers vector, and the obtained results are very dependant on the pixel size chosen to realize the mapping. Therefore, some of the information on the real dislocation density can be lost. The High-Resolution method

(HR-EBSD) limits this loss of information by calculating the disorientation directly from the Electron Back-Scattering Patterns (EBSP) obtained during the acquisition of the maps. This method has shown a better accuracy than the classical EBSD.

For X-ray diffraction (XRD), the calculation of the dislocation density is based on the broadening of the diffraction peak due to the presence of dislocations and stacking faults. Although this method uses bulk materials that do not require destructive processing like TEM or SEM, it still has drawback: the lower the dislocation density, the more difficult it is to determine it accurately. This is rather problematic for mechanical models, as they mainly require a description of the initial dislocation density (before deformation), for which the XRD measurement uncertainties are rather high.

Another possibility for dislocation observation consists in using a Scanning Electron Microscope (SEM), in the Electron Channeling Contrast Imaging mode (ECCI). A first advantage of the SEM-ECCI is that it is realized on a bulk sample. It is therefore possible to observe them at different stages of deformation, and thus achieve a monitoring of the thermomechanical history of the material. The second advantage of this observation technique is that it allows to study a larger area than using TEM. It is therefore possible to analyze several grains of different orientations and thus obtain a more representative value of the density of dislocations in the material. However, this method requires a careful orientation of the sample so that the dislocation can be visible. As this orientation step is quite tricky and time consuming, recent developpement were performed at MATEIS laboratory, and later called R-ECCI [L'H 19] for Rotationnal ECCI. Many images are recorded during the rotation of the sample, from which images in suitable conditions for dislocation imaging can be found. Moreover, a dedicated software was developed to perform an automatic dislocation detection on the obtained image stack. The first results indicate that it should allow a better imaging of deformed samples.

However, all the methods mentioned so far measure the dislocation density with a specific uncertainty. Additionally, the measured densities are of different nature and acquired under different conditions, on samples having undergone different transformations. This makes their interpretation and comparison difficult. Finally, for the newly developped R-ECCI, no comparison with existing methods has ever been realised. It is therefore necessary to first define the scope of this method, the type of material and the level of deformation that can be characterized and secondly to define the uncertainties of the R-ECCI method.

The first objective of this thesis is to improve the R-ECCI method and to adapt it to deformed materials. Moreover, it is necessary to define the accuracy and uncertainties related to the measurement method (observed volume, overlapping dislocations, apparent thickness of dislocations).

The second objective is to compare the R-ECCI clustering method with already existing and commonly used methods for dislocation density measurements (TEM, EBSD, XRD).

The third objective of this thesis is to compare the R-ECCI method with an existing mechanical model in order to evaluate the contribution of the method compared to the predictive model.

This manuscript is structured around several chapters, themselves developed in different parts:

The **first chapter** is devoted to the state of the art: it summarizes what is known about the plasticity and structure of dislocations and also discusses examples of existing mechanical models as well as the observation and acquisition methods currently used.

The **second chapter** is devoted to the presentation of the clustering method, used in R-ECCI and the classification of the data processing. The detection algorithm is detailed as well as the calculation of the dislocation density. This part continues with the quantification of the various sources of uncertainty encountered and ends with an experimental characterization of the dislocation density as well as on the measurement error on duplex steel samples with different deformation levels.

A **third chapter** is devoted to an experimental determination of the volume observed in ECCI, which constitutes the main source of error of the method. A FIB thin foil was observed using TEM and ECCI observations have been performed on the same sample in order to provide answers to this uncertainty.

The **fourth chapter** aims at comparing the different traditional methods (TEM, XRD, SEM), with R-ECCI, on several duplex steel samples at different deformation states. Each method is first studied separately in order to properly define what it observed and what data can be obtained. Then, the different methods are compared between them in order to know the scope of application of each method.

A **fifth chapter** is devoted to the effect of the density measurement on the mechanical model results. The objective of this part is to use an existing mechanical model based on a theoretical calculation of the dislocation density in order to evaluate the contribution of the R-ECCI method and of clustering to this type of model.

This work was carried out as part of the DISCO (Dislocation Imaging in Scanning electron microsCOpy) project supported by the Institut Carnot Ingénierie@Lyon.

Chapter 1

State of the art: plasticity and experimental characterization

Sommaire

1.1 The Kocks Mecking Estring model for the description of deformation laws

In order to improve material properties or be able to predict the life time of mechanical parts, it is of first importance to well understand and describe the effect of microstructural parameters on mechanical behavior. This section will focus on the description of microstructural-based models for predicting stress-strain curves.

1.1.1 Concept of plasticity and dislocation in metals

From an uniaxial tensile test, it is possible to obtain a stress/strain curve. Figure 1.1 shows an example of a stress/strain curve where the transition between the elastic and plastic domains is ideal, i.e. the transition between the two domains is continuous. The parameter that separates the two domains σ_y represents the yield strength or stress to be applied to enter the plastic domain. In order to predict the behavior of materials, it is necessary to model the yield strength and the plastic domain. However, the yield strength depends on the initial dislocation density contained in the material and the strain hardening phenomenon that takes place in the plastic domain also depends on the dislocation density.

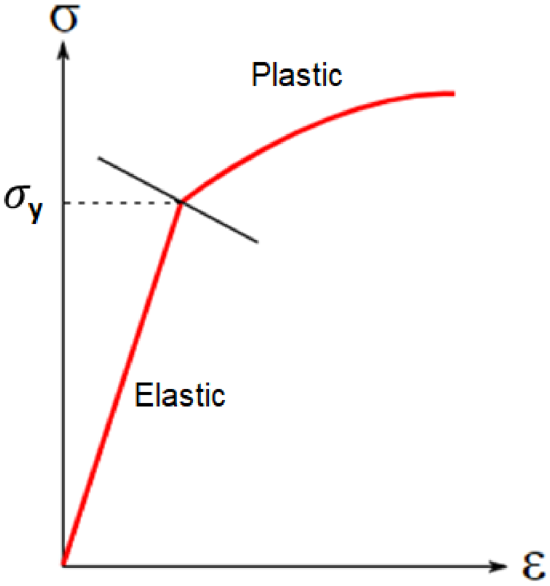

Figure 1.1: Example of “ideal” stress/strain curve with the elasic limit separating the two domains (elastic and plastic).

The non-ideal case has a transition phase between the two domains (plastic and elastic). This transition phase is necessary to allow the deformation mechanism (dislocation) to start moving.

1.1.2 Yield stress modelling

It is often observed that grain size reduction improves the plastic deformation resistance of materials. In the early 1950s, EO Hall and NJ Petch proposed a model describing the influence of grain size reduction on the yield strength of metals, which led to the formula of Hall-Petch [HAL 51a] [PET 53b]:

$$\sigma_y = \sigma_0 + k_1 D_{GB}^{-1/2} \tag{1.1}$$

σ_0 is an original frictional stress that considers the Peierls-Nabarro force and the contribution of dislocations, D_{GB} is the grain size, σ_y the yield stress and k_1 is a constant that can be considered as a measure of the resistance to dislocation motion. k_1 is to be distinguished from the lattice friction. It represents here the interference of dislocations with potential impurities or the change of orientation near the grain boundaries or sub-grain boundaries.

Subsequently, many studies have developed physical models to reproduce the hardening mechanism [DEL 07] [SIN 06b]. These studies have shown that the grain size and dislocation density are important parameters.

In order to make the dislocation density appear, it is possible to consider the flow stress σ_f as a function of the plastic strain such that:

$$\sigma_f(\varepsilon_p^f) = \sigma_0^f + \sigma_R^f + \sigma_X^f \tag{1.2}$$

With ε_p^f the plastic deformation, σ_0^f the sum of the Peierls force and frictional stress contributions related to the alloying elements in solution. σ_R^f is the isotropic hardening (or forest dislocation hardening) and depends on ρ_f, wich is the density of Statistically Stored Dislocations (SSD) contained in the ferrite (1.4). σ_X^f is the kinematic hardening generated by the density of Geometrically Necessary Dislocations (GND) created during deformation (1.5).

σ_R^f and σ_X^f are defined as:

$$\sigma_R^f = \alpha_T M_T \mu b_{111} \sqrt{\rho_f} \tag{1.3}$$

$$\sigma_X^f = \frac{M_T \mu b_{111}}{D_\alpha^0} n^f \tag{1.4}$$

Where α_T is the forest hardening coefficient, M_T is the Taylor factor, μ is the elastic shear modulus, b_{111} is the burger vector (other possible directions of the burger vector are neglected), D_α^0 is the initial ferrite grain size and n^f is the average number of GND-type dislocations accumulated to accommodate the deformation.

1.1.3 Plastic deformation: Strain hardening vs restoration

In 1934, G.I Taylor [TAY 34] introduced the term “dislocation” to explain the discrepancy between experimental observations and calculated values of the minimum stress to apply to deform a material. A dislocation is a linear defect that is set in motion by a force applied to the crystal, the crystal is then sheared and the atomic rows that compose it moves gradually. A dislocation is defined by two vectors, the Burgers vector $\vec{b}$, which represents the amplitude of the deformation and its direction and the line vector $\vec{u}$, which defines the direction of the dislocation line (see Appendix A.1: Plastic deformation and the concept of dislocation).

When the dislocations move in the crystal, they will interact with each other and several phenomena can occur. One of them is the annihilation of dislocations. When two identical dislocations with opposite burgers vector $\vec{b}$ will meet, their respective stress field cancel and restore the structure of the material without deformation (see figure 1.2R). Another possibility is that the dislocation finds itself “blocked” by what are called “pinning” points. The dislocation continues to move while keeping its pinning points immobile, it bends and continue to propagate, until a loop will come off, leaving behind a small segment, which will return to its initial position (from steps 5 to 6 in figure 1.2). This small segment will therefore start again to bend under the applied external stress σ’, and thus multiply the dislocation loops present in the material. The segment between two pinning points is called a “Frank-Read source” [FRA 50]. These sources of dislocation are one of the main causes of work hardening in materials.

The dislocation density ρ, is defined by

$$\rho = \frac{L}{V} \tag{1.5}$$

Where L is the total line length of dislocations in a volume V.

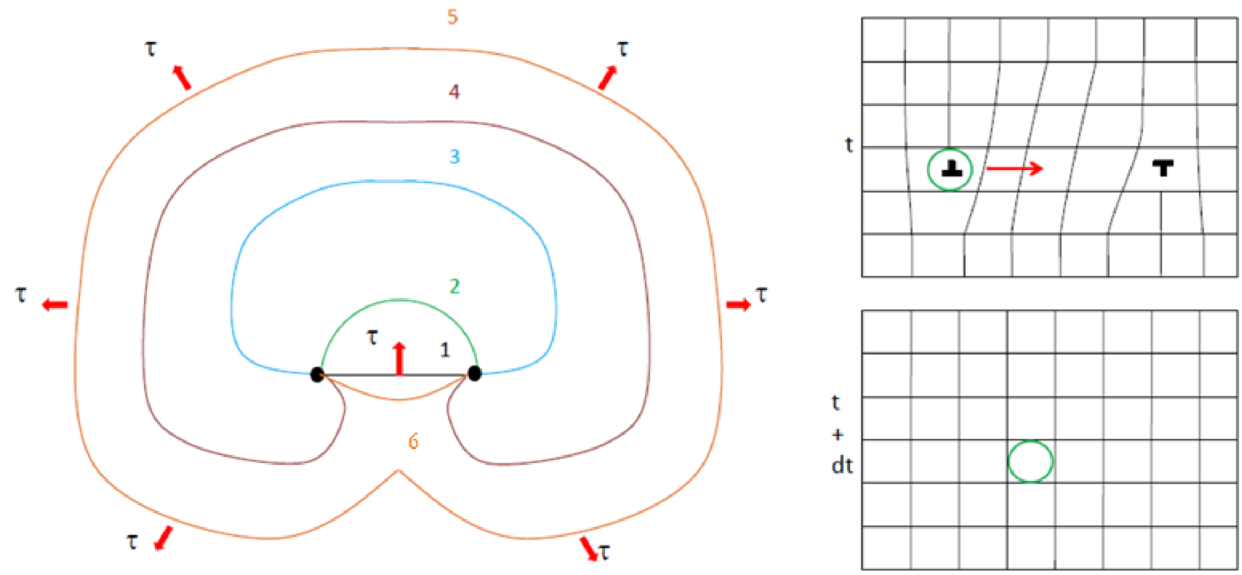

Figure 1.2: Frank-Read source (left) and annihilation of dislocation (right) [BAR 14].

Two opposites phenomenons might occur during plastic deformation, the first one corresponds to the strain hardening, through the increase of dislocation density, and the second one being the restoration, corresponding to the annihilation of dislocation, and therefore the diminution of the dislocation density.

As the displacement of a dislocation is of the order of the lattice parameter, it is considered as low compared to the size of the crystal, if the deformation is small it is possible to write:

$$\tan(\gamma_p) \approx \gamma_p \tag{1.6}$$

With γ_p is the angle of shear, represented in Figure 1.3. We introduce then the dislocation density:

$$\gamma_p = \frac{b}{h} = \frac{l_d}{l_d dh} = \rho db \tag{1.7}$$

With l_d the mean free path. It is then possible to describe the increase of dislocation density as:

$$\left(\frac{\partial \rho}{\partial \gamma_p}\right)^+ = \frac{1}{db} \tag{1.8}$$

The equation (1.8) is the mathematical representation of the creation of dislocations in the material during deformation. This phenomenon of dislocation creation corresponds physically to the Frank-Read sources and is opposed to the restoration phenomenon represented by a term called annihilation.

This corresponds to the fact that two dislocations can cancel each other during the deformation, if they have an opposite Burgers vector b. This phenomenon is proportional to the

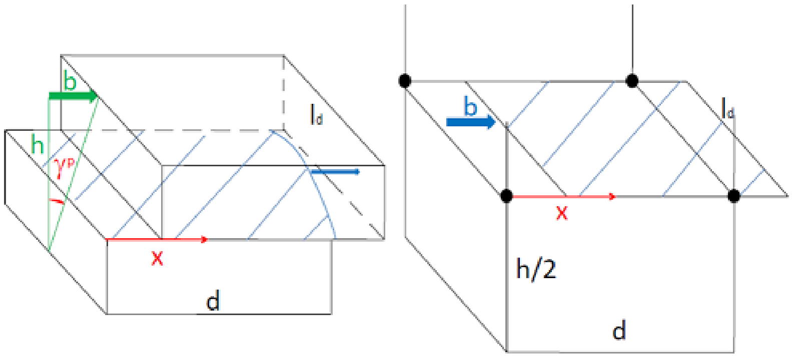

Figure 1.3: Crystal sheared by the movement of a dislocation. (a) full view of the crystal (h is the height of the crystal), γ_p is the angle of shear, b the Burgers vector, d the length of the crystal and l_d the mean free path. (b) zoom on the lower part of the crystal [BAR 14].

dislocation density and is independent of the previous event. The restoration rate $\frac{\partial \rho}{\partial t}$ is then a quadratic function of the dislocation density and if we couple it to the Orowan equation $d\gamma_p = \rho.b.v.dx$, the restoration term becomes [BAR 14]:

$$\left(\frac{\partial \rho}{\partial \gamma_p}\right)^- = \frac{\partial \rho}{\partial t}\frac{\partial t}{\partial \gamma_p} = k_2 \rho \tag{1.9}$$

Where k_2 is an efficiency factor of restoration that depends on temperature.

Kocks-Mecking and Estrin (KME) developed a model to describe both combined effects of restoration and strain hardening [EST 96] [KOC 03]. The total evolution of dislocation density with deformation can be written as:

$$\frac{\partial \rho}{\partial \gamma_p} = \left(\frac{\partial \rho}{\partial \gamma_p}\right)^+ - \left(\frac{\partial \rho}{\partial \gamma_p}\right)^- \tag{1.10}$$

This model shows the importance of the dislocation density in the material and the consequences of its evolution during deformation. These two terms are in competition: when one will deform the material, the Frank-Read sources will increase the dislocation density and therefore the hardening of the material will increase.

However, this increase in density will cause more frequent restoration phenomena. When the dislocation density in the material increases, the energy stored is more important. At a certain temperature about 0.6 times the melting temperature of the material, the thermal agitation of the atoms is sufficient to allow the dislocations in the material to reorganize and annihilate each other [SAK 88]. The sliding of dislocations does not imply the addition of matter, but the thermally activated phenomenon known as dislocation climb requires that there is diffusion of matter [TOL 07]. The mechanism behind the dislocations climb is the attraction of vacancies or interstitial defects. This climb phenomenon is one of the most important deformation mechanisms in the field of plasticity because it allows dislocations to change their slip plane and therefore to overcome obstacles. Therefore, the dislocations annihilate easier. The main driving force of the different restoration types is the decrease in the energy stored in the material, linked to the decrease in the dislocation density.

These phenomena are sensitive to temperature but also to the deformation rate. For example, Blaizot *et al.* [BLA 16] have shown that the strain rate (Figure 1.4, (a)) has little influence on the elastic limit but it significantly influences the work hardening over the ranges of rate and temperature presented here. There is also note the appearance of a steady sate more quickly for a slower strain rate, for example at 205 MPa for a speed of 10^{-4} s^{-1} against a stress of 435 MPa for a speed of 5×10^{-3} s^{-1}.

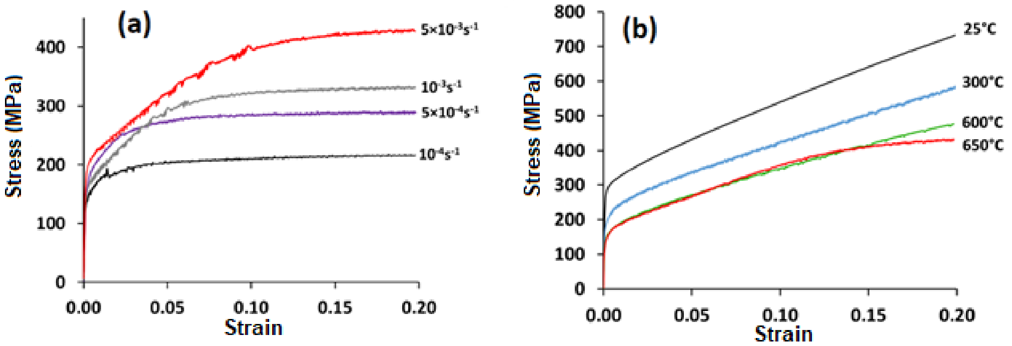

Figure 1.4: Stress-Strain curve of a nickel-based alloy (NY690) as a function of the strain rate at 750°C (a) and as a function of temperature with a strain rate $10^{-4}s^{-1}$ (b) [BLA 16]

In the case of nickel-based alloys observed by Blaizot [BLA 16] the temperature, on the other hand, influences the elastic limit but also the work hardening which is linear at low temperature for this nickel-based alloy (Figure 1.4 (b)). At 650°C, we notice the appearance of the stationary deformation regime. For this temperature (and higher temperatures), this appearance shows that the mechanisms of structure restoration (climb dislocation, annihilation...) started to activate. That activation slows down the hardening [VEN 98].

1.1.4 Dislocation types in metallic materials

Dislocation in polycrystalline materials can usually be found either isolated, randomly distributed inside the cells or grains, or localized close to grain boundaries to accommodate possible strain incompatibilities between the different grains. Other dislocations are found to be organized into patterns, in the form of dislocation cells or walls.

Therefore the total dislocation density ρ_{tot} is often decomposed as [BOR 00][WAU 15]:

$$\rho_{tot} = \rho_w + \rho_c + \rho_{GB} \tag{1.11}$$

with ρ_w the density of dislocations constituting the cell walls, ρ_c the dislocation density randomly distributed within the cells/grains and ρ_{GB} the dislocation density present at grain boundaries.

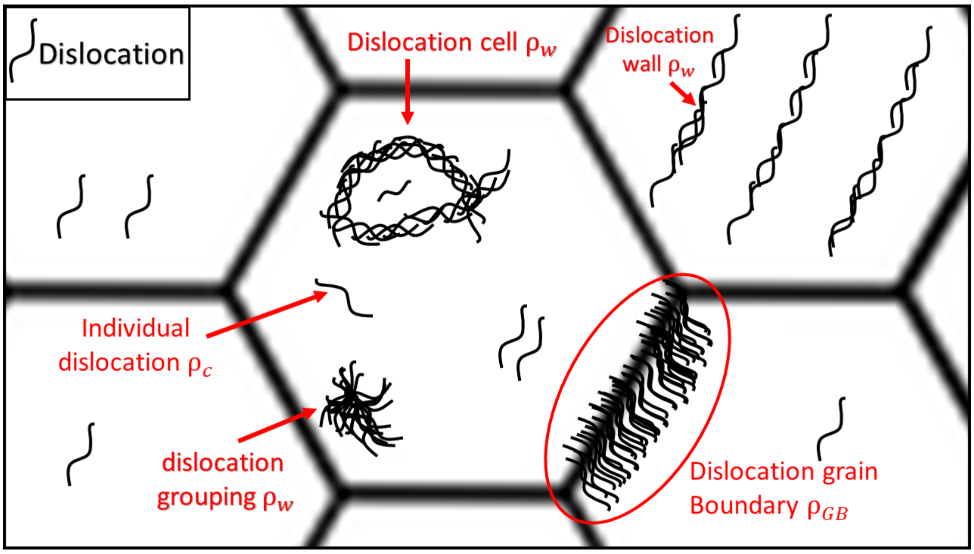

Figure 1.5: Diagram of the different arrangements of dislocations in a material

Another description of dislocation is often given, namely Geometrically Necessary Dislocations (GND) and Statistically Stored Dislocations (SSD), as presented by Nye [NYE 53], Cottrell [COT 64] and Ashby [ASH 70]. GNDs play an important role in the strengthening effects of alloys [VEN 98][BOR 00]. They are related to the deformation gradients due to the geometric constraints of the crystal lattice. These "same-sign" dislocations induce lattice curvature, or local misorientation, and represent dislocations located at grain boundaries or at cells walls so that the total amount of GND can also be expressed as $\rho_{GND} = \rho_w + \rho_{GB}$. On the other end, SSDs are stored due to an accumulation process - they trap each other randomly and do not produce significant disorientation [HUG 03]. Those dislocations represent the randomly distribution dislocation, described by ρ_c. Hence, the total dislocation density is often rewritten simply as:

$$\rho_{tot} = \rho_{GND} + \rho_{SSD} \tag{1.12}$$

In terms of mechanics, GNDs are often not very mobile as they are forming cells, or structures or dislocation pile ups. Therefore, their contribution to deformation is not important, and they contribute more to strain hardening. On the other hand, SSD are quite mobile and should be the one responsible to plastic flow. The difference in dislocation type is however not always taken into account in the modelling. Yet, in given material, for a given deformation level, the difference in SSD and GND density can be of more than a decade [ZHE 15] [ZHI 20]. It is therefore of importance to evaluate the errors generated by a wrong description of the dislocation population in mechanical models.

Several methods can be used to measure dislocation densities in materials. Some of them will mostly measure SSD's dislocation density while other will be more sensitive to the presence of GND's. The next section will describe some of those measurement techniques.

1.2 Characterization of Dislocation density

TEM and SEM can be used to observe dislocations, and later measure dislocation densities. In this section several methods of measuring dislocation density will be discussed (intercept and N/S) as well as the method of orienting the sample to observe dislocations will be described for SEM and TEM.

1.2.1 Traditional measure of density dislocation with image analysis

To measure the dislocation density from TEM or ECCI images, the most common used method is the intercept method [HAM 61] [BRA 70a]. It consists in drawing lines on a TEM (artitrary lines or regular grid) image and counting the number of intersections n with dislocations (Figure 1.6) with the formula:

$$\rho_{tot} = \frac{2n}{lt} \tag{1.13}$$

With t the analyzed thickness, l the total length of the lines drawn.

Moreover, the knowledge of the analyzed depth is essential for the intercept method. For TEM, the analysed depth corresponds to the thin foil thickness and can relatively easily be measured (see next section). In the case of ECCI, where bulk materials are used, it is more difficult to estimate this depth and this can lead to a significant uncertainty (see next section).

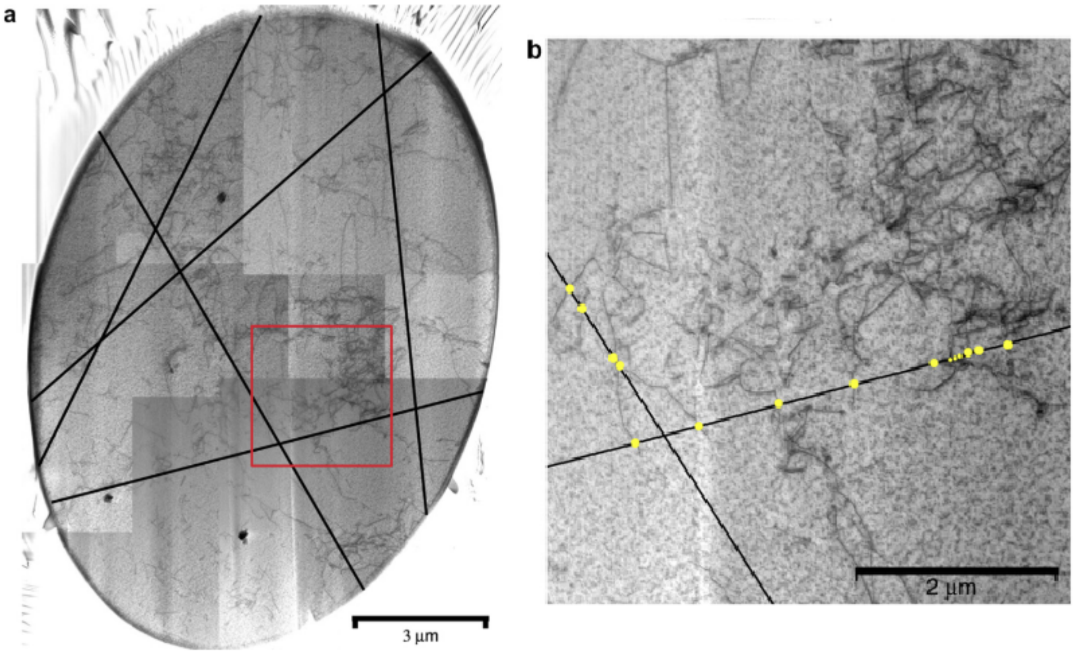

Figure 1.6: Example of one of the procedures used for dislocation density measurements, the line-intercept method: (a) random lines are superimposed on a Scanning in TEM (STEM) image taken from a deformed 10 μm diameter microsample; (b) marks are placed at each point where dislocation intersects a line, by D.M. Norfleet *et al.* [NOR 08]

Another possibility can be used on dislocation images (also applicable on ECCI imaging at SEM). It consists in manually counting the number N of dislocations visible on the image and dividing by the area S of the image.

However, neither the N/S method and the intercept method do consider the orientation of dislocations relative to the sample surface, which could lead to large measurement uncertainty. This will be later discussed in Chapter 2.

As a consequence, dislocation density can be efficiently measured from TEM images if it does not exceed 10^{14-15} m^{-2} [MEN 21]. Indeed, beyond this value, it becomes difficult to distinguish precisely the number of dislocations present at the intersection with the grid. Moreover, correctly distinguishing one dislocation from another requires high magnification images and therefore small analyzed areas, which might not be Representative of the whole material. In this case, multiplying the analyzed areas is always possible but will dramatically increase the data processing time.

In the case of ECCI, the field of view and the spatial resolution are different. Therefore, it is necessary to determine the limits of the characterizable minimum and maximum densities.

The principles for dislocation imaging are detailed below:

1.2.2 Transmission Electron Microscope

In 1931, Max Knoll and Ernst Ruska developed the electromagnetic lens to focus electrons [RUS 31]. This method is the basis of the Transmission Electron Microscope (TEM). It is a technique that uses high-energy electrons (with acceleration voltages generally 200 kV but which can range from 60 to 400 kV). This method allows to image thin objects (with a thickness of the order of a hundred nanometers). Compared to conventional optical microscopy using visible spectrum light, the electrons have a shorter wavelength and the electron microscopy gives a better resolution. However, due to aberrations (spherical, chromatic or astigmatism), the resolution of electron microscopes moves away from its theoretical value, defined by the De Broglie wavelength of electrons (0.00251 nm for electrons accelerated to 200 kV). In general, transmission electron microscopes have a resolution of around 1 Å.

1.2.2.1 Orientation condition

Electron diffraction in a transmission electron microscope (TEM) was first performed by Kossel and Möllenstedt in 1939 [KOS 39] and now has an indispensable place in their use. This is because the observation of dislocations with TEM is based on the diffraction of the different crystal planes according to Bragg conditions (see Appendix B). The Bragg conditions do not need to be perfectly respected, the relaxation of the Bragg conditions makes it easy to obtain diffraction images even if one slightly moves away from these conditions.

The diffraction phenomenon is discrete, therefore, the different diffraction spots (see appendix B: Notion of diffraction) that appear in the focal plane of the objective lens and can be filtered out. It is then possible to use a diaphragm to isolate either the transmitted spot or one of the diffraction spots. By isolating the transmitted spot, all the elements that have diffracted the beam will appear dark in the image plane, these images acquired in this condition are called Bright-Field (BF) images (Figure 1.7a). It is also possible to make so-called Dark-Field (DF) images (Figure 1.7b). This method consists in placing the diaphragm on a diffraction spot instead of the transmitted spot. The resulting image will show in white the elements that were diffracted under the same conditions as the diffraction spot isolated by the diaphragm.

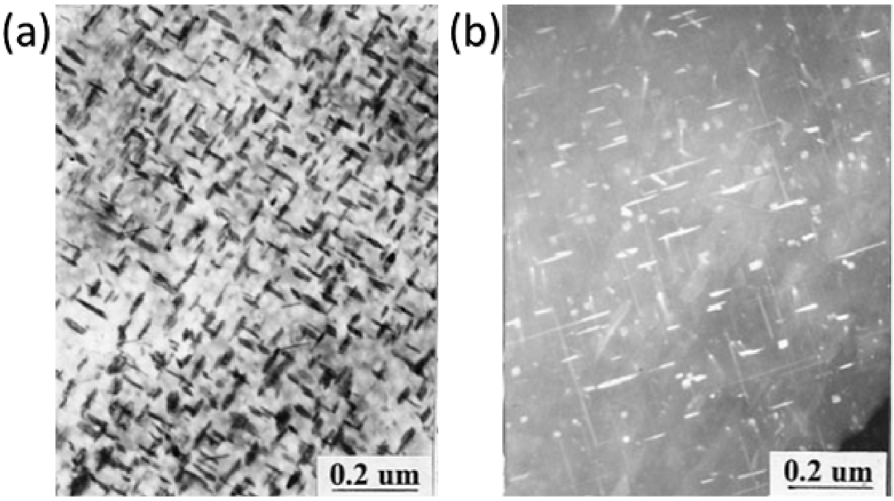

Figure 1.7: (a) Image obtained under Bright-Field (BF) conditions and (b) Dark-Field (DF) conditions [HUA 98]. Image obtained in an alloy of Al-4.0Cu-0.3Mg-0.4Ag. In Bright Field mode, the transmitted beam is selected, while in Dark Field mode a diffraction pattern is selected. In this case the diffraction spot of the precipitates was selected, the precipitates appear white, and the matrix dark.

In the context of dislocation imaging, it is necessary to proceed differently. Indeed, the dislocations do not give rise to any additional diffraction spots. However, the local curvature of the crystal planes surrounding the dislocation line (Figure 1.8) modifies the diffraction conditions around the dislocations, and might generate a contrast.

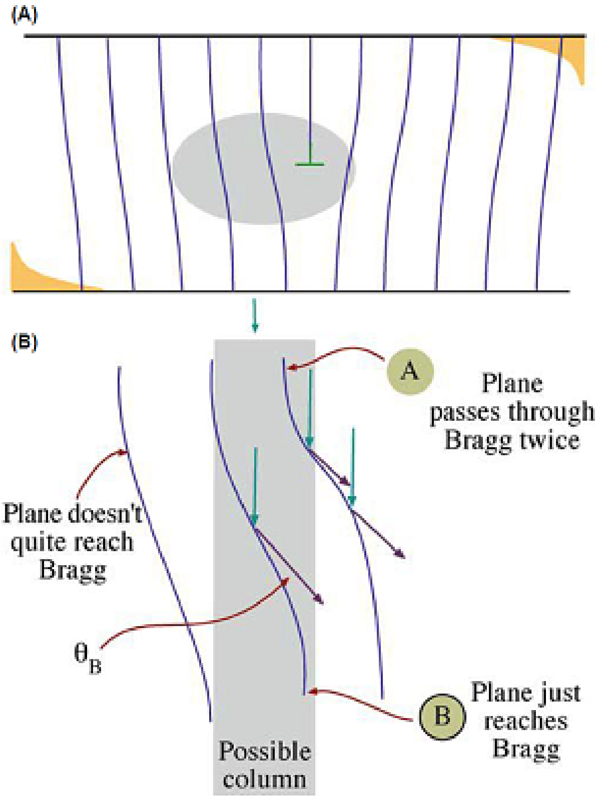

Figure 1.8: (B) zooms in on the area near the heart of the dislocation, in grey on image (A) [WIL 96]

In order to image the dislocations, the crystal is oriented so that only one family of planes diffracts. By moving slightly away from the Bragg diffraction conditions, it is possible to switch from a diffraction pattern containing all the diffraction spots (Figure 1.9(a)) to a "Two Beam‘' (TB) condition. This condition reveals only one family of planes (Figure 1.9(b)) and allows to separate the information.

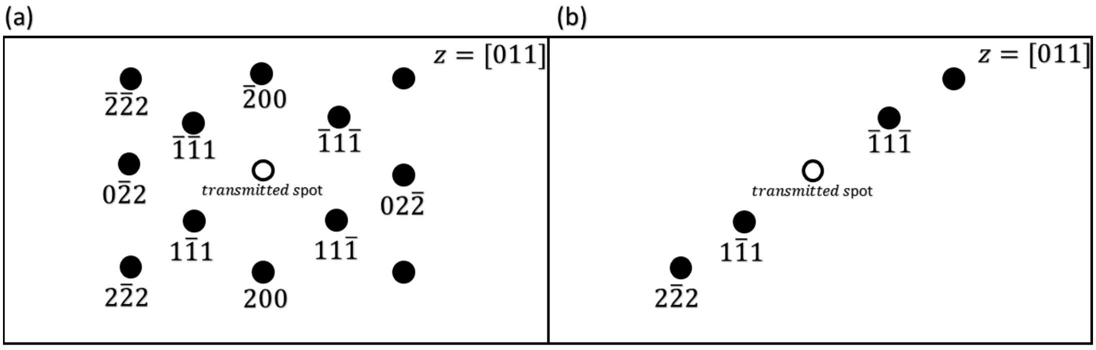

In the normal condition, several visible families

In two beam condition, just one visible family

Figure 1.9: Diagram of a diffraction pattern in normal condition (a) and in two beam condition (b).

To orientate the sample correctly, it is usual to use Kikuchi lines rather than diffraction spots. Indeed, when an electron beam interacts with a crystal, a part of the electrons will be scattered inelastically by the atoms with a small energy loss. This phenomenon creates a source point of divergent electrons under the surface of the sample. These source points scatter the electrons towards the outside of the sample and a part diffracts on the different crystal planes according to the Bragg law. This diffraction phenomenon produces cones of intensity at very large angles of aperture. These cones are so open that they are observed as two straight lines, when projected on a camera plane (Figure 1.10(a)). This phenomenon occurs for a multitude of crystal planes forming the different Kikuchi bands observed in Figure 1.10(b).

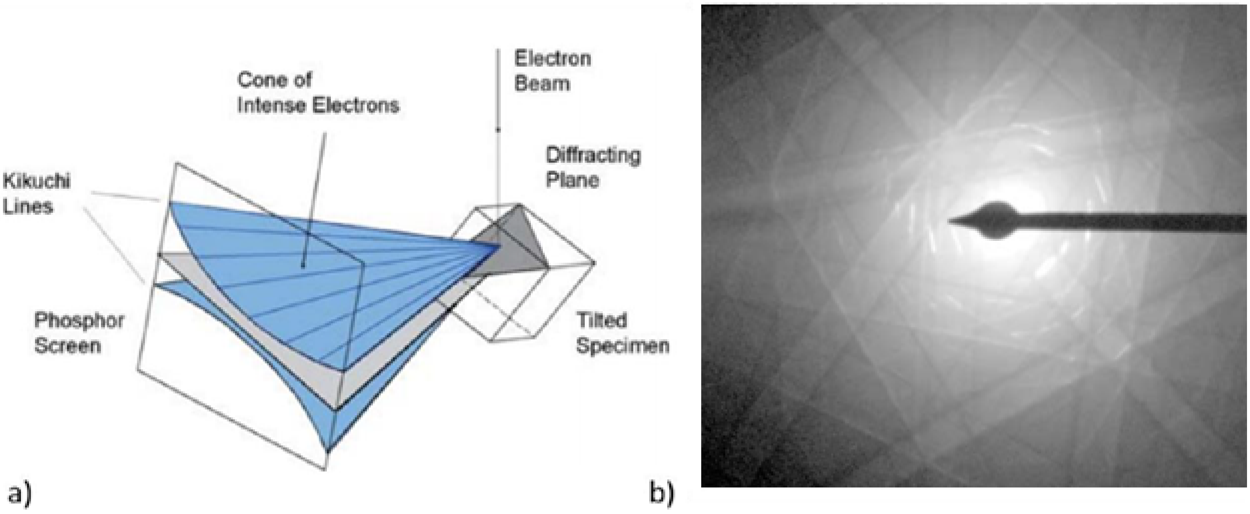

Figure 1.10: (a) Scheme of formation of Kikuchi plates [SCH 09] (b) Exemple Kikuchi plates obtained [FAR 08]

The Kikuchi bands (Figure 1.10(b)) of the same plane family intersect at different locations called “Zone Axis‘’. In order to obtain a correct image of the dislocations, it is necessary to orientate the sample in a Two Beam condition (TB) so that only one plane can be diffracted. Indeed, under normal conditions, many crystal planes can diffract at the same time, but to image dislocations with a good resolution it is necessary that only one type of plane can diffract.

The source of the Kikuchi images is the sample, so moving the sample will also move the Kikuchi bands, unlike diffraction spots which are just a deflection of the electron beam emitted by the microscope. Diffraction spots do not move with the sample but their intensity varies, appearing or disappearing depending on the position of the sample.

By moving the sample so that it is on a single Kikuchi band, only one family of planes hkl will be in the diffraction condition. The dislocation contrast between the matrix and the dislocation will be enhanced if a small deviation is added from this Bragg condition, which is called Weak Beam (WB) condition [COC 69]. In two beam condition, the Ewald sphere passes through the transmitted and the diffracted beam so that two spots are visible (Figure 1.11(a and b)). In WB mode, an even higher deviation angle allows the Ewald sphere to pass through -g and 3g nodes, and the image is performed using the g diffraction spot (Figure 1.11c and d). Its intensity is much weaker than the one of the transmitted beam, which explains the name of this mode. In that case, the diffracted intensity is much weaker (Dark field mode), but the dislocation contrast is much finer and located closer to the dislocation core than in the Two Beam mode.

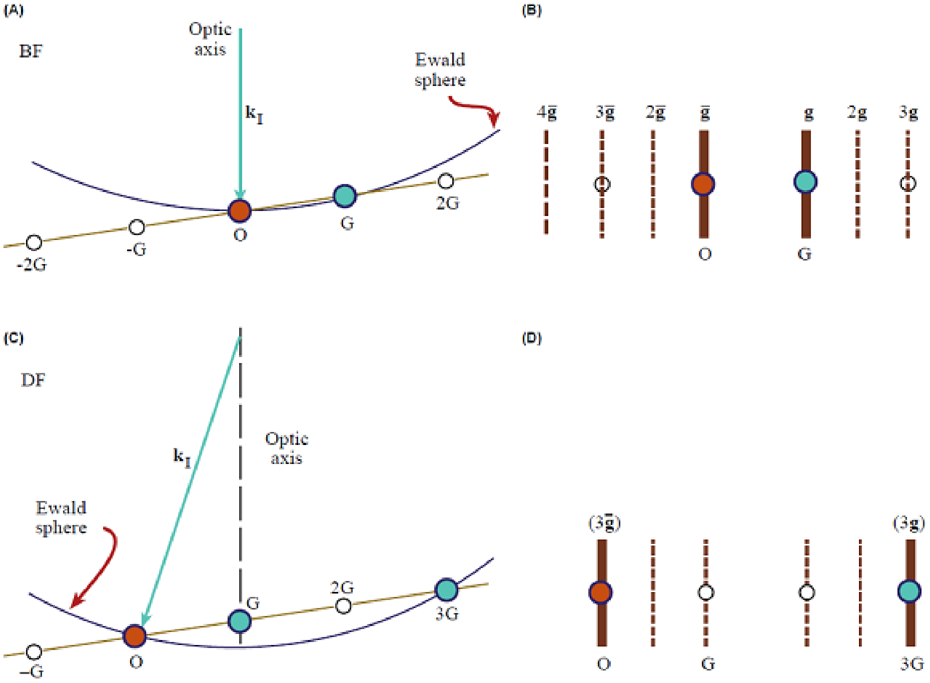

Figure 1.11: Relationship between the orientation of the Ewald sphere and the position of the Kikuchi lines for the 0(g) (A and B) and g(3g) (C and D) diffraction conditions. The two pairs of diagrams are related by tilting the beam; the specimen has not tilted so the position of the Kikuchi lines is unchanged [WIL 96]

By combining the Weak Beam and Dark Field (WBDF) methods, it is possible to obtain much finer apparent dislocation widths from about ten pixels wide to only a few pixels, as seen in Figure 1.12.

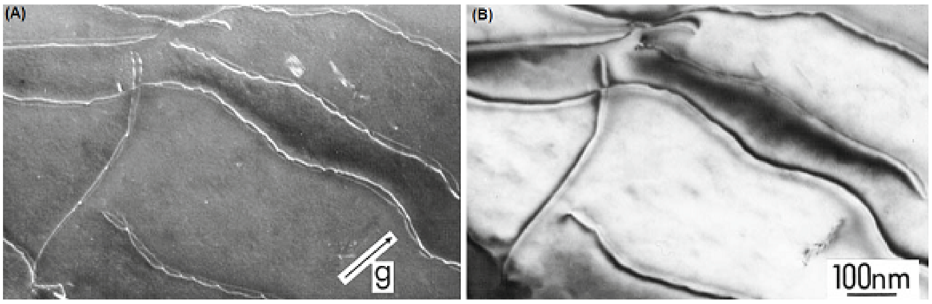

Figure 1.12: plate comparison obtained with (A) the Weak Beam Dark Field (WBDF) method and (B) the Brigth Field (BF) method [WIL 96]

It is important to note that dislocations have different diffraction conditions depending on their Burgers vector $\overrightarrow{b}$. This phenomenon, called the contrast extinction criterion [35] shows that, depending on the diffraction vector $\overrightarrow{g_{hkl}}$ chosen to make a dark-field image, a dislocation may or may not be visible. This extinction criterion is defined as:

$$\overrightarrow{g_{hkl}} \cdot \overrightarrow{b} = 0 \tag{1.14}$$

The knowledge of the thickness of the thin foil is essential for dislocation density measurements, as the analysed volume must be known for the calculation of ρ. In order to determine the sample thickness, one method is to analyze the Kossel-Möllenstedt (K-M) fringe in a converging beam electron diffraction (CBED). This allows to measure the thickness of a crystal with an accuracy of less than 2% [WIL 96][DEL 01].

This method does not require complex experimental operations or tedious theoretical analysis: it consists in measuring the spacing between the diffraction fringes, the Bragg angle, the total number of fringes n and other crystallographic values. To facilitate the calculation steps, numerical tools have been developed such as CBED tools for the Digital Micrograph software.

The sample thickness measurement is calculated from the fringes contained in the CBED disk. An example of a simulated CBED disk is shown on Figure 13. In all CBED disks, there are deviation vectors $\overrightarrow{s}$ (see appendix B notion of diffraction) for which the Bragg diffraction condition is perfectly satisfied when $\overrightarrow{s} = 0$. Variations of $\overrightarrow{s}$ in the CBED disk cause the appearance of diffraction fringes (or diffraction intensity oscillations).

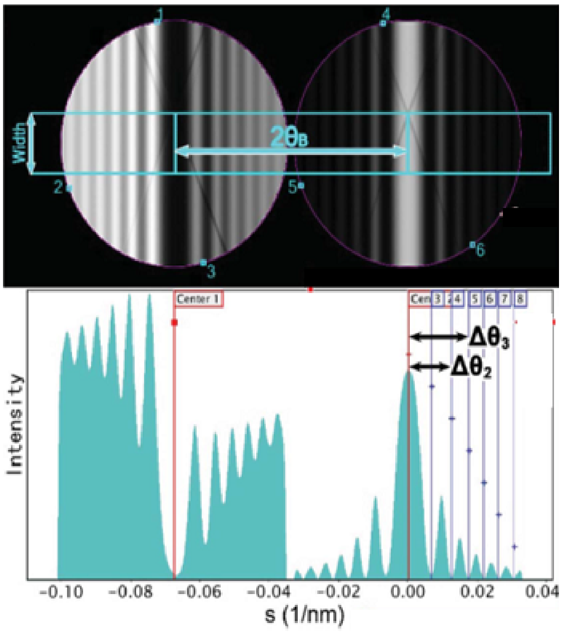

Figure 1.13: Schematic representation of the crystal thickness measurement based on the CBED technique. The top panel is a typical simulated CBED pattern and the bottom panel is a rocking curve projected from the rectangular region on the CBED pattern [HON 17]

For a crystal of constant thickness t, the intensity of the diffracted beam I_g can be written according to the condition of two beams [WIL 96]:

$$I_g(s_{eff}) = \left(\frac{\pi}{\xi_g}\right)^2 \frac{\sin^2(\pi s_{eff} t)}{(\pi s_{eff})^2} \tag{1.15}$$

With ξ_g the extinction distance for a diffraction vector $\overrightarrow{g}$ and s_{eff} is the effective deviation vector.

The intensity of the diffracted beam becomes zero $I_g(s_{eff}) = 0$ when the ith oscillation gives $s_i t =$ integer, that is:

$$\left(\frac{s_i}{n_i}\right)^2 + \frac{1}{n_i^2 \xi_g^2} = \frac{1}{t^2} \tag{1.16}$$

When plotting $(s_i/n_i)^2$ as a function of $1/n_i^2$, the ordinate at the origin gives $1/t^2$. Moreover, the slope of the curve gives a value of $1/\xi_g^2$.

The values of the deviation vector s_i associated with the peak n_i, are calculated from the CBED disk as follows:

$$s_i = \frac{\lambda \Delta\theta_i}{d^2 2\theta_B} \tag{1.17}$$

With λ is the wavelength of the incident electron beam, $\Delta\theta_i$ is the angle of the i$^t h$ fringe spacing with reference to $s = 0$, d is the hkl interplanar distance and θ_B is the Bragg semi-angle for the diffracted hkl disc. Therefore, the measurement of $\Delta\theta_i$ and θ_B are essential steps to obtain the thickness of the sample.

It is important to specify that this method of measurement gives a local thickness, this thickness can vary within the same grain. It is therefore always difficult to be precise on the average thickness of the grain (necessary data for the determination of the density).

1.2.3 Electron Channeling Contrast Imaging in Scanning Electron Microscopy

1.2.3.1 Principle

The observation of dislocations in a Scanning Electron Microscope (SEM), in Back Scattering Electron mode (BSE) is possible thanks to the phenomenon of electron channeling. This phenomenon has been predicted, from a theoretical point of view, by Hirsch and al. in 1962 [HIR 62]. It was confirmed experimentally by Coastes in 1967 [COA 67]. This phenomenon is due to the angle between the incident beam and the crystal orientation (see Figure 1.14).

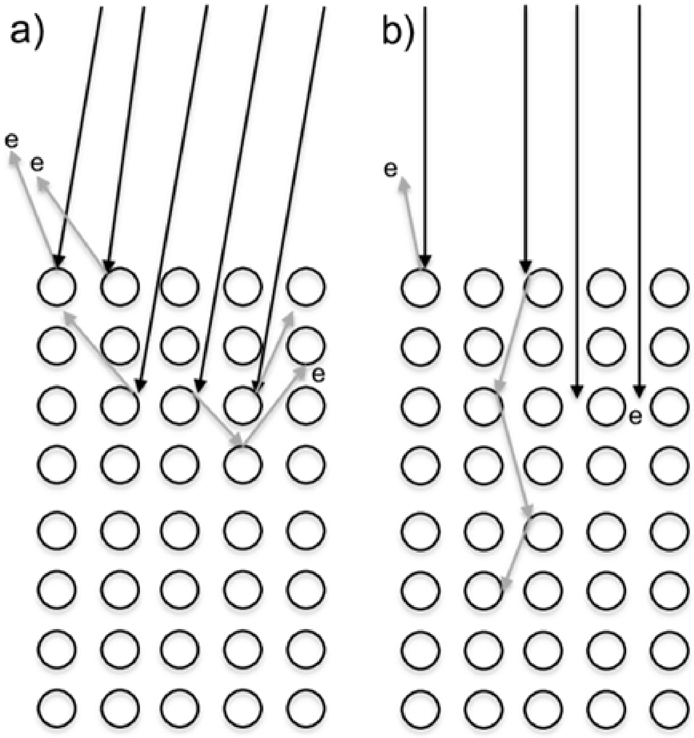

Figure 1.14: Schematic representation of the channeling phenomenon. (a) the angle between the atomic columns of the crystal and the electron beam is different from zero. (b) the electron beam is aligned with the atomic columns of the material, the channeling phenomenon occurs [JOY 82]

In Figure 1.14, for the case (a), the angle between the incident electron beam and the orientation of the crystal planes of low index (hkl) is different from zero. Incoming electrons will not be able to travel deep underneath the surface, and the backscattering phenomenon will occur close to the surface. Therefore, back scattered electrons will be emitted close to the surface, and many of them will reach the BSE detector: the grain will appear bright.

In the second case (b), the angle between the emitted electron beam and the dense crystallographic directions is close to 0. The vertical atomic columns, will act as "tunnels" or 'channels' for the electrons. Thus, the electrons will be able to travel a long distance in the crystal. The back scattered electrons will be emitted far away from the surface and many of them will not reach the surface of the sample, and later on the BSE detector. In this condition, the grain will appear dark.

In this second case, the presence of a dislocation will locally modify the channeling conditions due to the distortion of the crystal planes around the dislocation. When the crystal will be in proper condition (later called Channeling Condition), dislocations will be seen in white on a black background, as shown in Figure 1.15.

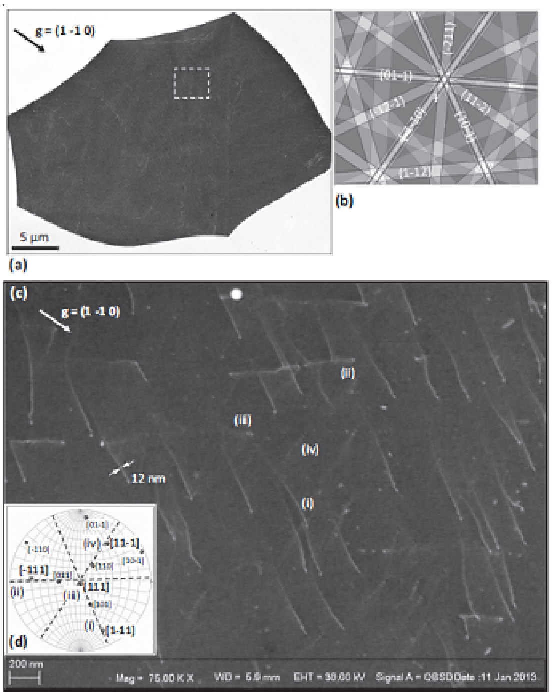

Figure 1.15: Example of ECC-image of dislocations in a bcc Fe–3% Si alloy. (a) Overview of the whole grain tilted into two-beam conditions, acceleration voltage 30 kV, WD 7.3 mm. (b) Simulated electron channeling pattern for the applied diffraction conditions. (c) A highly magnified ECC image of the area marked by dashed lines in (a) with several visible dislocation [ZAE 14]

In order to find these exact channeling conditions, it is necessary to use an "Electron Channeling Pattern" (ECP) [COA 67]. An ECP is a representation of measured intensities as a function of the angles between the crystal and the electron beam.

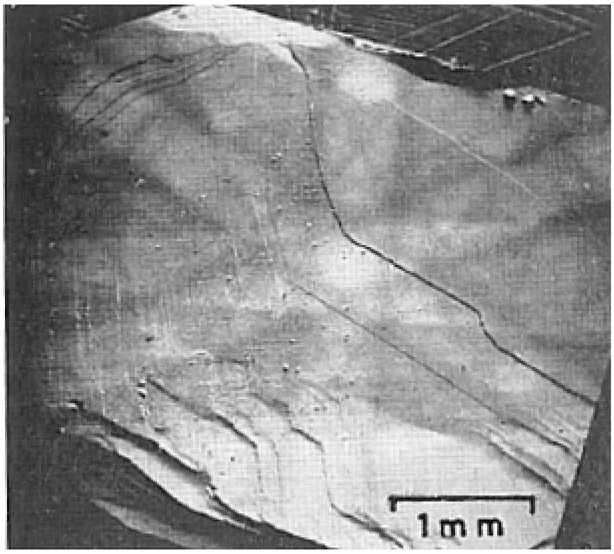

Figure 1.16: First Electron Channeling Pattern (ECP) acquisition on a GaAs single Crystal with visible kikuchi bands (red arrows [COA 67]).

In Figure 1.16, the kikuchi bands are visible and perfectly show the dependence between the electron backscattering phenomenon and the tilt angle of the incident beam, for a single crystal. Moreover, as for TEM imaging, it is necessary to be in Two Beam conditions in order to correctly image the dislocations. These conditions are also found on the edge of the diffraction bands (red arrows Figure 1.16)

Unlike ions, electrons cannot be only described by a ballistic approach (Figure 1.14) and must be treated by the dynamic theory of diffraction [JOY 82]. However, it is possible to describe the phenomenon of electron channeling in a simplified way from the Bragg's law at first order:

$$2d_{hkl}\sin\theta_B = \lambda \tag{1.18}$$

With d_{hkl} the interatomic distance, λ the wavelength of the incident electrons and θ_B the Bragg angle.

Clarke [CLA 71] used this method to observe dislocations in copper and aluminum. Now it is possible to simulate this type of ECP image from the kinematic or dynamic law of diffraction.

In the kinematic approach, a single incident wave diffracting on a crystal represented by a three-dimensional array of atoms is considered. Each atom acts as a point with a scattering power and is represented by a spherical wave. In this model, several approximations are made. First, the incident wave is not attenuated in the crystal, the interactions between the incident wave and the waves scattered by the atoms are therefore neglected. Second, it is considered that each wave is scattered only once. Finally, there is no absorption of the incident wave in the crystal. The intensity of electrons backscattered by the crystal is then proportional to the atomic structure factor. This model allows a fairly good description of the bands positions, as illustrated by the Figure 1.17, but, is however too simplistic to correctly describe the intensities observed experimentally.

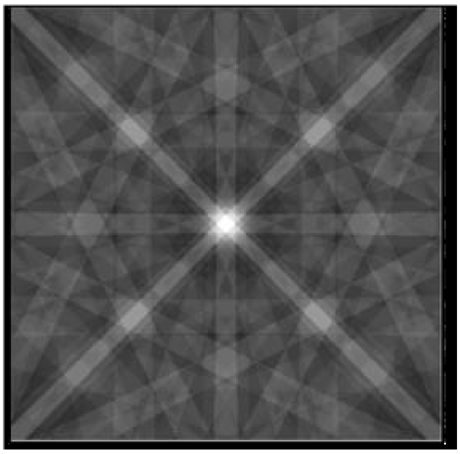

Figure 1.17: Kinematic simulation for a ferrite crystal and an incident beam of 15kV. Simulation performed with the ESPRIT DynamicS software (Bruker) [LAF 20]

In the dynamic approach of electron diffraction, multiple wave scattering events are taken into account for a given depth of the crystal. It is then necessary to determine the probability for each wave to be scattered in each layer constituting the penetration thickness of the incident wave. Different theoretical models have been developed [CLA 71][DUD 95][SPE 80] and the Bloch wave approach is one of the most used [PIC 14a][WIN 07]. In this model, the incident beam is modeled by a set of Bloch waves, i.e. waves having the periodicity of the crystal lattice, penetrating a crystal. The wave function ψ of the electrons is then expressed as:

$$\psi(\overrightarrow{r}) = \sum_j \alpha^j \sum_g C_g^j e^{2i\pi(\overrightarrow{k^j}+\overrightarrow{g})\cdot\overrightarrow{r}} \tag{1.19}$$

With $\overrightarrow{k^j}$ the incident wave vector, $\overrightarrow{g}$ the wave vector in the reciprocal space, C_g^j the Bloch wave coefficients and α^j the amplitude coefficients.

This wave function is then inserted into the Schrödinger equation which describes the diffusion of electrons:

$$\Delta\Psi(\overrightarrow{r}) + 4\pi^2 k_0^2 \Psi(\overrightarrow{r}) = -4\pi[U(\overrightarrow{r}) + iU'(\overrightarrow{r})]\Psi(\overrightarrow{r}) \tag{1.20}$$

With k_0 being defined as the norm of the incident wave in vacuum, $U(\overrightarrow{r}) + iU'(\overrightarrow{r}))$ the complex potential of the crystal lattice, the real part being determined from the atomic scattering factors and the position of the atoms while the imaginary part, which describes the absorption potential, is determined from the atomic shape factors.

The coefficients C_g^j are determined by solving an eigenvalue problem. The coefficients α^j are determined by the boundary conditions on the crystal surface. The determination of these coefficients is a problem of order N^3 with N the number of reflective planes considered. It can induce very important computation times. To reduce these times, one of the methods is to use the Bethe perturbation method [BET 28]. In Bethe's approach, the low contribution beams are treated as perturbations. Indeed, all the beams scattered in the crystal do not contribute equally to the multiple scattering phenomenon, therefore, it is not necessary to take all of them into account. The mathematical development to determine the beam selection criteria is detailed by

Wang *et al.* [WAN 16]. Finally, the probability of an electron backscattering at a given point in the crystal is calculated by the product $\Psi\Psi*$. The intensity is obtained by integrating the interaction depth of the electrons in the crystal, which can be determined statistically by Monte-Carlo simulation. This approach can be used to model EBSD patterns but also for the electron channeling patterns mentioned above. The main difference is that for EBSD, it is necessary to repeat the calculation for different energies close to the incident energy since an EBSD pattern consists of a sum of EBSD patterns of different energies [WIN 10].

The combination of the three phenomena (*i.e.* Bragg's law which gives the geometry of the bands, the kinematic diffraction which allows a wave to interact with the crystal and finally the dynamic approach which allows several waves to interact with each other) allows to obtain Figure 1.18.

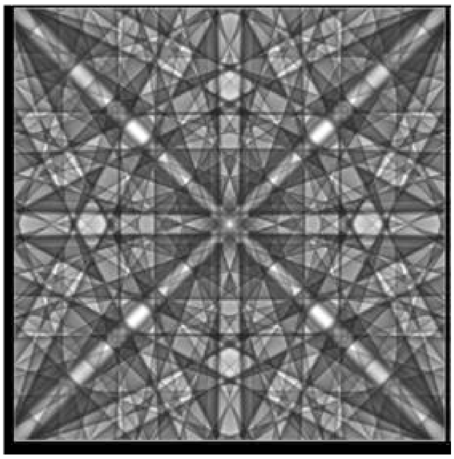

Figure 1.18: Dynamic simulation for a ferrite crystal and an incident beam of 15kV. Simulation performed with the ESPRIT DynamicS software (Bruker) [LAF 20]

From this type of simulation the angular positions to be reached to bring the sample in diffraction condition for dislocations observation can be determined.

1.2.3.2 Orientation methods

The difficulty of the ECCI method lies in determining and experimentally reaching the orientation conditions for dislocations observation. Indeed, orientating the sample close to a Kikuchi Band requires a perfect knowledge of the orientation of the observed sample.

To address this problem, several methodologies have been developed. The first one, performed on single crystals, consists in obtaining the scattering conditions through the observation of ECP, with the use of the BSE detector. The ECP are recorded from a selected area using the "rocking beam‘' method [VAN 71]. Figure 1.19 shows the trajectory followed by the electron beam inside the SEM. The beam is deflected twice around the intersection point of the optical axis and the sample. The method is based on the "focusing deflection‘' technique and consists in using another electron lens to realize the second deflection of the beam instead of the classical scanning coil.

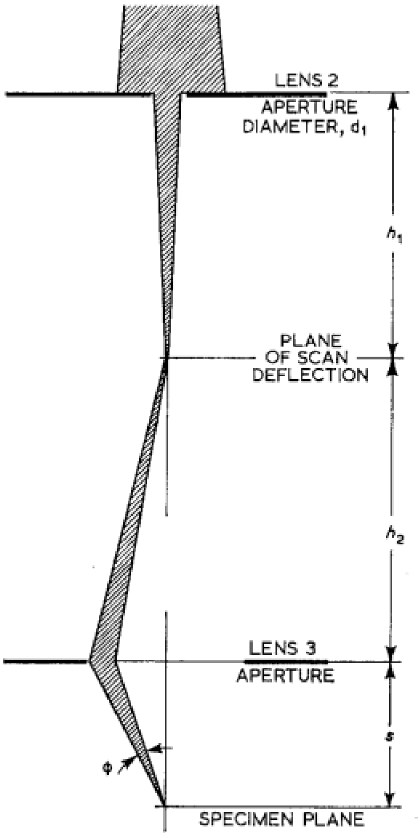

Figure 1.19: Diagram for deflection-focusing méthod of selected area scanning [VAN 71]

The conjugate points of this lens are:

(a) the intersection of the optical axis and the upper scan deflection;

(b) the intersection of the optical axis and the sample surface.

With this configuration, all electrons passing through (a) will arrive on the sample surface (b). Point (a) is the image point of the previous lens, so the beam is focused on the sample surface during the whole scan. The divergence of the probe is fixed by the aperture of the last lens and is determined by the focal length of this lens. In the case of the SEM, this aperture is located just after the plane of the lens 2 (numbering from the gun, Figure 1.19) and the total angular divergence is:

$$\phi = \frac{d_1 h_2}{h_1} \times \frac{1}{S} \tag{1.21}$$

A set of coils is placed above the objective lens and allows the beam to oscillate around a point on the sample surface. In this configuration, it is possible to obtain an ECP on a selected area. This method is more commonly called Selected-Area Channeling Pattern (SACP) [JOY 82]. The advantage of this method is that the objective lens current does not vary when switching between observation and SACP modes. In addition, filtering in BSE increases the contrast of SACP. The SACP is therefore obtained without changing the voltage used for observation.

Thus, changing from image mode to diffraction mode only requires a condenser lens excitation with a scanning-control modification and an aperture shift.

Unfortunately, currently developed SEMs no longer offer the possibility to collect SACP. Moreover, in the initial configuration of the microscopes, the collection area of the pattern is about five micrometers in diameter, which makes quantitative analysis of dislocations by ECCI difficult. The SACP obtained under these conditions might be too large for deformed crystals. Indeed, dislocations will create a disorientation inside the grain that will distort the pattern, making it difficult to identify the optimal channeling bands [KAC 91].

Another method, called Accurate-ECCI (A-ECCI), developed by Mansour *et al.* [MAN 14], is based on the live collection of High Resolution SACP (HR-SACP) and simulated EBSD images. It was efficiently used to characterize dislocations in a polycrystalline steel [MAN 14]. A-ECCI has been developed for the FEG electron column of the GEMINI type. The beam is deflected from the center of a selected aperture, which moves the electron beam away from the area of interest, but hitting the sample at an angle. Then, the electron beam is moved to the observed area by controlling the beam displacement. This process is repeated sequentially, tilting the beam over the area of interest and collecting HR-SACPs as a function of the tilt angle [MAN 14][MAN 15]. However, this method requires a particular installation on the SEM to perform portions of ECP.

In parallel to the A-ECCI method, another method has been developed by Gutierrez-Urriti *et al.* [ZAE 14][GUT 09] and uses EBSD orientation to calculate the rotation and tilt conditions needed to place the crystal in the proper channeling condition. The calculated condition is optimal for ECCI at low tilt angles. This procedure is known as controlled-ECCI (cECCI). The purpose of the cECCI method is to use EBSD instead of ECPs to orient the sample in an observation condition. Figure 1.20(a) shows the illustration of the set-up proposed by Gutierrez-Urrutia *et al.* [GUT 09]. Two configurations are used:

- the first one allows to perform ECCI images. In this configuration, the sample is placed perpendicular to the incident electron beam (ECCI position);

- the second is used to perform EBSD measurements. In this configuration, the sample is tilted by 20° with respect to the incident electron beam. This places the sample in a classical configuration for EBSD (EBSD position).

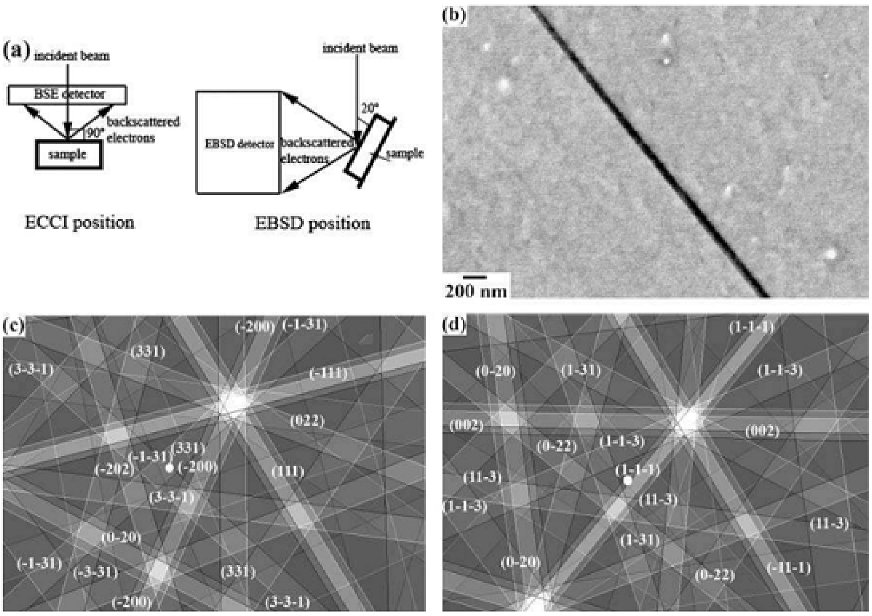

Figure 1.20: (a) Schematic illustration of the set-up for ECCI in SEM under controlled diffraction conditions. (b) ECCI of a mechanical twin under controlled diffraction conditions with the matrix bright and the twin dark. Simulated diffraction patterns of the crystal matrix (c) and twin (d) [GUT 09]

The ECCI protocol consists of first selecting the area of interest. To do this, the sample is placed in the “ECCI position‘’, with a tilt angle close to 0°. Once the area is selected, the sample is tilted by 70° to obtain an EBSD map of the area. For each point of the EBSD map, the tilt and the rotation angles required to orient the crystal under optimal conditions are calculated from the EBSD orientation map with an in-house software [ZAE 00] Figure 1.20(b) to (d) shows an example of a result obtained by Urrutia *et al.* [GUT 09] on a TWIP steel. Figure 1.20(b) shows the ECCI image obtained on a mechanical twin. The ECP of the matrix (Figure 1.20(c)) and the twin (Figure 1.20(d)) are simulated from the EBSD maps. The ECCI image Figure 1.20(b) was acquired under conditions where the contrast is optimal, *i.e.* when one of the two crystals (matrix or twin) is oriented outside the channeling conditions (Figure 1.14(a)) while the second crystal is oriented in optimal channeling conditions (Figure 1.14(a)).

The cECCI method therefore allows for efficient orientation of the sample under the two-beam conditions necessary for dislocation imaging. However, this approach requires the use of many complex calculations. Furthermore, in the context of dislocation density measurements or the nature of slip systems determination, multiple images are required under different diffraction conditions, which requires changing the tilt and rotation angles between each image. Moreover, the calculation of tilt and rotation angles does not consider the internal grain disorientation caused by the presence of dislocation. In deformed samples, the presence of dislocations will disturb the observation conditions. These observation conditions can vary within a grain by several degrees depending on the density of dislocation in the grain.

1.2.3.3 Rotationnal-ECCI and clustering

Regardless of the method used, the sample orientation step under channeling conditions is a difficult step. Moreover, the presence of dislocations and thus of internal disorientations implies that the observation conditions might change inside the grain, especially for deformed samples. The Rotational-ECCI (R-ECCI) method was developed to avoid the orientation steps of the sample.

The experimental conditions for image acquisition are similar to those used by the eCHORD method [LAF 20][LAF 18]. To do this, the sample must first be tilted by few degrees and rotated by 360°. A backscattered electron (BSE) image is acquired at each rotation step, such that 180 or 360 images are recorded, for 1° or 2° rotation steps, respectively. During the rotation, the orientation of a given pixel describes a circle on the selected grain's electron channeling pattern (ECP). The radius of this circle in yellow in Figure 1.21 corresponds to the selected tilt angle. For any grain orientation, this circular crystallographic path should always cross at least one Kikuchi band (green dots in Figure 1.21); therefore, several rotation angles should correspond to adequate diffraction condition for dislocation imaging, *i.e.*, at the Kikuchi band edges [CAZ 19]. For a large tilt angle, the circle diameter will be larger and more diffraction bands will be crossed. However, this can lead to some geometrical difficulties within the chamber during the sample rotation; the sample might be touching one of the detectors. A tilt angle of 5°–10° appears to be the best compromise to cross a sufficient number of bands without any danger for the detectors.

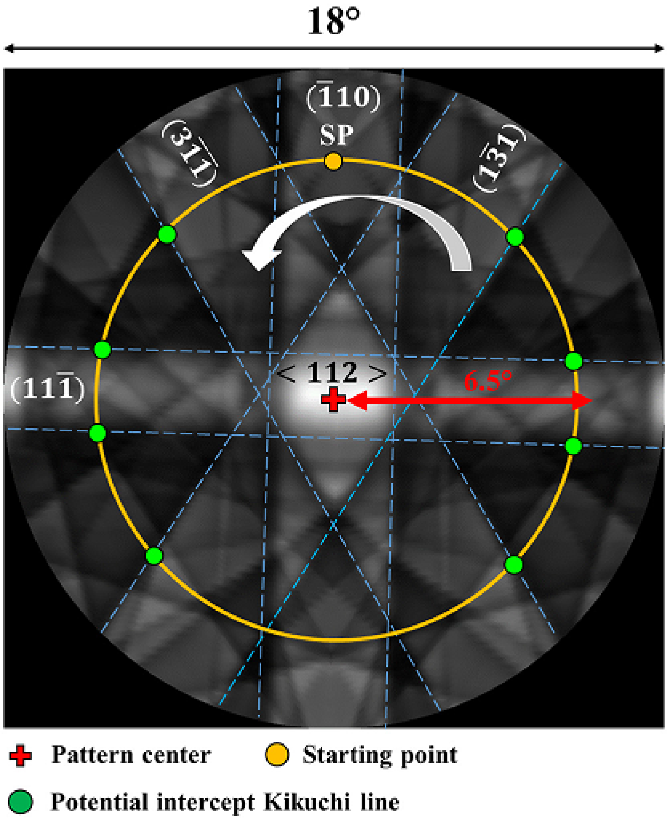

Figure 1.21: Simulated ECP for FCC structure from EMSoft. Green dots show the potential Kikuchi lines that will be intercepted for a tilt angle of 6.5° [L'H 19]

This procedure is automated using a rotating sub-stage, together with the use of a program that acquires an image after each rotation step, developed in the framework of the e-CHORD project [LAF 18]. For dislocation imaging, the magnification required is high (minimum 5 nm/pixel), and the image quality is sensitive to a perfect astigmatism or focus setting. However, each image acquisition takes approximately 1 min 30 s, and a drift in the focus/astigmatism together with a mechanical drift of the sample occur along the rotation and time. It is thus necessary to refocus and recenter the ROI by hand every 5–10 images.

A preliminary 360° series at very low magnification is first acquired. For each pixel of the ROI, the grey-level intensity is plotted as a function of the rotation angle to obtain a so-called "intensity profile" shown in Figure 1.22. ECP could be calculated from this intensity profile to obtain the precise crystallographic orientation of the grain. The rotation angles of interest for ECCI imaging are determined by the series of images obtained during the rotation of the sample and the intensity profile obtained for each pixel. The angular ranges corresponding to dislocation contrast conditions are the local minimun of this intensity profile (see [CAZ 19]), *i.e.* where the matrix is the darkest.

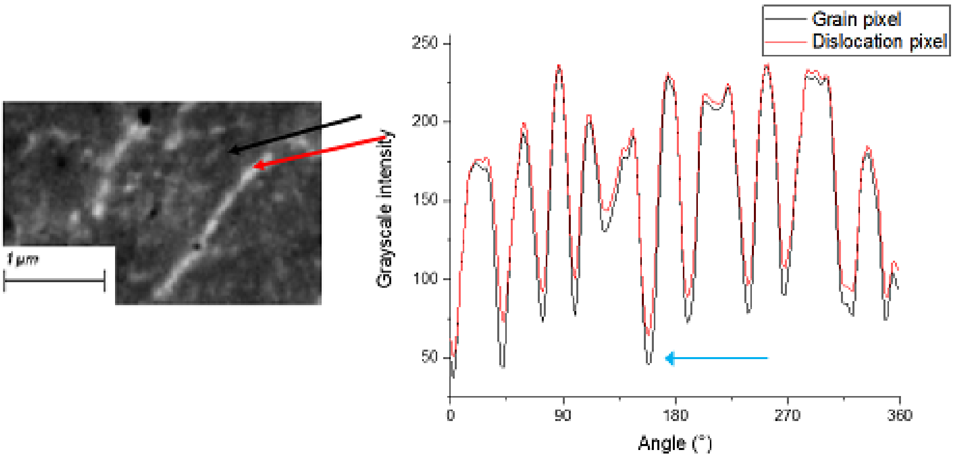

Figure 1.22: (a) ECCI image acquired on a ferrite sample. The black arrow represents a pixel of the matrix and the red arrow represents a pixel of a dislocation. (b) gives the intensity profiles of the two selected pixels of the image (a) with the same color code. The blue arrow shows one of the local minimums which is one of the conditions for observing dislocations.

It is on these local minima that the dislocations appear in white and the rest of the grain appears in black. Therefore, their intensity is greater than that of the grain for these angular conditions (Figure 1.22, blue arrow). This small difference in intensity between the dislocations and the grain matrix allows to adopt an automatic dislocation detection approach by clustering.

To improve calculation times and reduce acquisition times, it is possible to limit the observations to these angular ranges corresponding to the local minimas. It is then possible to switch from a 360° series to several "mini-series" of 20° to 30° each.

A pixel clustering method based on the analysis of the contrast variation between the dislocations and the grain-matrix profiles was developed to allow for an automatic determination of the dislocation density [CAZ 19]. The procedure is detailed in Chapter2, and the main steps are the following. The clustering is divided into two steps. The first step consists of partitioning

[CHE 96][JAI 99][JAI 10] the elements to be classified, *i.e.*, grouping all the elements contained in the same grain, as in Figure 1.23(a) where the different grains in the selected area are detected with different colors. The second step is the classification [DEC 09][DID 13], which consists of identifying each of the elements constituting these partitions (grains), i.e., identifying dislocation pixels, matrix pixels, and noise pixels, as in Figure 1.23(b) where the dislocations inside the grain were detected and highlighted in blue. Indeed, the pixels located on a dislocation present a profile identical to one of the pixels located in the grain, except for the diffraction condition, for which the dislocation appears bright and the matrix dark [CAZ 19][ZAE 14]. The intensity profiles corresponding to dislocations therefore present a local minimum with higher intensity.

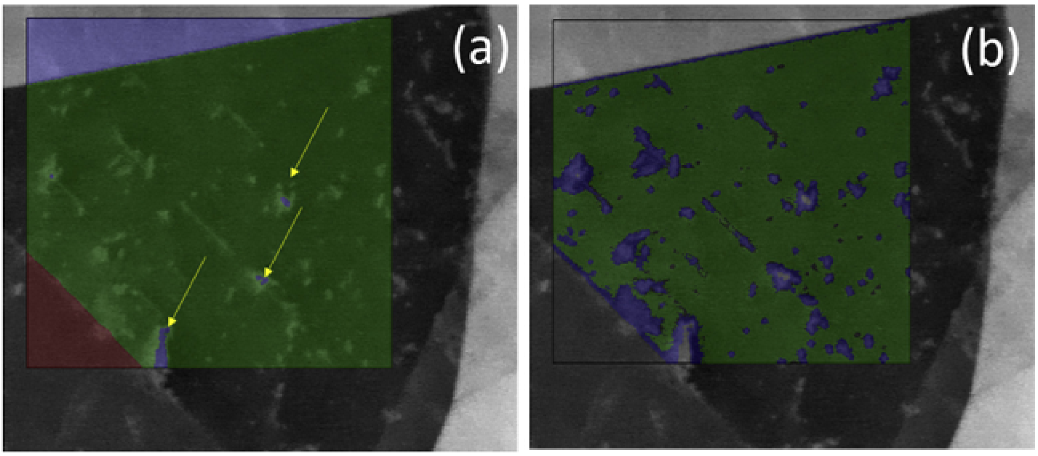

Figure 1.23: (a) Clustering of the mini-series used to partitioning the different grains (clusters) and (b) defect classified within the selected cluster [CAZ 19]

The partitioning step presented in Cazottes *et al.* [CAZ 19] was based on the calculation of the difference between a considered pixel profile and the average profile of the grain (obtained from all the profiles contained in the selected grain). If the difference between the two profiles is too high, the pixel is not considered to be part of the grain. However, for a deformed grain, an internal disorientation can appear. In that case, profiles from adjacent pixels will still be close; however, profiles from further pixels might differ, although they are part of the same grain.

The dislocation density is later calculated by a simple counting method: $\rho = \frac{N}{S}$, where N is the number of defects in the analyzed area S. However, this calculation method does not consider the thickness of the analyzed area. In the case where all the dislocations are perpendicular to the surface, this method is of unequalled accuracy. However, in the general case where the dislocations are randomly oriented, a correction coefficient must be applied to correct the influence of the volume. This correction coefficient is difficult to determine experimentally and will be developed in the next chapter.

Figure 1.24 presents an austenitic grain deformed at 35%. It is possible to observe several areas with different observation conditions. Zone A is under suitable observation conditions for the dislocations; therefore, the dislocations are visible in white on a black background. However, a few hundred nanometers around, it is no longer the case: zone B is outside of these observation conditions. It is not very far from its observation condition as the dislocations are still barely visible. Finally, zone C, located further away, is completely out of the observation conditions.

In this area, the grain is completely white and the dislocations are not visible. The distortion leads to different diffraction conditions throughout the grain. Therefore, a comparison with the average profile of the grain is no longer relevant on deformed materials. It is then necessary to modify the profile comparison strategy using a more local average profile around the analyzed pixels. This will be developed in chapter 2: R-ECCI methods for deformed materials.

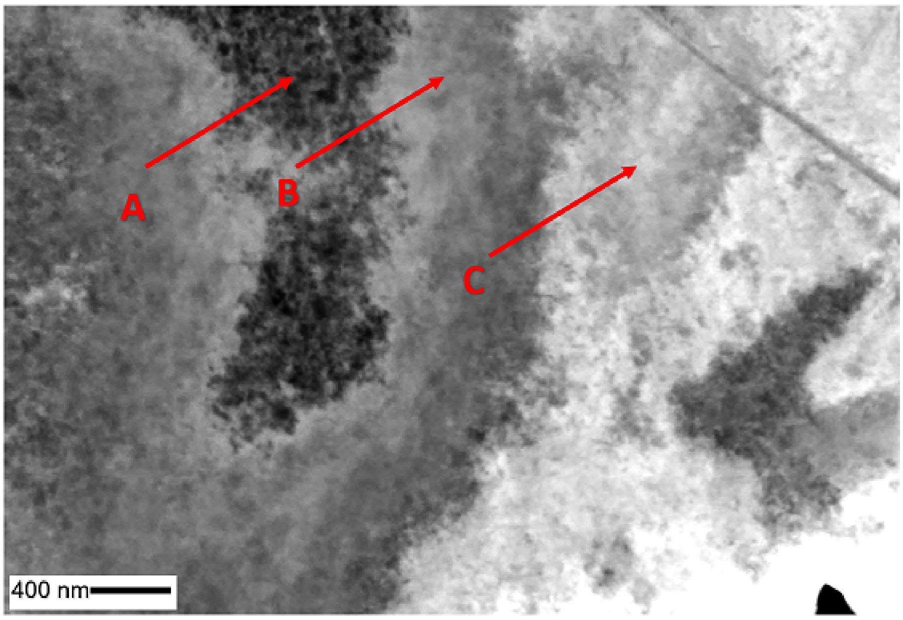

Figure 1.24: Example of a BSE image acquired with an acceleration voltage of 20 kv, an aperture of 120 μm, and a pixel size of 4.5 nm and obtained on a 35% deformed austenite grain. The important disorientation in the grain generates three different zones: (a) a zone where the dislocations are in observation conditions; (b) the disorientation of the grain moves away from the observation conditions, which reduces the contrast between the dislocations and the grain; and (c) the observation conditions of the dislocations are lost, and the dislocations are no longer visible.

1.2.4 Indirect methods for dislocation density measurement

Imaging methods (TEM and SEM) allow direct measurement of dislocation density through their observation. There are other applicable methods that allow to obtain this information such as EBSD orientation maps or XRD diffraction peak deformation.

EBSD is mostly used to characterize microstructures through orientation maps. Indeed, GND density is then computed from the local crystal curvature (through the local disorientation θ) and the map step size [NYE 53],[EST 84],[SUN 00],[ELD 03],[PAN 08]. Although common, this approach is questionable. The uncertainty on the crystallographic orientations limits the sensitivity on GND densities, the resulting disorientation axis being significantly imprecise for low disorientation angles [PRI 99]. Weighed Burgers vector method proposes to consider a kind of Burgers circuit in order to reduce the imprecision at low disorientation angles [WHE 09], but only three components of the curvature tensor are considered and the contribution of elastic strain is also neglected. The latter is nevertheless a reasonable assumption in plastically deform metals [WIL 10],[ERN 20b][28,29], but not at slightly disoriented materials such as in GaN single crystals[ERN 20b].

Another method, High (angular) Resolution EBSD (HR-EBSD), based on the acquisition of EBSD orientation maps has been developed in the ATEX-software [BEA 17] (developed at the University of Lorraine). The HR-EBSD technique was developed under the impetus of Wilkinson *et al.* [WIL 06] and recently experienced a revival with the emergence of global image registration approaches [VER 18],[RUG 18],[SHI 19], like the method used in this study [ERN 20b],[KRÖ 58]. All these methods apply digital image correlation techniques to a pair of Kikuchi patterns in order to measure their relative displacement field with subpixel accuracy. Coupled with the precise knowledge of the projection geometry, relative lattice rotation and elastic strain can be captured with a typical accuracy of 10^{-4} ($> 0.006°$) in good experimental conditions. The Nye's tensor can then be calculated including the contribution of the elastic strains [KRÖ 58]. The complete determination of this tensor remains however limited by the two-dimensional nature of EBSD measurements, hence the growing interest in 3D HR-EBSD studies like in [KAL 20]. The higher accuracy of HR-EBSD techniques as compared to an indexing-based GND derivation comes with practical considerations limiting its wider use: use of a high-resolution camera with longer exposure time, large data collection (15 to 20 GB for the maps used in this article), each diffraction pattern being stored for the subsequent numerical intensive data post-processing. That is why identifying the cases of applications where the method brings a real improvement compared to indexing, in particular for deformed polycrystals, is crucial [ERN 20b],[DHI 22],[ERN 20a],[JIA 13].

The use of disorientation maps to calculate the dislocation density does not allow the calculation of the total density. Indeed, only the dislocations contributing to the disorientation will be detectable by these methods, so only the GND density is measured here. The SSD part of the dislocation density is averaged in the noise of the EBSP images and cannot be processed (depending on the pixel size of the image).

XRD is a more global measurement technique, that is often performed on a much larger volume, which in the present case will contain many grains of both phases with different orientations, and this different deformation behavior. The calculation of the dislocation density by X-Ray Diffraction (XRD) is based on the broadening of the diffraction peak [WAU 15]. The calculation assumes the presence of 'crystallites domains' that would correspond to the cell/structure. Therefore, dislocations present at cells or grain boundaries would not be taken into account.

This was experimentally confirmed by a direct comparison TEM / XRD measurements made on copper single crystals by Ungar et al [UNG 84].

In the context of X-ray Diffraction (XRD) it is quite difficult to determine which density is observed. Many observations and studies of dislocation density do not specify whether it is GND, SSD or the sum of the two that are observed [LEE 14][DIN 10]. Some studies indicate that it is the SSDs that are observed by XRD [SHA 20] [WAU 15], while other studies show that the GNDs contribute, in a high proportion, to the diffraction peak profiles [ZRI 19]. Moussa *et al.* [MOU 15] explain that the accuracy of the orientation measurement and the spatial resolution have a direct influence on the discrimination between GNDs and SSDs for both SEM and XRD methods. This lack of information and precision on the capabilities of each method shows the difficulty of comparing all methods with each other and demonstrates that discussing the proportions of GND/SSD is dependent on the acquisition conditions. This comparison between the different methods and the measurements of GND and SSD will be studied and discussed in chapter 4.

1.3 Conclusion

In this chapter, the plasticity of crystals has been discussed to explain some existing deformation mechanisms (strain hardening, restoration). The mechanism of dislocation multiplication via Frank-Read sources was discussed to describe the dislocation dynamics. The importance of the dislocation density ρ was highlighted through the Kocks-Mecking and Estrin (KME) and Hall-Petch mechanical models. The different types of dislocation (GND and SSD) have been defined. Transmission and scanning electron microscopes are at the heart of dislocation studies. Based on the diffraction of crystal planes, these microscopes allow the understanding and indexing of dislocations in the material, as well as their sliding system in order to understand how the material evolves under a given stress. These deformation mechanisms being strongly dependent on the initial density of dislocations in the material, it is therefore important to measure it with a good representativity.

To measure this dislocation density, imaging analysis methods have been described, such as the intercept method and the N/S method. However, these methods have their limitations because they do not consider the tilt of dislocations. In addition, the uncertainty on the analyzed depth with ECCI method is difficult to estimate accurately and there is also a measurement error when the material is deformed, a high number of dislocations can saturate the image and distort the results. These sources of error will be studied in chapters 2 and 3.

Other methods have been developed for SEM (A-ECCI, cECCI and R-ECCI). Each of these methods provides the conditions for the observation of dislocations. However, the A-ECCI and cECCI methods require either a SEM capable of rotating the incident electron beam over a small area or software to process the EBSD data. In this project, we want to develop the R-ECCI method, which allows the observation of dislocations in SEM. This method not only has the advantage of easily observing dislocations, without affecting the sample, but also of giving us access to the intensity profiles of dislocations and of the grain that contains them.

The difference of intensity depends on the nature of the defects (dislocation, dust, etc.), which means that they can be treated numerically. This difference of intensity between the defects and the grain that contains them is the basis for clustering software developed in partnership with the company Axonsquare. Forward, this software not only detect dislocations located in a grain but will also calculates a dislocation density. The details of the R-ECCI method and the clustering will be presented in chapter 2.

Chapter 2

About the automatic measurement of the dislocation density obtained by R-ECCI

Sommaire

2.1 Introduction

In the previous chapter, it was shown that the microstructure, and dislocations in particular, greatly affect the mechanical properties of metallic materials [NAD 88]. Therefore, it is necessary to accurately characterize these values.

A new dislocation detection algorithm was developed, with the aim of better characterizing grains that would exhibit internal disorientation caused by the presence of dislocations. This new method is applied for a duplex stainless steel for different deformation levels.

Then, the reliability and possibilities, such as the maximum and minimum achievable densities, were characterized.

A theoretical review of the uncertainty factors is presented, and then, some parameters are studied theoretically in detail, such as the effect of the analyzed volume projection and the effect of dislocation overlap. Then, the effect of the clustering algorithm is presented.

2.2 Materials and methods

The SEM observations were performed on a Zeiss Supra 55VP SEM with an accelerating voltage of 20 kv using a 120 μm diaphragm and a working distance of $\approx$7 mm. The SEM images were recorded with a pixel size of 4.5–6 nm and a size of 1024 $\times$ 768 pixels.

2.2.1 Materials

Observations were made on a commercial Outokumpo 2101 lean duplex stainless steel that was mechanically ground, with final polishing performed using a 1 µm diamond solution. To avoid any strain hardening of the surface, a final electropolishing step was performed using an A2 electrolyte (from Struers APS, Denmark) at 20 V for 60 s with the Lectropol 5 device (Struers APS, Denmark).

The evolution of the dislocation density was characterized in both ferritic and austenitic phases. Micro tensile samples (total length 112.5 mm, width 12.5 mm, and thickness of 1.5 mm) were deformed using a MTS tensile machine. Standard digital image correlation (DIC) was used to follow and precisely measure the deformation of each point of the sample surface. One sample was deformed up to 3% and the other one up to 10%. Then, R-ECCI was applied to several grains for each deformation state. Figure 2.1 presents isolated images of the rotation image series that reveal the dislocation structure for undeformed and 10% deformed ferrite, Figure 2.1 (a) and (c), respectively, and for undeformed and 3% deformed austenite, Figure 2.1 (b) and (d), respectively.

In the undeformed state, dislocations in ferrite appear as dots or lines on the image, indicating that their orientation relative to the surface is quite random. The matrix is not completely dark and appears quite noisy. The contrast of vertical dislocations (appearing as dots) is greater than that of the horizontal dislocations. A large white zone is observed that could originate from the presence of a large defect or a polishing artifact that was not considered in the data treatment. After deformation, more tortuous dislocations appeared in the ferrite grains as well as more dot dislocations. In the grain presented in Figure 2.1c, the bottom part of the grain is in good condition for dislocation imaging (dislocations appear white on a dark matrix), while the top part of the grain appears bright and dislocations are not visible. This is due to the local disorientation that appeared during deformation, the orientation of the grain is not similar on its top and bottom part. Therefore, the orientation of the sample required to image dislocation is not the same for the bottom and top part. This reveals one of the major advantages of using intensity profiles instead of single images for the determination of dislocation densities, as already presented in [L'H 19]. In the rotation image series, all part of the grains will become suitably oriented but not for the same rotation angle. Therefore, using an adapted clustering algorithm, it is possible to detect dislocations in all part of the grains, even if a slight disorientation is present within the grain.

For austenite grains in the as received condition, Figure 2.1(b), few dislocations are present, the matrix is homogeneously dark, and dislocations present a very high contrast. However, after only 3% of deformation, the amount of dislocations in the austenite phase is very high, dislocations are very long and linear, and appear aligned along 111 type planes. This high dislocation density is expected as austenite deforms before ferrite in duplex stainless steels. In this case a distortion of the grain is also present, which explains the fact that the top right and left part of the grain are very bright, while the bottom remains in diffraction condition. The apparent density is so high that dislocation might overlap within the analyzed volume, which would lead to uncertainties in the density measurement.

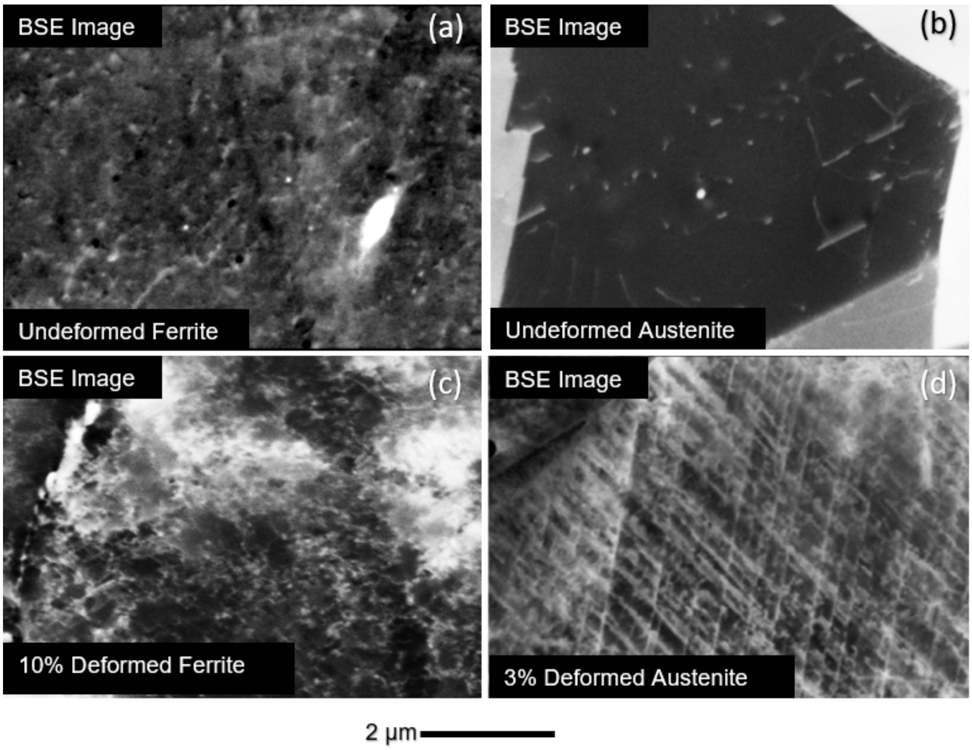

Figure 2.1: BSE image extracted from the series acquired on different grains. For each image, the dislocation lines are visible in white on a black background. Each image was acquired with an acceleration voltage of 20 kv with a pixel size of 4.5 nm and an aperture of 120 μm. (a) Undeformed ferrite grain. (b) Undeformed austenite grain. (c) 10% deformed ferrite grain. (d) Austenite grain deformed at 3%, where dislocations are visible.

2.2.2 Acquisition method

The acquisition method is the same as the one presented in section 1.2.3.3 Rotational-ECCI and clustering. The switch for “mini-series‘’ was made to limit the acquisition time and the mechanical drift and to obtain good quality.

2.3 Adaptation of the clustering algorithm for distorted grains

As mentioned in the previous chapter, the disorientation contrast (Figure 1.24) requires a new approach to characterize the deformed samples

The algorithm was changed such that the analyzed pixel intensity profile is compared with a local average of intensity profiles around it. The number of neighbors selected for the average is selected, with the variable b called the “bin size‘’ (see Figure 3). If the analyzed pixels are located at the edges of the image, the area is cropped, and the average is obtained on a reduced number of pixels.

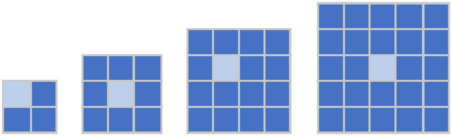

Figure 2.2: Illustration of the analysis parameter “bin size‘’ with a value of 2, 3, 4, and 5, respectively. The analyzed pixel is shown in light blue, and its neighbors are shown in deep blue.

For profile comparison, the intensity profiles were then transformed into vectors. The intensity profile of a pixel located at (i, j) will be transformed to the vector $\overrightarrow{P_{(i,j)}} = (x_1, x_2, \dots x_N)$ of dimension N, N being the number of images contained in the stack and the x_i values being the intensity in gray level of the pixel (i, j) for the image N.

If mini-series are used, then the vector $\overrightarrow{P_{(i,j)}}$ used for comparison of the intensity profiles will have a dimension N' smaller than that of a complete series, thus decreasing the necessary calculation time previously presented in [CAZ 19]. The distance $D(\overrightarrow{P_{(i,j)}}, \overrightarrow{P_{(k,l)}})$ between the vectors contained in b and the central point of the bin size (Figure 2.2) is calculated using an Euclidean difference:

$$D(\overrightarrow{P_{i,j}}, \overrightarrow{P_{k,l}}) = \left\| \overrightarrow{P_{i,j}} - \overrightarrow{P_{k,l}} \right\| \tag{2.1}$$

For very diffuse dislocations or for noisy images, normalizing the $\overrightarrow{P_{i,j}}$ vectors can improve the results. In the studied case, the Euclidean normalization was used: $\overrightarrow{P'} = \frac{\overrightarrow{P}}{\sqrt{\Sigma P_i^2}}$.

Then, to enable the detection of pixels that have sufficient profile variations to be potential defects, a value d_b, representative of the mean distance between this pixel and its environment, is calculated. For each pixel (i, j), surrounded by $b^2 - 1$ neighbors (see Figure 2.2):

$$d_b(i, j) = \frac{1}{b^2} \sum_{(i',j')\text{ neighbor of }(i,j)} D(\overrightarrow{P_{i,j}}, \overrightarrow{P_{i',j'}}) \tag{2.2}$$

A map, called “Features‘’, represents the areas for which d_b exceeds a certain threshold d_t and highlights the defects in green (Figure 2.3(b)).

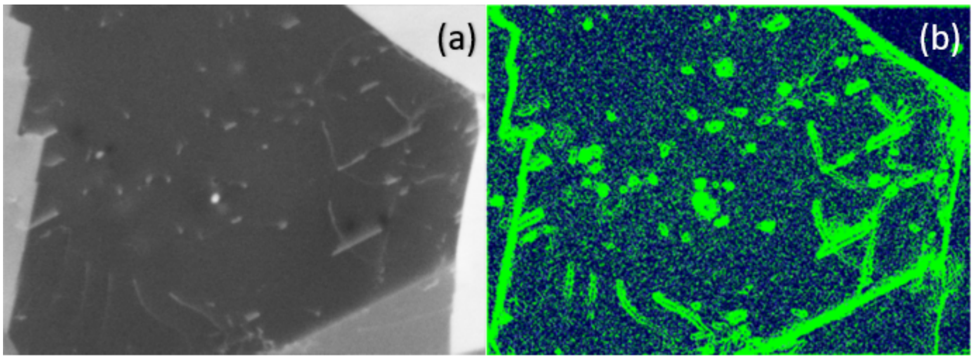

Figure 2.3: Example of "Features" map obtained from a series of BSE images of an undeformed austenite grain. (a) BSE image where dislocations appear in white on a black background. (b) Corresponding "Features" map obtained with the profile analysis, which shows in green all the intensity profiles that differ from those of their neighbors. This map was obtained with a bin size of 5 and a threshold d_t equal to the 77th percentile of $d_b(i, j)$

This "Features" map (Figure 2.3(b)) shows areas containing local "anomalies" with respect to the profiles contained in the stack. These anomalies may be dislocations but also dust, grain boundaries, or other defects that locally affect the contrast. All anomalies (dislocation and noise pixels) are placed in a set named *roi* (roi stands for region of interest). All the other pixels are considered matrix pixels.

2.3.1 Noise Detection

This step aims to distinguish dislocations from other defects within $_{roi}$. Defect pixels are stored in a cluster called K_{dp} (*dp* stands for "discarded pixels"). The assumption here is that the difference in the intensity profile of a discarded pixel and the local matrix or dislocation profiles will be large regardless of the angle and orientation condition. It represents the fact that a defect (dislocations excluded) is always visible on all images of the series. In contrast, dislocations become visible only for particular angles, which correspond to the visibility conditions.

For this purpose, it is first necessary to group the different pixels contained in K_{roi} into different "objects", formed by percolating pixels of K_{roi}. Let K_{o_l} be the ensemble of pixels of an object of index l. Small objects containing less that n_p pixels, which cannot be dislocations, are automatically discarded and their pixels are put in the "discarded pixel" cluster.

Around each object, we define a local area of the matrix, called the matrix margin (mm), that will be used to calculate the average local profile of the matrix $\overrightarrow{P^l_{mean}}$. The matrix margin area around each object is defined by the sum of matrix pixels contained within a circle of radius b_m centered on all pixels of the object. All pixels lying in the Matrix Margin of object 1 are included in a region named K^l_{mm}:

- $\forall (i, j) \in K_{o_l}$, for all pixels $(i', j') \notin K_{roi}$ such that $(i - i')^2 + (j - j') < b_m^2$
    - $(i, j) \in K^l_{mm}$

The average local profile of the matrix $\overrightarrow{P^l_{mean}}$ around object l is defined as

- For all $(i, j) \in K^l_{mm}$, $\overrightarrow{P^l_{mean}} = (\overline{x_{ij1}}, \overline{x_{ij1}}, ..., \overline{x_{ijN}})$

For the sake of illustration, Figure 2.5(b) shows the matrix margin region (white pixels) around the object indicated by the red arrow. All profiles of all pixels of the image are then normalized (profiles with a prime (') represent normalized profiles):

- $\overrightarrow{P'_{(i,j)}} = (x'_1, x'_2, ..., x'_N)$ with $x'_n = \frac{x_n - MIN(x_N)}{MAX(x_N) - MIN(x_N)}$

This normalization decreases the distance between the matrix and dislocation profiles, as illustrated in Figure 2.4c. However, the intensity profiles corresponding to noise or artifacts will still have differences over the entire profile that do not change much with normalization. This step allows dislocation pixels to be distinguished from noise pixels contained in the image. For this, the Euclidean distance D of the normalized profile is compared with a value H. The distance D between the normalized profiles of the matrix dislocations will be very small while the distance D between the normalized profiles of the matrix and the other defects will remain large. For each object l,

- $\forall(i,j) \in K_{o_l}$, if $D(\overrightarrow{P'_{i,j}}^{l}, \overrightarrow{P'_{mean}}^{l}) > H$ then $(i,j) \in K_{dp}$

Finally, some other black spots usually appear in the images (see Figure 2.4), which correspond to intensity profiles that follow the same trends as the average grain profile and an intensity difference with the local matrix that is too low to be discarded in the previous step. These pixels will be removed under the assumption that the local difference between the matrix and dislocation is necessarily positive (*i.e.*, the dislocations appear white on a black matrix).

- $\forall(i,j) \in K_{o_l}$, and $\forall(i',j') \in K^l_{mm}$, if (for all series $n, x_{ijn} < xi'j'n$) then $(i',j') \in K_{dp}$

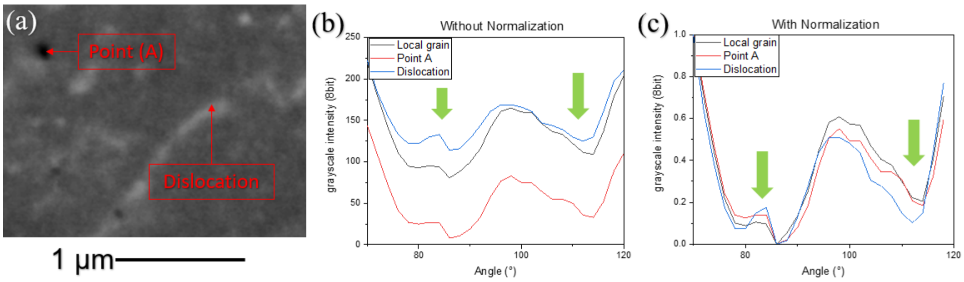

Figure 2.4: (a) BSE image of dislocation contained in an undeformed ferrite grain obtained at an accelerating voltage of 20 kv. (b) Intensity profile of the matrix (in black) of a dislocation pixel (in blue) and of a black point (in red) without normalization. The green arrows represent conditions where dislocations are visible in white on a black background. (c) The same intensity profile as (b) with normalization.

2.3.2 Detection of dislocations

After having discarded noise pixels (see previous section), dislocation pixels are detected by analyzing *separately* the intensity differences near local minima (diffraction condition). Mini-series are extracted from the complete series of image profiles. Each mini-series describes the intensity profile near a local minimum:

- $\overrightarrow{P_{(i,j)}} = \overrightarrow{P_{(i,j)^1}}, \overrightarrow{P_{(i,j)^2}}, ..., \overrightarrow{P_{(i,j)^{N_s}}}$

Where N_s is the number of observation mini-series.

For each object of index l and each mini-series of index n_s containing N_{n_s} images, we calculate the mean local matrix profile:

- For all $(i,j) \in K^l_{mm}$, $\overrightarrow{P^{l,n_s}_{mean}} = (\overrightarrow{x^{n_s}_{i'j'1}}, \overrightarrow{x^{n_s}_{i'j'2}}, ..., \overrightarrow{x^{n_s}_{i'j'N_{n_s}}})$

For each mini-series of each object l, the difference of the integrals between each pixel of K_{o_l} and K^l_{mm} is calculated. If one or more mini-series exhibits a distance larger than a threshold ε_d, the pixel is considered a dislocation pixel.

- $\forall(i,j) \in K_{o_l}$ if one or more mini-series satisfies $\sum_{x_1}^{x_{N_{n_s}}} \overrightarrow{P^{l,n_s}_{i,j}} - \sum_{x_1}^{x_{N_{n_s}}} \overrightarrow{P^{l,n_s}_{mean}} > \varepsilon_D$, then $(i,j) \in K_{dislocation}$

$K_{dislocation}$ is the set of pixels considered as dislocations.

The ε_D value represents the difference necessary for the pixel (i,j) to be considered a dislocation. It is therefore necessary to proceed by iteration from the ECCI images to determine and refine its value.

2.3.3 Results of the clustering

A so-called « Cluster Map » (Figure 2.5) is used to verify the parameters used in the previous analyses.

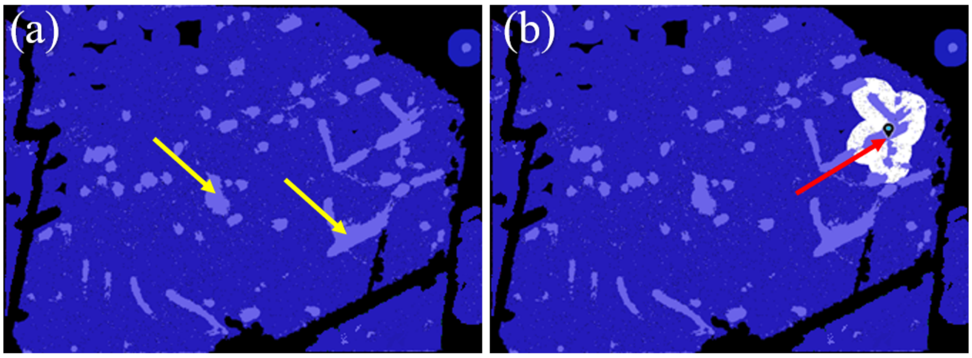

Figure 2.5: Example of Cluster Map obtained on an undeformed austenite grain. (a) The grain appears in dark blue while the areas of interest or potential defects appear lighter in this area (yellow arrows). (b) Illustration of the "Matrix Margin‘' (Bm neighbors) zone that appears in white and that is used to calculate the local average value of the grain for comparison with the different pixels contained in the zone of interest (red arrow). Cluster map obtained with $b_m = 30$ pixels, $\varepsilon_D = 40th$ percentile. The objects composed of less than 5 pixels were excluded.

The excluded profiles (too different from the rest of the grain, grain boundaries, etc.) are plotted in black, and the different grains appear with different colors. Moreover, the defects detected via the "features‘' (Figure 2.3) appear in the same color as their corresponding grain but lighter (yellow arrows). In the example in Figure 2.5, the pixels located in the lighter zone (yellow arrow) can be compared with the local average of the grain profiles, calculated in a zone around it, whose thickness is equal at B_m, as indicated in white (red arrow).

In the BSE images presented in Figure 2.1, dislocations appear with a width of several pixels (30 nm width for the steel at this accelerating voltage, *i.e.*, 4–5 pixels wide). However, in Figure 2.5, some isolated pixels are detected as potential dislocation pixels. An additional user-defined parameter is used to fix the minimum size of dislocations present in the images to remove the isolated pixels from the dislocation clusters

Finally, for each mini-series, *i.e.*, each set of orientation conditions, clustered maps are calculated, where the matrix is plotted in dark and the dislocations pixels are shown in green, as shown in Figure 2.6.

Figure 2.6 shows dislocation clusters with thicknesses greater than those in the original BSE image (red arrows, Figure 2.6). It is possible to refine the detection parameters to obtain a thinner thickness; however, a loss of information can occur for dislocations that appear with lower contrasts (yellow arrow, Figure 2.6). The average thickness of the dislocation must be considered in the calculation of the dislocation density. Indeed, because the dislocations are not thicker than one pixel, counting the total number of green pixels in Figure 2.6(b) means counting the same dislocation several times in the measurement of the total length of dislocation lines used in the density calculation. To avoid this, the total number of pixels detected as dislocations is divided by the average thickness of each dislocation, and the pixels contained in the other grains are removed manually before the calculation of the dislocation density. It is possible to count the number N of dislocations appearing in green in Figure 2.6(b) to determine the dislocation density in the image series (with the formula $\rho = N/S$ described in the following section).

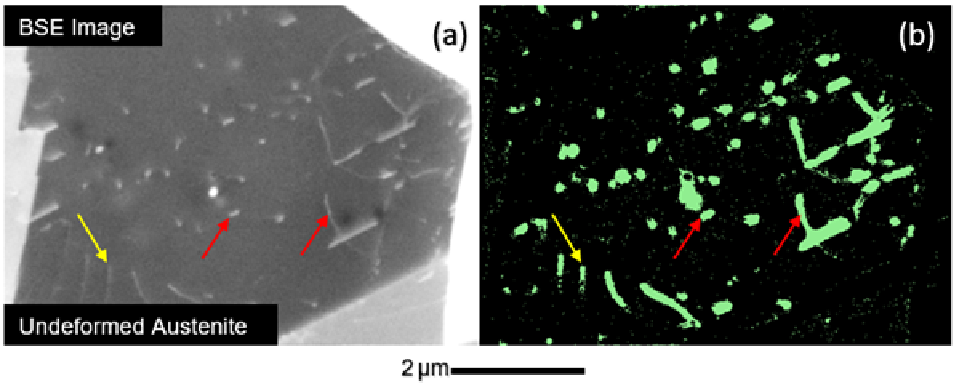

Figure 2.6: Example of clustering result (b) with the corresponding BSE image (a), where dislocations are shown in white on a black background. The clustering result shows the pixels detected as dislocations in green on a black background. Some well-defined dislocations on the BSE image (red arrows) appear with large thicknesses in (b) while more diffuse dislocations have comparable thicknesses (yellow arrow).

Currently, the clustering algorithm shows good results (which will be detailed in the following chapters). However, although it seems to be a promising tool, several problems are still present. The dislocations close to each other are not differentiated by the algorithm and clustered into a single cluster by taking also the pixels of the matrix lying between the dislocations. Moreover, the contrast that varies according to the position in a deformed grain makes the clustering inhomogeneous and makes the apparent thickness of the clusters vary. To solve these problems, it is possible to divide the image into several areas in order to apply different parameters depending on the conditions (edge of the grain, strong or weak contrast, dislocations close to each other) that could improve the clustering results.

2.4 Results

2.4.1 Preliminary calculation of the measurable dislocation density

The dislocation density is calculated using the following formula: $\rho_{clus} = \frac{L}{V}$

After data treatment, the total number of dislocation pixels N^{dislo} is determined. The total length of the dislocations is then calculated using:

$$L^{dislo} = \frac{N^{dislo} \times P_S}{E} \tag{2.3}$$

With E the mean thickness of dislocations (in pixels), and P_S the pixel size in nm.

$$E = \frac{E^{app}}{P_S} \tag{2.4}$$

With E^{app} the apparent dislocation width in nm.

$$\rho = \frac{N^{dislo} \times P_S}{S \times t \times E} = \frac{N^{dislo} \times P_S^2}{N^{tot} \times P_S^2 \times t \times E^{app}} = \frac{N^{dislo}}{N^{tot} \times t \times E^{app}} \tag{2.5}$$

With t the analyzed sample thickness (in nm), and S the analyzed surface in nm^2. N^{tot} is the total number of pixels on the image. Therefore, the dislocation density ρ only depends on E^{app} measured manually on the image.

The determination of the analyzed thickness is difficult to achieve experimentally. Previous studies [ZAE 14] [GUT 12][BIS 11] considered that the analyzed thickness depends on the orientation conditions of the sample, and can be approximated as $t = 5.\xi_g$ with ξ_g the extinction distance corresponding to the diffracting vector $\overrightarrow{g}$. This value thus depends on the orientation condition of the sample, and will not be the same for all images of a given series. It will range from 70 nm for austenite in ($\overrightarrow{g_{11\bar{1}}}$) orientation, to 115 nm for ferrite ($\overrightarrow{g_{220}}$) orientation. For sake of simplification, and for both phases, the analyzed thickness was set to 100 nm for all conditions. The impact of this approximation on the measurement will be discussed later in the text.

However, the observations show that the width of dislocations E^{app} no longer evolves beyond a given magnification. Two images of the same area were acquired on a ferrite grain under the same experimental conditions, one with a pixel size of 4.5 nm (1024 × 768 pixels) Figure 2.7(a) and the other with a pixel size of 2.25 nm (2048 × 1536 pixels) Figure 2.7(b). One can see that there is no difference in the apparent width of the dislocations (27 nm in that case). Therefore, in order to limit the acquisition time, all acquisitions performed on this material were made with a pixel size of 4.5 nm.

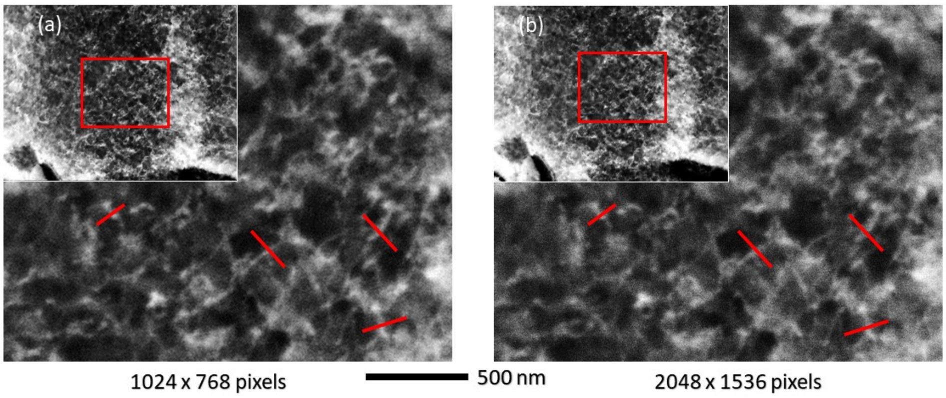

Figure 2.7: BSE image acquired on a ferrite grain deformed at about 3%. For each image, the dislocation lines are visible in white on a black background. Each image was acquired with an acceleration voltage of 20 kv, an aperture of 120 μm and an acquisition time of 3.7 minutes. (a) Ferrite grain observed with a pixel size of 4.5 nm. (b) Same area as image (a) but with a pixel size of 2.25 nm. Dislocation widths were measured perpendicular to the dislocation line. The red lines represent examples where identical widths were measured.

Considering a pixel size of 4.5 nm and an image size of 1024 pixels × 768 pixels, a theoretical dislocation density was calculated. Arbitrarily, the minimum density was chosen to corresponds to an image where 1% of the pixels are dislocation pixels. Applying equation (2.5) leads to a theoretical minimum value of 3.45×10^{12} m^{-2}.

On the other end, the maximum density measurable cannot exceed the total number of pixels. Arbitrarily, the maximum dislocation density is chosen to corresponds to an image where 50% of the pixels are dislocations pixels. It leads to a maximum theoretical dislocation density of $1.73 \times 10^{14}\text{m}^{-2}$.

These limits are indicative and should be reconsidered in the light of experimental results and associated measurement biases.

2.4.2 Experimental measurement of high and low dislocation densities

Two sets of BSE images were acquired for the experimental tests: the first one on an undeformed ferritic grain and the second one on a 3% deformed austenitic grain (Figure 2.1(a) and (d)). The clustering method applied on these two sets of images is presented in Figure 2.8, with the dislocation pixels detected in green on a black background. The measured densities are $\rho_{clus} = 5.8 \times 10^{12}\text{m}^{-2}$ for the undeformed ferritic grain and $\rho_{clus} = 5.7 \times 10^{13}\text{m}^{-2}$ for the 3% deformed austenitic grain. ρ_{clus} was calculated using the following formula:

$\rho_{clus} = \frac{L}{V}$ with $L = \frac{N_{dislocation}}{E} \times P_s$, where $N_{dislocation}$ is the number of pixels detected as dislocations, E is the average dislocation thickness, and P_s is the pixel size.

it is important to remember that the dislocations have an apparent width of several pixels, which depends on the observation conditions and the observed material. Using the total number of dislocation pixels in the image, the length of one dislocation is counted several times because of the thickness of several pixels. Therefore, to determine the appropriate length of the dislocation, its apparent length should be divided by its apparent thickness.

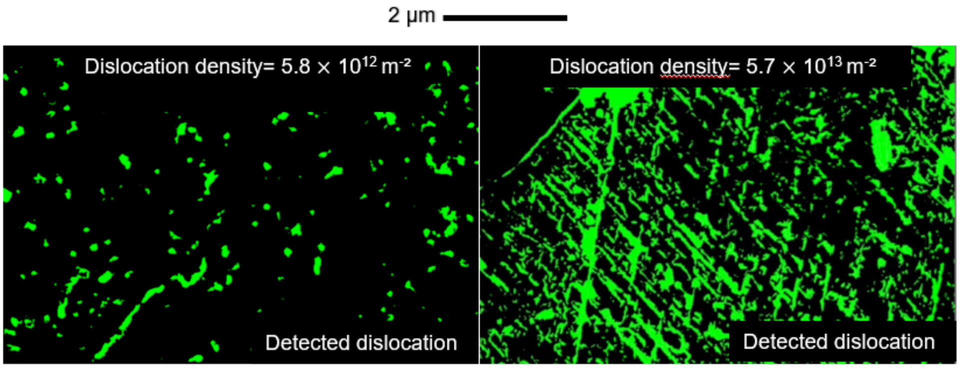

Figure 2.8: (a) Clustering image of an undeformed ferrite grain, where dislocations appear in green on a black background. The dislocation density measured on this grain is equal to $5.8 \times 10^{12}\mathrm{m}^{-2}$. (b) Clustering image of a 3% deformed austenite grain, where dislocations appear in green on a black background. The dislocation density measured on this grain is $5.7 \times 10^{14}\mathrm{m}^{-2}$

Additionally, for validation purposes, the dislocation density was measured on the clustered image presented in Figure 2.8 using the $\rho = N/S$ method, which consists of counting the number of dislocations N visible on the image and dividing it by the surface of the image. The density measurements obtained are $\rho_{N/S} = 5 \times 10^{12}\mathrm{m}^{-2}$ on the undeformed ferritic grains and $\rho_{N/S} = 4 \times 10^{13}\mathrm{m}^{-2}$ for the austenitic grains deformed at 3%. The difference between these values originates from the different uncertainties of measurement, in particular, the one on the volume which is not considered with the N/S method but also from the overlapping of the dislocations and the fact that it is difficult to really detect everything with the clustering algorithm. However, the measurements are of the same order as those obtained by the clustering method, which validates the last step of the clustering method.

2.4.3 Estimation of the dislocation density measurement error

2.4.3.1 Measurement error for clustering

The dislocation density measurement uncertainty arises from three main factors: the first one is related to the apparent thickness of the dislocation and the selection of the pixel size and magnification, the second one is related to the projection of the 3D analyzed volume onto a 2D image, and the third one is related to the dislocation overlapping.

It is possible to quantify the measurement error from the apparent thickness of the dislocations E. As this value is obtained with a precision of one pixel it is possible to repeat the previous calculations with $E' = E \pm 1$ pixel. These calculations show that this measurement of the average thickness E of the dislocations causes an error of 6%–7% in the measurements.

The second effect that leads to uncertainty in the dislocation density measurement is linked to the projection of the analyzed volume. The apparent length of a given dislocation on the 2D projected surface is highly dependent on its orientation in the analyzed volume. For instance, a dislocation that is strictly parallel to the surface will be counted with its real length, whereas a dislocation perpendicular to the surface (red dislocation, Figure 2.9(a)) will appear as a point on the projected image (red circle Figure 2.9(b)), and its length will be underestimated.

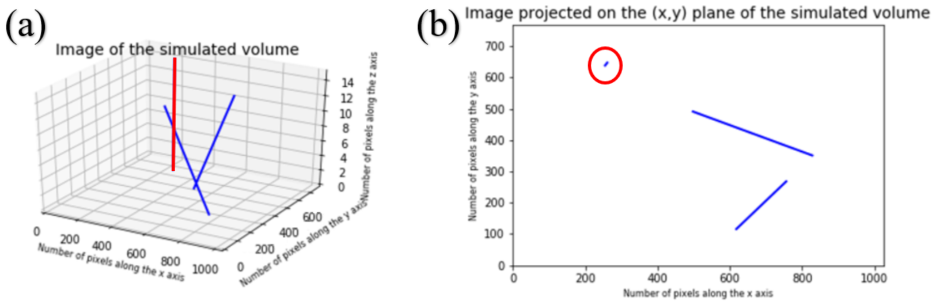

Figure 2.9: (a) Example of dislocation (in blue) obtained with a random direction in a three-dimensional volume and a red dislocation that is almost perpendicular to the (X,Y) plane. The simulated volume is comparable to the experimentally explored volume. (b) Projected image of the volume on the (X,Y) plane with the dislocation almost perpendicular to the surface, which appears as a point (red circle).

Volumes containing a given number of dislocations (plotted as straight blue lines, Figure 2.9(a) were simulated, and the projections of those dislocations on a 2D image were calculated (Figure 2.9(b)). In the case presented in Figure 2.9, the volume and surface sizes were close to those typically required for dislocation images in ECCI (1024×768 pixels, a pixel size of 4.5 nm, and a depth of approximately 100 nm). The orientation of the dislocations was randomly selected by taking randomly generated points in the considered volume. A direction was then randomly selected in a sphere around this point to draw a line that entirely crosses the volume.

The real dislocation density was calculated from the 3D volume:

$$\rho_{real} = \frac{\Sigma \left\| d_{3D} \right\|}{V} \mathrm{m}^{-2} \tag{2.6}$$

Where d_{3D} is the total length of each dislocation.

To estimate the uncertainty resulting from the projection of these 3D objects on a 2D surface, the projected density was estimated:

$$\rho_{projected} = \frac{\Sigma \|d_{2D}\|}{V} \tag{2.7}$$

Where d_{2D} is the total projected length of each dislocation.

The measurement error M was calculated using the densities obtained with the linear coordinates in 3D and 2D using the relation:

$$M = \frac{\rho_{real} - \rho_{projected}}{\rho_{real}} \tag{2.8}$$

M as plotted in Figure 2.10. M increased up to 6% for densities of 2×10^{12} m^{-2} and then fluctuated between 5% and 7% for higher densities values. For the maximum density achievable using the present method, $M = 7\%$. Oscillations in the error measurement are attributed to the random orientation of the generated dislocations. When a dislocation is generated parallel to the projection surface, its contribution to this source of error is zero. In contrast, if it is generated perpendicular to the projection surface, its contribution will be maximum. The rapid increase and fluctuation of the error source for low dislocation densities is attributed to the small number of dislocation lines being present in the volume. Thus, each dislocation will have a significant impact on the difference between the real and projected density. However, by increasing the number of dislocations, the proportion of dislocations oriented perpendicular to the surface compared with all others is necessarily reduced, which has the effect of reducing the percentage of error of a measurement.

Therefore, the measurement error due to the projection remains small because the depth (approximately 100 nm) is very small compared with the surface size (4608 nm × 3456 nm). This makes the contribution to the total dislocation length along the z axis small compared with the lengths along the x and y axes.

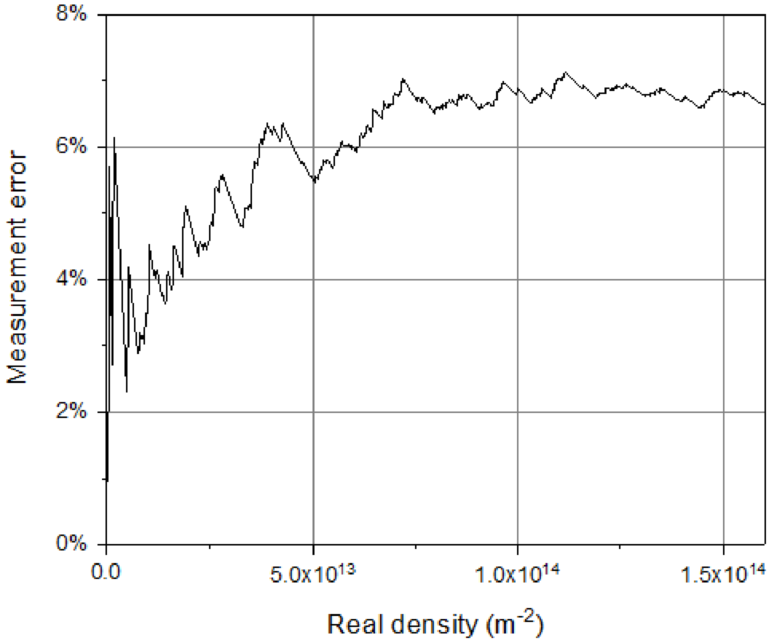

Figure 2.10: Measurement error between the real and projected density.

The third measurement artifact arises from the fact that if dislocations overlap, the total dislocation length will be underestimated. Indeed, the total dislocation length is calculated using $L = N_t \times P_s$, where N_t is the number of dislocation pixels identified and P_s is the pixel size.

If two dislocations overlap, the area of overlapping will be counted only once, whereas it should be counted twice. Therefore, for a higher density, the potential overlapping is higher, and thus, the measurement error is higher. As an estimate, the so-called apparent dislocation density was calculated using $\rho_{apparent} = \frac{N_t \times P_s}{V \times E}$, where E is the thickness of a dislocation in number of pixels, N_t is the total number of dislocation pixels, and P_s is the size of a pixel in nanometers.

To visualize the effect of overlapping, the real density contained in the volume is plotted as a function of the apparent density in Figure 2.11.

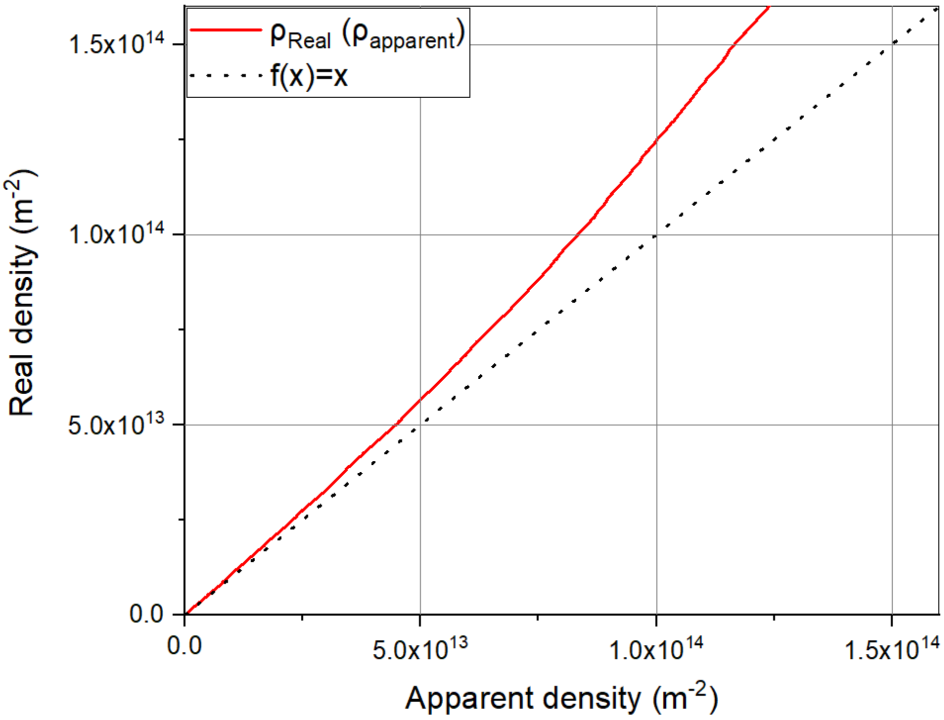

Figure 2.11: Representation of the real dislocation density, obtained in a three-dimensional volume, as a function of the apparent density obtained on a projected image of the volume. The divergence that appears comes from the overlapping dislocations.

As expected, the difference between the real density and the apparent density increases with increasing dislocation density. The apparent density deviates by a few percent for densities below 4×10^{13} m^{-2} and by 20% for densities close to 10^{14} m^{-2}, which is close to the maximum achievable densities.

As a conclusion, the main source of measurement error comes from the overlapping of dislocations, with a higher density resulting in a higher measurement error. For highly deformed materials, the maximum density achievable using the method is close to 10^{14} m^{-2}, for which an error of 20% due to potential overlapping is present.

2.4.3.2 Measurement error for N/S method

In order to compare the measurement obtained by clustering to a traditionally measured value, an N/S type measurement was used, requiring to consider the projection effects. Indeed, this method is particularly effective when all dislocations are perpendicular to the surface. In this configuration, their length L located in the observed volume becomes equal to the depth t. Considering $\rho = N/S$ removes questions about the explored volume and simplifies the calculation. However, this configuration where the dislocations are perpendicular to the surface is a special case.

From the dislocation simulation (Figure 2.9), it is possible to obtain information about the measurement error of this method by imposing directions on the dislocations or by changing the depth. The difference between the real dislocation density (dotted curve), with the one obtained using $\rho = L/V$ (black curve), and the one measured by for $\rho = N/S$ (blue curve) are shown in the Figure 2.12. The difference between the blue curve (Figure 2.12) and the dotted curve is related to the orientation of dislocations with respect to the surface. In the used simulation conditions, a correction factor of 4.47 is required in the case of randomly oriented dislocations. When the analyzed depth t is modified, the apparent dislocation slightly varies, as revealed by the red curve ($t/3$: correction factor 6.63) and green curve ($3t$, correction factor 3.74). Therefore, there is a slight effect of the analysed depth as well.

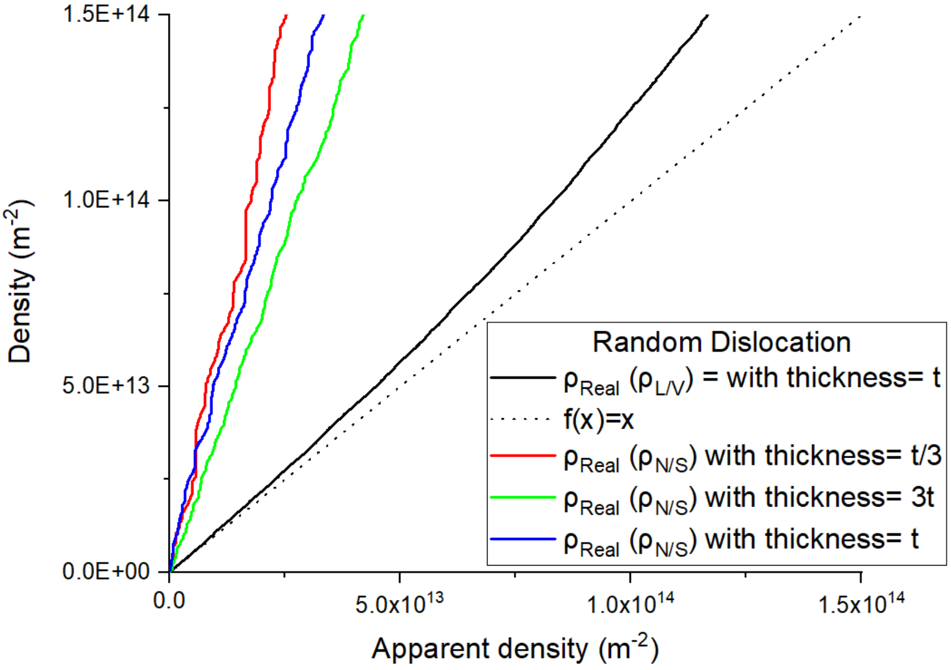

Figure 2.12: Representation of the real dislocation density, obtained in a three-dimensional volume, as a function of the apparent density obtained on a projected image of the volume (black curve) with a depth equal to t. Representation of the real dislocation density as a function of the density measured by the number of dislocations N divided by the projected image area for three different depths t (blue curve), 3t (green curve) and t/3 (red curve).

Therefore, a corrective factor must be applied to the density measurements by the N/S method when the dislocations are in random orientations. When the dislocations have a particular orientation, *i.e.* they are all vertical in the explored volume (or perpendicular to the observed surface) then the density measured by the N/S method is perfectly equal to the real density (blue curve Figure 2.13). However, in the opposite case, if all dislocations are horizontal (or parallel to the observed surface) then the measurement obtained by the N/S method is very far from the real value (red curve Figure 2.13).

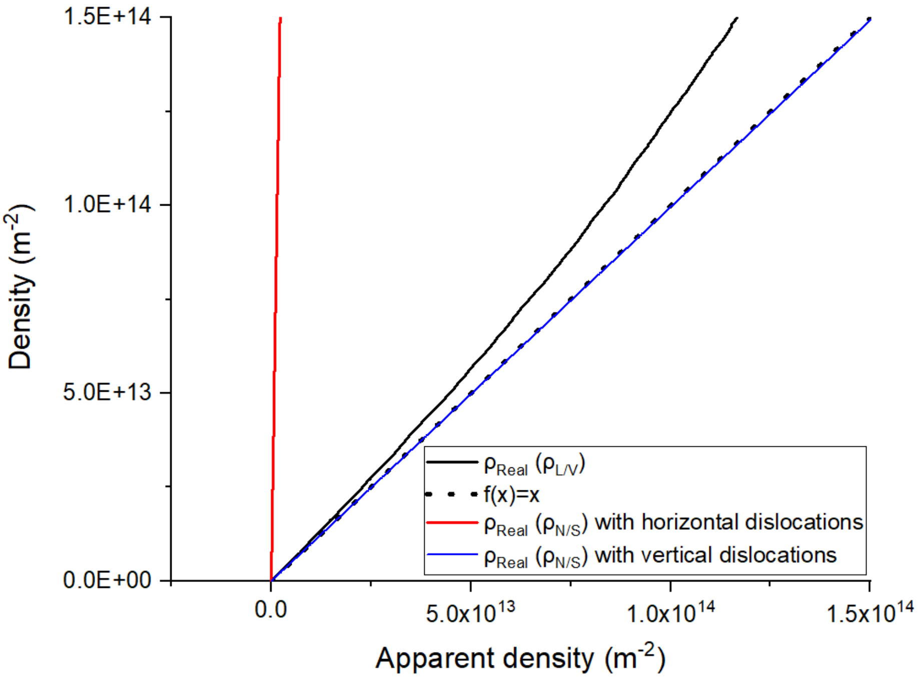

Figure 2.13: Representation of the real dislocation density, obtained in a three-dimensional volume, as a function of the apparent density obtained on a projected image of the volume (black curve). Real dislocation density as a function of the density measured by the number of dislocations N divided by the projected image area for two configurations: dislocations parallel to the surface (blue curve) and perpendicular to the surface (red curve).

Therefore, the correction factor to be applied does not only depend on the analyzed depth but also on the inclination of the dislocations in the material. This factor decreases to 1 when all dislocations are perpendicular to the surface (blue curve Figure 2.13), and increases to 68.27 (red curve Figure 2.13) when all dislocations are parallel to the surface.

As this correction factor depends on the volume and orientation of the dislocations, it is in fact a parameter related to the material and orientation as well. For the following the correction factor used is the one obtained for randomly oriented dislocations and for a depth t, *i.e.* 4.47.

In Figure 2.14, the results obtained during this study on the two grains characterized with the clustering method (Figure 2.8) are presented. The measurement obtained with clustering (in green, Figure 2.14) calculated from the series of BSE images is compared with a traditional N/S measurement (in blue, Figure 2.14) measured on a single BSE image per dislocation observation condition. Considering the different sources of measurement error presented previously, the results obtained are comparable in their order of magnitude and the measurement uncertainties are superimposed.

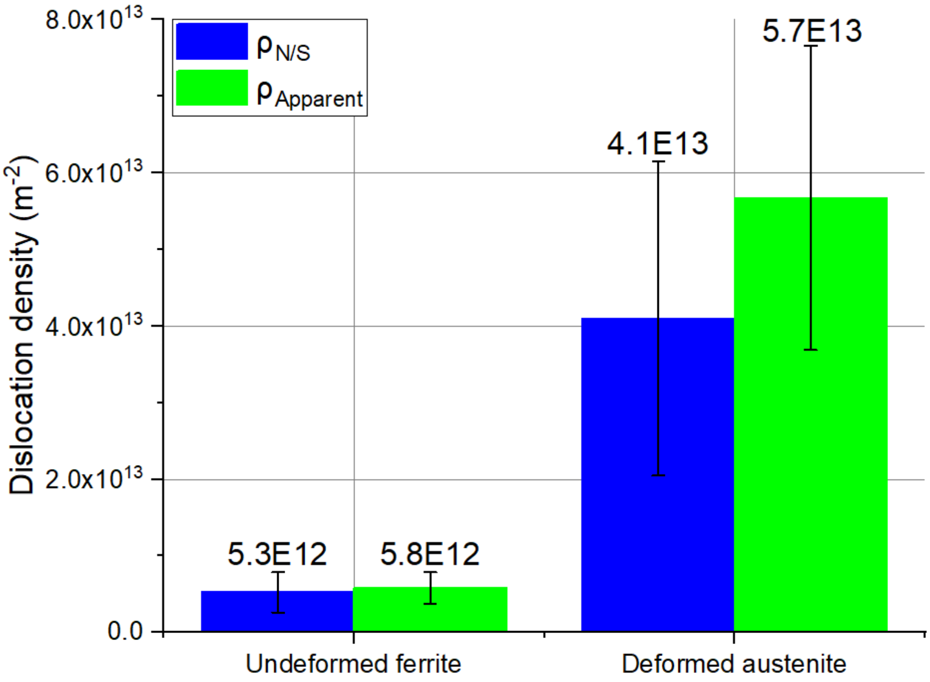

Figure 2.14: Representation of the dislocation density measured for two different grains: a non-deformed ferrite grain and a 3% deformed austenite grain. The measure of dislocation density obtained by clustering (in green) is compared with another measure (in blue) taken directly from the images, which consists of dividing the total number N of dislocations visible on the image by the surface of this image.

2.5 Discussion

The method presented in this study indicates that it is possible to measure dislocation densities semi-automatically on deformed materials by switching to a local average of the grain intensity profile around the analyzed pixel. Two examples were provided, the first on an undeformed ferrite grain, where the measured dislocation density was $5.8 \pm 0.6 \times 10^{12}$ m^{-2}, and the second on a 3% deformed austenite grain, where the measured dislocation density was $5.7 \pm 1.1 \times 10^{13}$ m^{-2}.

This methodology was tested on several duplex samples, and the analysis on a deformed grain was performed on an austenite grain in which the dislocations were relatively easy to image with little noise, thus facilitating the post-processing steps by clustering. Having fewer sharp dislocations with more noise can lead to an additional loss of information during the comparison of intensity profiles because the local average will be distorted. Nevertheless, this problem can be avoided because the first step of the method allows a "feature map‘' to be obtained, which highlights in green all the profiles of the pixels showing a substantial difference with the neighboring profiles. It is therefore sufficient to determine the minimum size of the clusters to be analyzed to remove all the pixels that do not form a dislocation. The method, however, remains dependent on the quality of the acquired images and the polishing state of the material, which must be perfect.

It was demonstrated by calculation that dislocation densities in the range of 10^{12} m^{-2} to 1.2×10^{14} m^{-2} can be precisely measured. These limits correspond to dislocation density measurements in the literature for undeformed steels. For example, Ruggles *et al.*[RUG 20] observed densities between 10^{13} and 10^{14} m^{-2} in an austenitic sample, as did Zaefferer *et al.*[ZAE 14], who reported a dislocation density of 2×10^{13} m^{-2}. Higher densities are expected in deformed steels, as measured by ECCI and TEM by Gutierrez-Urrutia *et al.*[GUT 12], who observed densities ranging between $(10 \pm 4) \times 10^{13}$ and $(17 \pm 6) \times 10^{13}$ m^{-2}. In addition, Bissey-Breton *et al.* [BIS 11] observed a dislocation density of 4.2×10^{13} m^{-2} in a recrystallized bulk copper. In semiconductors, the measured density has been reported to range between 10^{11} and 10^{13} m^{-2} [HIT 14],[SHA 21].

It is nevertheless important to specify that these boundary measurements consider values inherent to the observed materials; such as the apparent thickness E and the explored volume, which are both dependent on the material and the crystallographic orientation. During this study, several different materials were examined using ECCI. Images recorded in the same conditions allowed to measure apparent thickness E for copper (22 ± 2) nm, ferrite (30 ± 2) nm, austenite (32 ± 2) nm, and nickel (27 ± 2) nm. Moreover, in ECCI images, the apparent thickness E of the dislocations may also depend on the observation conditions of the sample, as reported by Kriaa *et al.* [KRI 17], who obtained an apparent thickness of 30 and 19 nm on the same dislocation, depending on the channeling conditions selected. It is therefore preferable to define an apparent dislocation thickness per observation condition and not an average value for all conditions.

This study has shown that the measurement error due to the orientation of the dislocations relative to the surface is negligible and that the main source of uncertainty originates from the overlap of dislocations as the dislocation density increases. It gives a measurement error of approximately 3% for low densities of approximately 10^{13} m^{-2} and 20% for the limit densities of 10^{14} m^{-2} achievable with this method. This uncertainty, due to the overlap of dislocations, also exists for dislocation densities measured from TEM images. Considering a typical TEM image, with a surface size of 4008 × 2664 pixels, a pixel size of 0.55 nm, and a dislocation width of 6.5 nm, the uncertainty is approximately 5% for densities close to 10^{14} m^{-2} and can increase to 20% for maximum densities of 3×10^{14} m^{-2}. The precision of the measurement is thus drastically better for TEM vs. SEM-ECCI, as for the same density, the SEM results in an uncertainty of 20%, whereas that for TEM is only 5%. This is mainly because the higher spatial resolution of TEM allows the dislocations to be better discriminated. However, TEM is more localized than SEM, and the question of representativeness can always arise.

The second major source of error originates from the apparent thickness of the dislocations E, obtained from BSE images, which were measured at one-pixel accuracy, resulting in a measurement error of 6% to 7%. When added to the other contribution to the measurement error, the total measurement error for 10^{12} m^{-2} is 15% and it is 34% for 10^{14} m^{-2}.

Finally, the main source of error is associated with the explored depth, which is directly related to the probed volume. The calculations were here performed considering the deepest condition in each mini-series (around 100 nm). However, the theoretical value of $5\xi_g$ varies within an image miniseries. As an example, it varies from 70 nm (g_{111}) to 150 nm (g_{311}) for austenite. But, surprisingly, we observed that the number of visible dislocations was quite similar for the different conditions, *i.e.* for the different theoretical analyzed depth, additional observations on this phenomenon are made in the next chapter. For those reasons, the uncertainty of the quantitative measure is yet about the order of magnitude (this question will be further analyzed in the next chapter). However, when comparing different deformed states, for the same material acquired under the same experimental conditions, the measurement uncertainty shall be close to the one previously calculated (15 to 34%). A better quantification of the explored depth is thus necessary, and could be determined experimentally by the stereo pairs method [SIM 96],[Já 18], or by combining TEM and SEM observations of the same sample. Picard *et al.* [PIC 14a] simulated ECCI images as a function of the explored thickness. A comparison between simulated and experimental images could help to specify the explored volume for this orientation. Moreover, the data treatment procedure could be improved by taking into account the nature of the Kikuchi bands crossed, which is theoretically possible as each intensity profile is a signature of the orientation [LAF 18].

2.6 Conclusion

In this chapter, an approach to measure dislocation density in deformed materials was presented along with the measurement uncertainty induced by the method. Using a data-classification algorithm based on a local average of the grain around the analyzed pixel, it became possible to obtain a quantitative measure of the dislocation density in a deformed sample without knowing the grain orientation. Moreover, from the imaging data, it was possible to calculate the measurement uncertainties of this method.

The ranges of densities that can be expected are on the order of 10^{10} m^{-2} for semiconductors and can increase to 10^{14} m^{-2} for metallic materials. The main sources of error are the explored volume and the superposition of dislocations. It was also possible to determine the evolution of the error caused by the superposition of dislocations as well as that originating from the apparent thickness of dislocations present in the images. The uncertainty of measurement for these last two points is 27% at most on the highest densities characterizable using this method. This uncertainty does not consider the error made on the analyzed volume. Indeed, a change in the value of ξ_g can lead to errors on the analyzed volume of 20 to 70%. The uncertainty on the volume remains the weak point of the method. Observations have been made in order to specify the volume explored with the ECCI method and will be detailed in chapter 3. However, when comparing different deformed states of the same material acquired in the same experimental conditions, the experimental uncertainty in the density evolution shall be the one that we estimated during this study.

In summary, the R-ECCI method coupled with clustering enabled characterization of the dislocation densities in a material, specifically in a deformed material with the presence of local disorientation. the method seems to be relevant for the study of heterogeneous microstructures that require imaging but also for multiphase materials.

Chapter 3

Investigation of the probed depth with the R-ECCI method

Sommaire

3.1 Introduction

The dislocation density is defined by the total length of the dislocation lines L present in a given volume V :

$$\rho = \frac{L}{V} \tag{3.1}$$

However, as mentioned in the previous chapter, when measuring the dislocation density from electron microscopy images, the determination of the analysed volume remains difficult and leads to large measurement uncertainties.

Determining the explored volume using SEM is very difficult. The depth probed is also difficult to estimate from simulation because of the complexity of the electron backscattering model. However, some studies gave some clue on the depth t probed during ECCI measurements. Wilkinson *et al.* [WIL 93] rely on the channeling contrast theoretical approach [SPE 72] and estimated the maximum depth t to be $5\xi_g$. Using these results, theoretical values of t have been estimated to be around 45 nm and 65 nm by Gutierrez-Urrutia *et al.* [GUT 12] for diffracting vectors of type (110) and (200) and an acceleration voltage of 10 kV for steel. Zaefferer *et al.* realized simulations in duplex steels and found depth around 100 nm for a diffracting vector (111) for austenite. It corresponds to about $3\xi_g$ [ZAE 14]. More recently, Yamasaki *et al.* [YAM 21] showed that in titanium, the depth would be around $6\xi_g$, which corresponds to about 150 nm at 30 kV. As a conclusion, there is yet no consensus about the analysed depth during ECCI. This chapter present an experimental attempt to determine the analysed depth range during ECCI observations.

For TEM observations, the converging beam electron diffraction (CBED) method shows a local accuracy of about 2% [CAR 16][DEL 01], and can be used to measure the local thickness of the thin foil (see chapter 1).

To compare the two imaging methods, a FIB thin foil was extracted from a bulk material and was observed using SEM and TEM.

During TEM observations, the thin foil is tilted from a few degrees to about ten degrees. This tilt changes the probed depth by a few nm (Figure 3.1(a)). Indeed, if the tilt is about ten degrees, a thickness of 150 nm would be measured at about 153 nm, which is within the margin of error of TEM measurement methods. For SEM measurements, the probed depth (Figure 3.1(b)) does not depend on the tilt of the material and remains unknown.

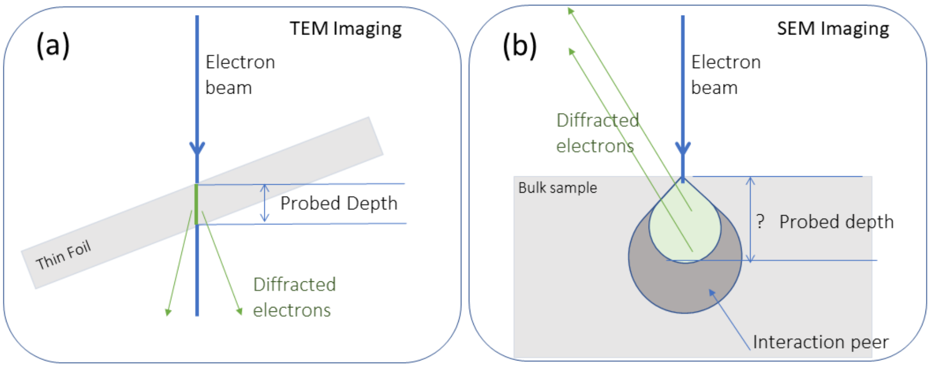

Figure 3.1: Ilustration of probed depth in TEM (a) and SEM (b).

TEM and SEM observations were made on the same Focused Ion Beam (FIB) thin foil. The objective of this chapter is not to directly answer the question of the volume explored but to provide elements of comparison with these two dislocations imaging methods. Indeed, during the TEM image acquisitions (Figure 3.2(a)), the whole slice is observed and the projected image obtained allows to observe the whole length of dislocations contained in the area (Figure 3.2(c)). For ECCI, the probed detph depends on the extinction distance ξ_g and the expected value for a duplex sample is less than a hundred nanometers. This is why a FIB thin foil of about 150 nm thickness was machined in order to observe differences between TEM and SEM images. Indeed, for ECCI images, the measured dislocation length depends on the analyzed depth (Figure 3.2(b)), which implies that the part outside the probed depth will be invisible on the SEM projected image (Figure 3.2(d)).

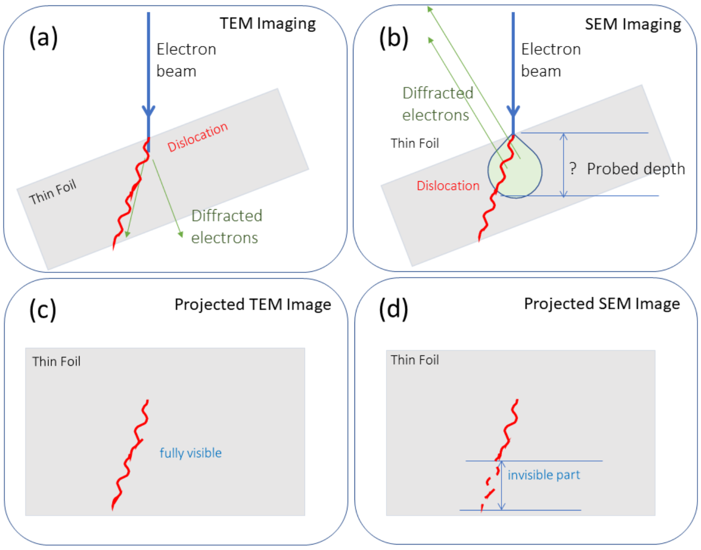

Figure 3.2: Thin Foil observed by TEM (a) and SEM (b) with a dislocation in red. Projected image of the thin foil where the red dislocation is fully visible in TEM (c) but partially visible in SEM (d).

This difference between the apparent lengths of the dislocations in the TEM and SEM images must be related to the ξ_g extinction distance and may provide answers to the volume analyzed by SEM.

3.2 Materials and method

3.2.1 Materials

Observations were made on the same commercial Outokumpo 2101 presented in the previous chapter. The sample was mechanically ground, with final polishing was performed using a 1 µm diamond solution. To avoid any strain hardening of the surface, a final electropolishing step was performed using an A2 electrolyte (from Struers APS, Denmark) at 20 V for 60 s with the Lectropol 5 device (Struers APS, Denmark) SEM-ECCI imaging of the dislocations were performed on a Zeiss Supra 55VP with an accelerating voltage of 20 kv, a diaphragm of 120 μm and a pixel size of aproximately 3 nm. TEM imaging was performed on a JEOL 2100 LaB6 TEM with an accelerating voltage of 200 kv.

3.2.2 FIB Thin foil

The microscope used combines a Gemini I column (Carl Zeiss Microscopy GmbH, Oberkochen, Germany) and a standard proven solid-state BSE detector (El-Mul Technologies Ltd., Rehovot, Israel).

EBSD maps were acquired in order to select the most appropriate grain. The choosen austenitic grain allows to have the normal of the thin foil close to a zone axis (Figure 3.3). Several different two beams conditions are reachable within the available tilt angles of the sample holder used. The formation of the thin foil can suppress many dislocations inside the grains by image force effect [KOH 20]. It is therefore necessary to have several different observation conditions in order to increase the number of visible dislocations to be able to compare the two imaging methods (TEM and SEM).

It was decided to choose an austenite grain because the dislocation density there was slightly lower than in ferrite (according to the observations made in Chapter 2), with, on average, a density of $(1.5 \pm 0.1) \times 10^{14}$ m^{-2} for austenite and on average of $(2.5 \pm 0.2) \times 10^{14}$ m^{-2} for ferrite in this sample. Moreover, in the austenite grains, the dislocations appear less diffuse and with a more contrasted, which facilitates their observation.

The EBSD acquisition performed on the thin foil shows an austenite grain positioned between these two zones (Figure 3.3, red zone) and oriented near a zone $< 111 >$. All observations will be made on this austenite grain. The measurement of the grain thickness has been done using the CBED procedure detailed in chapter 1.

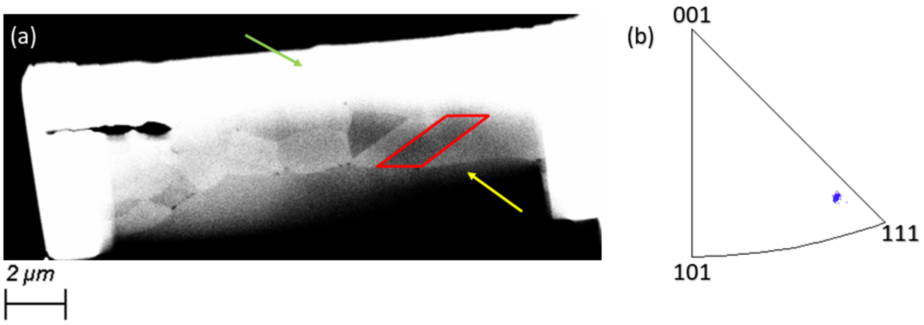

Figure 3.3: (a) BSE image of a FIB thin foil of a duplex sample. Red zone: selected austenite grain near a zone axis (b) Inverse Pole Figure (IPF) along the axis normal to the selected grain. The grain was chosen because it is located between the white area (green arrow) and the black area (yellow arrow) which are difficult to image.

The measurement of the thin foil thickness in the middle of the selected grain was performed using the CBED method (see Chapter 1). A value of (144 ± 20) nm was found.

3.2.3 SEM and TEM orientation

The orientation of the FIB thin foil was obtained by EBSD and confirmed by the CHORD method which allows to link the intensity profile to an orientation [LAF 20][LAF 18][LAF 21]. By creating a database of simulated intensity profiles, it is possible to match the experimental profile to a known orientation.

Knowing the orientation of the grain, the corresponding ECP can be calculated (Figure 3.4). This pattern can then be used to plot the crystallographic path followed during the 360° rotation performed at 10° tilt. It consists of a circle of 10° diameter, where the starting point (*i.e.* rotation angle of 0°), is represented in red. On this crystallographic path, for some rotation angles, a two beam conditions will be crossed. Each of those orientation condition, suitable for dislocation imaging are represented in green. Using this ECP (type of g vector, and rotation angle required).

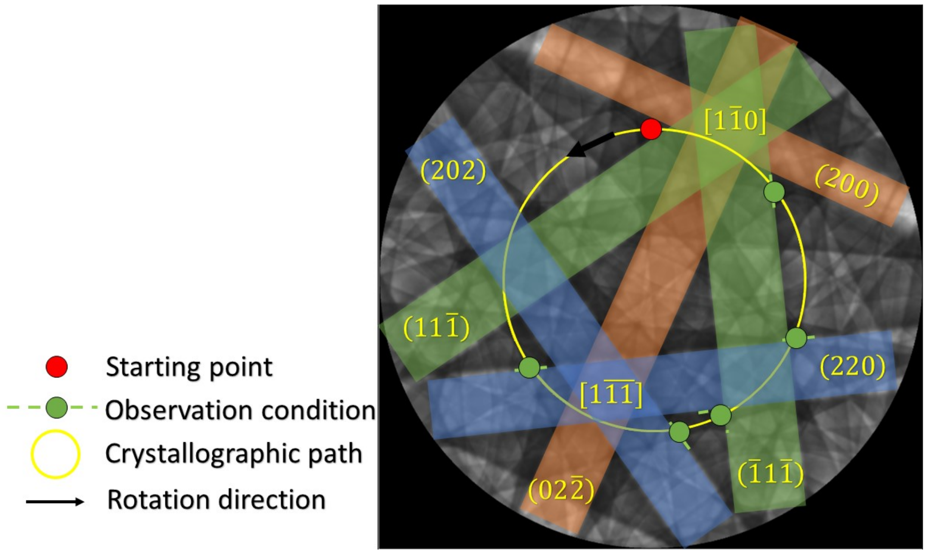

Figure 3.4: Simulation of the ECP of the austenite grain (red zone figure 3.2) obtained with Emsoft [SIN 17][GRA 19] showing the analysed rotation path associated with the R-ECCI method.

The Selected Area Diffraction Pattern (SAED) of the choosen austenitic grain confirmed that its orientation is close to a $[1\bar{1}\bar{1}]$ Zone Axis, Figure 3.5(b). This allows to reach several two Beam condition without applying too large tilt angles. For instance, Figure 3.3(a) is a $g_{\vec{2}20}$ two beam bright field, where many dislocations are clearly visible within the austenitic grain.

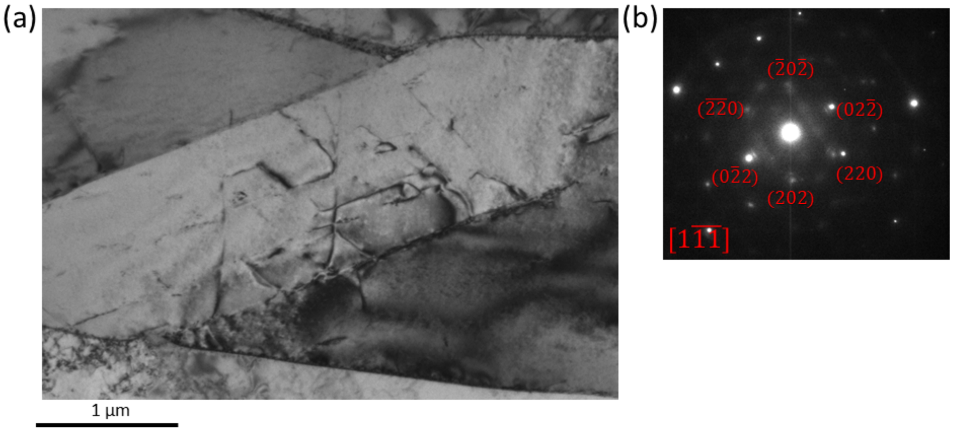

Figure 3.5: (a) TEM-acquired BF image of the selected austenite grain in two beam condition ($g_{\vec{2}20}$). (b) Associated Diffraction patterns of the $[1\bar{1}\bar{1}]$ zone axis of grain (a).

3.3 Results

The geometry of the thin foil creates artefacts that affects the constrast of the images. Therefore, additional post processing steps were required. Curtaining effect from FIB preparation are visible on the top right part of the raw image (Figure 3.6(a), red arrow). It creates a persistent white contrast, visible as a vertical line, which can be removed by using the image processing included in Fiji [SCH 12]. The dislocations on the rest of the grain appear with a good contrast but where the curtaining effect is present (Figure 3.6(a), red arrows), they appear very diffuse and with a low contrast on the top of the grain (Figure 3.6(b), red circle).

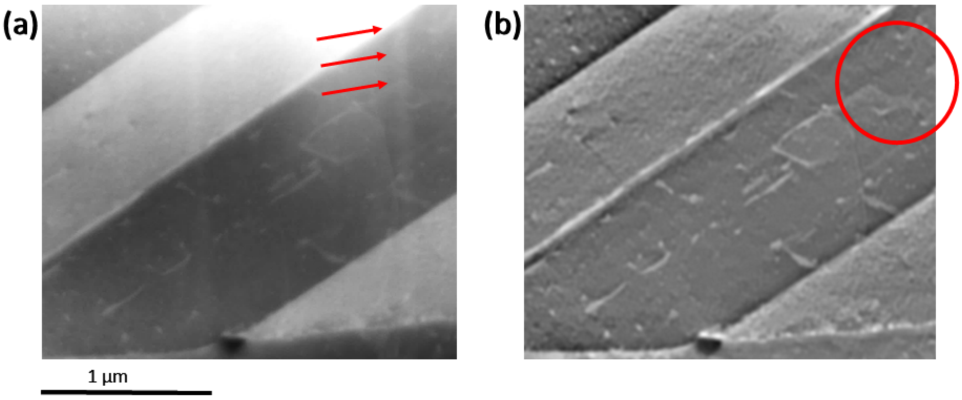

Figure 3.6: BSE image acquired on an austenite grain contained in the thin foil. (a) raw image (b) image after processing. the red arrows show a curtaining effect from FIB and the red circle shows that this effect disturbs the imaging of the dislocations even on the sharp images (blurred dislocation and less contrast).

The tilt angles used in SEM are defined by the rotation during the R-ECCI acquisition, it is of 10° in the present case. For TEM imaging, different tilt angles were chosen so that different two beam conditions could be reached. Therefore, the projection angles of the images acquired by using the two methods are not exactly the same. Consequently, the apparent grain width was different depending on the imaging condition (Figure 3.7). In order to compare the apparent length of the dislocations visible on the two images, the apparent grain width was corrected. The pixel size of each image was changed to obtain an apparent grain width of 1000 nm and to be able to compare the dislocation lengths with the same scale for all diffraction conditions.

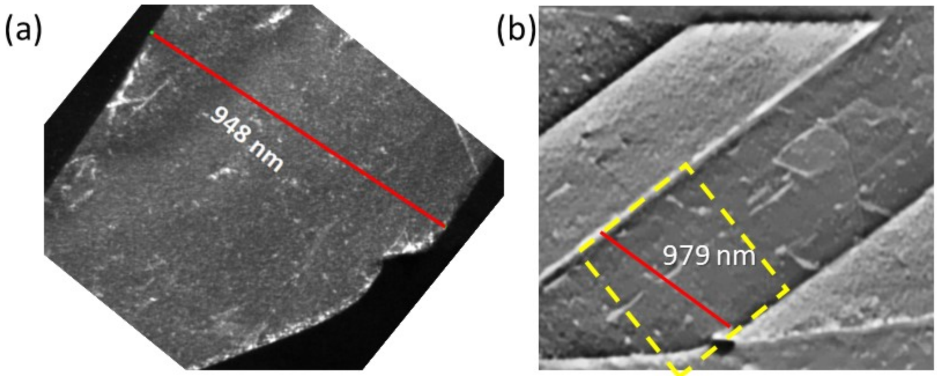

Figure 3.7: (a) TEM image acquired on the bottom of the austenite grain. (b) BSE image acquired on the austenite grain. Due to the different tilt angle used, the apparent width of the grain was slightly different using both methods. The yellow rectangle on the right image represents the part imaged with TEM

Two orientation conditions have been chosen because they provide a better quality of the image: $g_{11\bar{1}}$ and g_{220}.

For the first observation condition, Figure 3.8 shows the comparison of the apparent length of the dislocations selected for the $g_{11\bar{1}}$ diffraction condition. First of all, some dislocations appear in ECCI images and not in TEM one, such as the one circled in red on Figure 3.8. If the same two beam condition was selected, *i.e.* 111 type of plane, it is not sure that the exact same condition was chosen. Therefore, there might be some dislocation that respect the $g.b = 0$ condition in TEM and not in SEM or inversely. However, as the aim of this part is to compare the visible dislocation, only the ones that were identified to be the same on both imaging condition are discussed here.

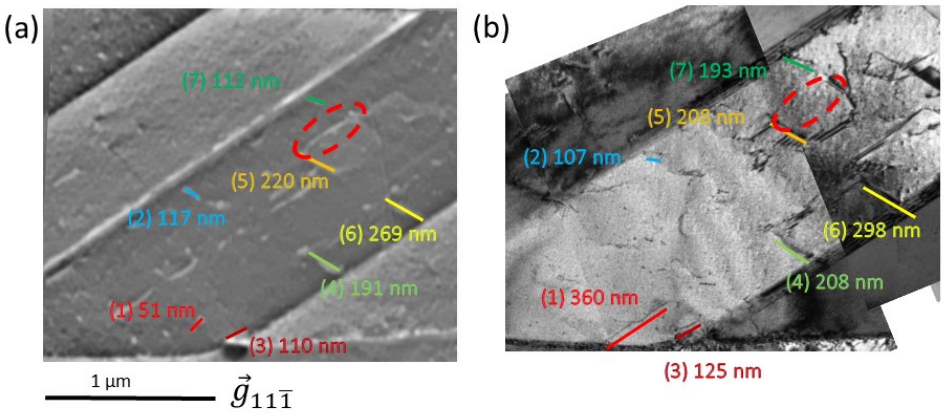

Figure 3.8: Comparison of apparent dislocation lengths between SEM (a) and TEM (b) images for the same diffractant vector $g_{\vec{11\bar{1}}}$ on the same grain. Shows that the apparent lengths of the dislocations are almost always close.

The apparent lengths of the dislocations are summarized in the table 3.1. Most of the dislocation that are visible on ECCI and TEM imaging have similar length if observed from

TEM or ECCI. However, the dislocation noted (1) appear much longer on TEM image compared with the SEM one (360 nm against 52 respectively). There might be several dislocations close to each other, that appear as one on TEM, with only one of them in suitable condition in the case of SEM imaging.

Apparent dislocation length for the diffracting vector of type $\vec{g}_{<111>}$		
	SEM	TEM
1	(51 ±9) nm	(360 ±19) nm
2	(117 ±17) nm	(107 ±5) nm
3	(110 ±17) nm	(125 ±6) nm
4	(191 ±27) nm	(208 ±11) nm
5	(220 ±30) nm	(208 ±11) nm
6	(269 ±36) nm	(298 ±15) nm
7	(112 ±17) nm	(193 ±10) nm

Table 3.1: Comparison of apparent dislocation lengths in TEM and SEM images for the diffracting vector $\vec{g}_{<111>}$.

The second observed condition with the $\vec{g}_{220}$ diffracting vector (Figure 3.9) shows fewer common dislocations between the two acquired images. Moreover, the dislocations in the red circles (Figure 3.9(b)) are only visible in TEM and not in SEM. One of the two dislocations is visible with the first observation condition but its intensity is very low, close to a residual contrast.

The apparent length measurements in TEM and SEM are summarized in the table 3.2. In this case, no difference exceeds the measurement uncertainties.

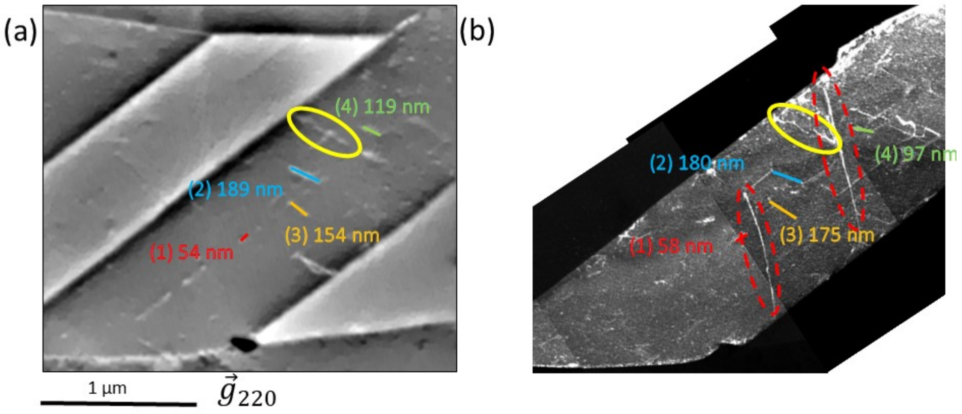

Figure 3.9: Comparison of the apparent length of dislocations between SEM (a) and TEM (b) images for the same diffraction vector $g_{\vec{220}}$.

Apparent dislocation length for the diffracting vector of type $\vec{g}_{<220>}$		
	SEM	TEM
1	(55 ±10) nm	(58 ±3) nm
2	(189 ±26) nm	(180 ±9) nm
3	(154 ±22) nm	(175 ±9) nm
4	(119 ±17) nm	(97 ±5) nm

Table 3.2: Comparison of apparent dislocation lengths in TEM and SEM images for the diffracting vector $\vec{g}_{<220>}$.

Figure 3.10 shows two images taken with the diffracting vector $\vec{g}_{220}$ for two different angles (about 230° and 117°). Normally the same dislocations should be observed however on figure 3.10(b) additional dislocations are visible. This could be caused by an additional diffraction effect from the $(\bar{1}1\bar{1})$ band.

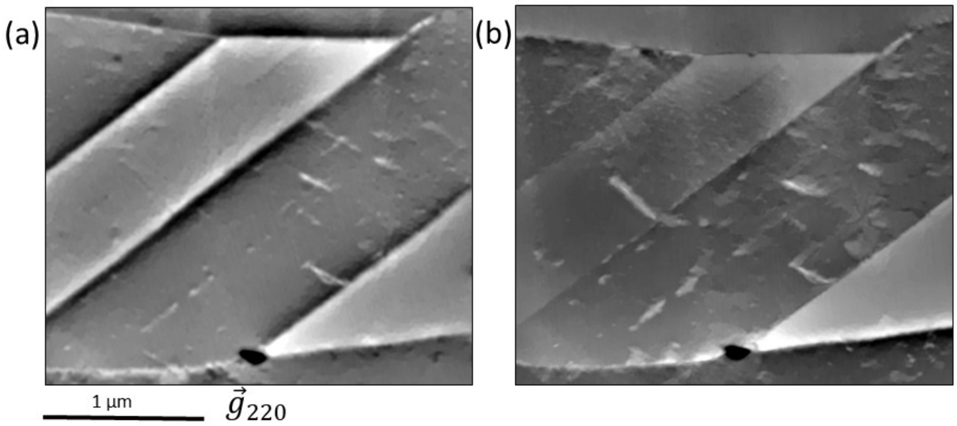

Figure 3.10: BSE image of the $\vec{g}_{220}$ vector obtained for two different angles (about 230(a) and 117°(b)). Additional dislocations are visible on figure (b) whereas the two images should be identical.

3.4 Discussion

All precautions have been taken to have the same orientation conditions in TEM and SEM. However, it is possible that some diffracting vectors are not the right ones. More precisely, it is always possible that the order and sign of hkl in the diffracting vector $\vec{g}_{hkl}$ could be interverted.

Some dislocations do not appear in the TEM images but appear in the ECCI images (Figure 3.8, red circle). In TEM, it is possible to refine the two-beam condition (TB, see Chapter 1) and obtain the diffracted signal by a single diffracting vector, thanks to the double-tilt sample holder. On the other hand, with the R-ECCI method, different diffraction conditions are encountered during the rotation. Depending on the case, it is difficult to determine with certainty whether the two-beam condition is fully satisfied. Therefore, if the two-beam condition is not fully satisfied, dislocations may not be visible. For exemple, in the case $\vec{g}_{<111>}$ shown on Figure 3.8, three observation conditions are close to another Kikuchi band (Figure 3.4). At three degrees past the starting point of the rotation, the $\vec{g}_{<111>}$ condition was acquired and gives the ECCI image shown on Figure 3.8. The image allows to distinguish the dislocations. However, it is difficult to be sure that the two-beam condition was achieved at this rotation angle because of the proximity of the two diffraction bands $\vec{g}_{<111>}$ (green in Figure 3.4) and $\vec{g}_{<200>}$ (orange in Figure 3.4). This may explain why dislocations are seen in the SEM but not in the TEM: in the SEM, the addition of several different diffraction vectors is cumulated in the signal. In addition, a complex contribution of more than one Kikuchi band for a given orientation (corresponding to the position of the incident beam on the ECP) has also been raised by Kriaa *et al.* [KRI 18]. This hypothesis helps to explain the variations in contrast and apparent thickness of dislocations during the acquisition of a series of images obtained along a Kikuchi band.

Nevertheless, this possible error could explain the fact that not the same dislocations are visible on SEM and TEM images. Moreover, the thicknesses observed in the SEM will not change following this type of error and therefore the following conclusions will remain the same.

For the dislocation that were both visible on ECCI and TEM images, similar lengths were observed in both cases. If one consider that those dislocations are randomly oriented in the thin foil, observing the exact same length indicates that a similar depth is probed in the two cases. As the thin foil thickness was measured to be around 140 nm, one can expect that the probed depth in ECCI measurement is of at least this value.

However, in the literature, the probed depth for ECCI is usually described as being of type $n\xi_g$. In the case of $< 111 >$ orientation, ξ_g equals to around 13 nm, this would lead to a minimum n value of 10. In the case of the 220 orientation, ξ_g equals to around 22 nm, which would lead to a minimum n value of about 7.

Zaefferer *et al.* realized simulations in duplex steels and found depth around 100 nm for a diffracting vector (111) for austenite. It corresponds to about $5\xi_g$ [ZAE 14]. However, this simulation is done under perfectly respected two beam conditions and has a higher acceleration voltage than in our study, which increases the value of ξ_g. Yamasaki *et al.* [YAM 21] showed that in titanium, the depth would be around $6\xi_g$. It is difficult to compare these values since all the observations are not made under the same acquisition conditions and it is complex to know if the two-beam condition is perfectly respected.

3.5 Conclusion

In conclusion, the measurements of the apparent lengths of the dislocations by SEM and TEM do not allow to deduce precisely the volume explored in ECCI. Indeed, similar length were measured from TEM and SEM analyses. Under the assumption that dislocations are randomly oriented within the foil, this would indicate that the whole thin foil thickness is probed (approximately 140 nm) during ECCI measurements close apparent lengths in almost all cases.

These results also allow us to revise the approach on the explored volume in R-ECCI for the calculation of dislocation densities. Indeed, under the current observation conditions, it is not possible with R-ECCI to be in perfect two-beam conditions, so that the use of a value of ξ_g must be carefully chosen for the volume calculation.

An average value for the volume of about 150 nm seems to be more consistent with the observed values which are closer to 9 to $10\xi_g$ than $5\xi_g$ and that underestimates the explored volume for diffracting vectors of low indices (hkl). This is particularly true for dislocation density measurements performed on several observation conditions as is the case with the R-ECCI method. However, an uncertainty related to this average must still be specified.

Chapter 4

Experimental measurement of dislocation density in metallic materials: a quantitative comparison between measurements techniques (XRD, R-ECCI, HR-EBSD, TEM)

Sommaire

4.1 Introduction

In Chapter 1, it was shown that dislocations in polycrystalline materials can usually be found either isolated, randomly distributed inside the cells or grains, or localized close to grain boundaries to accommodate possible strain incompatibilities between the different grains. Other dislocations are found to be organized into patterns, in the form of dislocation cells or walls.

As a reminder the total dislocation density ρ_{tot} is often decomposed as [BOR 00],[WAU 15]:

$$\rho_{tot} = \rho_W + \rho_C + \rho_{GB} \tag{4.1}$$

with ρ_W the density of dislocations constituting the cell walls, ρ_c the dislocation density randomly distributed within the cells/grains and ρ_{GB} the dislocation density present at grain boundaries.

This equation can be reduced to the sum of GND and SSD:

$$\rho_{tot} = \rho_{GND} + \rho_{SSD} \tag{4.2}$$

The imaging and indirect measurement methods detailed in chapter 1 allow to obtain a value of the dislocation density. Although different methods have been developed, experimental measurement of dislocation density in metallic alloys remains a challenging task. Indeed, for each measurement method, experimental artefacts induce non-negligible bias that must be considered. Beyond the definition of dislocations from the crystallographic point of view, their modelling implies concepts or units which differs from metallurgical ones at some point (*e.g.*, expressing densities in m^{-1} rather than m^{-2}).

It should be noted, however, that each method does not characterize the same dislocation populations. The TEM and ECCI imaging methods allow theoretically to measure the sum of the densities (GND + SSD). The EBSD and HR-EBSD methods can only measure the density of GND. For the XRD method, as described in chapter 1, opinions differ but seem to be more sensitive to SSD.

Thus, the aim of this chapter is:

- (i) to present some quantitative measurements of dislocation densities performed with the same duplex steel samples using four different characterization techniques and for three different strain levels.
- (ii) To discuss the measurement uncertainties of all used techniques.
- (iii) Discuss the link between the obtained results and the different types of dislocation observed for each method.

4.2 Materials and methods

4.2.1 Materials

Observations have been made on the same type of lean duplex stainless steel Outokumpo 2101 hot rolled as in the previous chapters. This choice is motivated by the presence of two phases, austenite and ferrite, in which the dislocations adopt very distinct arrangements. Indeed, the dislocations appear straight with a high contrast in the austenitic phase, which makes them easy to image. In the ferritic phase, on the contrary, the dislocations appear tortuous with a lower contrast, which makes them more difficult to image. It is therefore interesting to study the performance of measurement methods based on dislocation imaging (ECCI/TEM) for this material and more particularly the R-ECCI method.

The evolution of dislocation density was characterized in both ferritic and austenitic phases. Micro tensile samples (total length 112.5 mm, width 12.5 mm and a thickness of 1.5 mm) were deformed under an optical microscope using a Deben 2000E tensile stage. Using standard Digital Image Correlation (DIC) the deformation was determined on all points of the surface. One sample was deformed to 5% and the other one to 10%. In the present study, the austenite grain size will be impacted by the appearance of martensite in austenite during deformation.

For ECCI and HR-EBSD measurements, samples were mechanically ground, and the final polishing was performed using a 1 µm diamond solution. To avoid any strain hardening of the surface, a final electropolishing step was performed using A2 electrolyte (fromStruers APS, Denmark) at 20 V for 60 s with the Lectropol 5 device (Struers APS, Denmark).

To allow for TEM observations, the duplex samples were mechanically ground to obtain a thin sample of 50 μm thickness. Small discs of 3 mm diameter were subsequently extracted by punching and later electropolished using A2 electrolyte (from Struers APS, Denmark) with the Tenupol-5 device (Struers APS, Denmark). A final ion polishing step was performed using PIPS-II to increase the observable area with an acceleration voltage of 1.5 kv and angles of ±4° for the ion beams for 2 hours.

For XRD measurements, samples were mechanically ground using SiC paper, down to a 1200P.

4.2.2 Methods

The R-ECCI method used in this chapter is the one developed and described in chapter 2.

4.2.2.1 Transmission Electron Microscopy

TEM micrographs were acquired with a TEM JEOL 2100 LaB6 operating at 200kV. For dislocation densities measurements, the intercept method was used [BRA 70b]. It consists in drawing lines of total length l on the image (arbitrary lines or regular grid) and counting the number of intersections n with dislocations. The dislocation density ρ is then calculated using the formula: $\rho = \frac{2n}{lt}$, with t the analyzed thickness. The determination of t was done by measuring the number of thickness fringes [CAR 16]. For a grain in a given two beam orientation, the probed depth z is proportional to the number of bands N observed and the extinction distance ξ_g related to the diffraction vector used: $z = (N - \frac{1}{2})\xi_g$.

The observation of dislocations in TEM is possible in Weak Beam Dark Field (WBDF) mode [COC 69] or in Bright Field (BF) mode. In both cases, it requires to orient the crystal in a

Two-Beam (TB) [HIR 70](see chapter 1) condition (only one diffracting vector $\overrightarrow{g_{hkl}}$). In these conditions, only dislocations with a burgers vector $\overrightarrow{b}$ respecting the relation $\overrightarrow{g_{hkl}} \cdot \overrightarrow{b} \neq 0$ are visible. As a result, for each orientation conditions, different dislocations might be invisible, and the density is then always underestimated when determined from only one orientation condition. Therefore, for each strain rate and for each phase, two to three grains of each phase were oriented in several TB conditions.

4.2.2.2 EBSD and High angular Resolution EBSD

EBSD was conducted with the same microscope as for the R-ECCI acquisitions. Electron BackScatter diffraction Patterns (EBSP) were acquired with an EBSD Symmetry camera (Oxford), an acceleration voltage of 15 kV, an exposure time of 32 ms, an aperture of 60 μm and a pixel size of 50 nm. The EBSP images were averaged by 3 to enhance their signal-to-noise ratio in view of the subsequent HR-EBSD analysis.

The latter is based on a global image registration approach implemented in ATEX-software [BEA 17] (developed at the University of Lorraine). EBSP are considered as a whole, through a unique and large region of interest, whose relative deformations are modelled by a linear homography [ERN 20b]. Often used in computer vision to describe projections, the latter is measured by an iterative inverse-compositional Gauss Newton algorithm, modified to integrate a correction of optical distortions caused by camera lenses [ERN 21]. The reader is also referred to chapters 3 to 5 in [ERN 20a] for all details.

The Nye's dislocation tensor is computed according to the Nye-Kröner theory [NYE 53],[KRÖ 58]:

$$\alpha = \mathrm{curl}\varepsilon + \mathrm{tr}(k_e).I - k_e^T, \tag{4.3}$$

where ε is the elastic strain tensor and k_e the lattice curvatures. These curvatures can be approximated with a finite difference scheme:

$$k_{ij} \cong \Delta w_i / \Delta x_j, \tag{4.4}$$

where Δw_i is the difference of rotation w_i (with respect to the axes of the basis) between two neighboring points separated spatially by Δx_j in the j-th direction. Thus, it arises the GND densities obtained by EBSD or HR-EBSD depend on the step size [JIA 13],[FRE 18], which will be further discussed in this study.

Regarding the HR-EBSD technique, relative lattice rotations w_i between the reference and the target are directly obtained, as well as the elastic strains. In the case of standard EBSD, the contribution of elastic strains is unknown and simply omitted while the lattice rotations w_i are derived from the Euler angles [PAN 08]. Given two points "A" and "B" of the material, their respective orientation matrices g_A and g_B are computed and the disorientation angle $\Delta\theta$ is then deduced:

$$\Delta\theta = \min_k \left[\arccos \left(\frac{tr(\Delta g^k) - 1}{2} \right) \right], \tag{4.5}$$

where Δg^k is the "disorientation‘' matrix for the k^{th} symmetry of the crystal. This disorientation is decomposed into three rotations w_i with respect to the axes X_i of the sample frame:

$$w_i = -e_{ijk}.\Delta g_{ij}.\frac{\Delta\theta}{2.\sin(\Delta\theta}, \tag{4.6}$$

Where e_{ijk} is the permutation symbol of Levi-Civita. The lattice rotations are evaluated considering the same reference point as in the HR-EBSD analysis. On the one hand, the location of this reference is not important from a strictly mathematical point of view, the calculation of the Nye tensor implying spatial derivatives. On the other hand, the grain internal disorientation angle is generally smaller between neighboring pixels. As mentioned in the introduction, this is detrimental to the accuracy on the disorientation axis [PRI 99], and the rotations w_i accordingly.

For both EBSD and HR-EBSD, only a partial computation of the Nye's dislocation tensor is possible. Indeed, the latter implies spatial derivatives along the surface normal direction ($\overrightarrow{X_3}$) which are unknown due to the two-dimensional nature of EBSD measurements:

$$\alpha = \begin{bmatrix} \frac{\partial\varepsilon_{12}}{\partial x_3} - \frac{\partial\varepsilon_{13}}{\partial x_2} & \frac{\partial\varepsilon_{13}}{\partial x_1} - \frac{\partial\varepsilon_{11}}{\partial x_3} & \frac{\partial\varepsilon_{11}}{\partial x_2} - \frac{\partial\varepsilon_{12}}{\partial x_1} \\ \frac{\partial\varepsilon_{22}}{\partial x_3} - \frac{\partial\varepsilon_{23}}{\partial x_2} & \frac{\partial\varepsilon_{23}}{\partial x_1} - \frac{\partial\varepsilon_{21}}{\partial x_3} & \frac{\partial\varepsilon_{21}}{\partial x_2} - \frac{\partial\varepsilon_{22}}{\partial x_1} \\ \frac{\partial\varepsilon_{32}}{\partial x_3} - \frac{\partial\varepsilon_{33}}{\partial x_2} & \frac{\partial\varepsilon_{33}}{\partial x_1} - \frac{\partial\varepsilon_{31}}{\partial x_3} & \frac{\partial\varepsilon_{31}}{\partial x_2} - \frac{\partial\varepsilon_{32}}{\partial x_1} \end{bmatrix} + \begin{bmatrix} \frac{\partial w_{12}}{\partial x_3} + \frac{\partial w_{31}}{\partial x_2} & \frac{\partial w_{13}}{\partial x_1} & \frac{\partial w_{21}}{\partial x_1} \\ \frac{\partial w_{32}}{\partial x_2} & \frac{\partial w_{23}}{\partial x_1} + \frac{\partial w_{12}}{\partial x_3} & \frac{\partial w_{21}}{\partial x_2} \\ \frac{\partial w_{32}}{\partial x_3} & \frac{\partial w_{13}}{\partial x_3} & \frac{\partial w_{31}}{\partial x_2} + \frac{\partial w_{23}}{\partial x_1} \end{bmatrix} \tag{4.7}$$

$$w_{ij} = -e_{ijk}w_k, \tag{4.8}$$

As a consequence, only α_{13}, α_{23} and α_{33} components are fully assessable [SUN 00], [ELD 03], [PAN 08]. The α_{12} and α_{21} components are determined by neglecting the contribution of elastic strains, which is partly unknown. Finally, the components α_{31} and α_{32} are not computable, neither the contribution of lattice curvatures nor that of elastic strains being fully assessable.

In this study, both EBSD and HR-EBSD results are discussed from the norm of the estimated Nye's tensor. Its α_{ij} components having units of inverse length, there are divided by the norm b of the Burgers vector to express a GND density in m^{-2}:

$$\rho_{GND} = \frac{1}{b}\sqrt{\alpha_{ij}.\alpha_{ij}} \tag{4.9}$$

Data processing to obtain the HR-EBSD orientation maps was performed by Clément Ernould, Benoît Beausir and Emmanuel Bouzy from the University of Lorraine France.

4.2.2.3 X-Ray Diffraction

XRD experiments were conducted in a BRUKER D8 advance diffractometer equipped with a Mo-K_α radiation ($\lambda_{K\alpha1} = 0.7093$Å), a Zr filter to absorb the K radiation from molybdenum, a 1 mm collimator and a Lynxeye linear detector. The goniometer is operating in a θ/θ configuration: the X-ray tube and the detector present symmetrical movements while the sample remains horizontal in a fixed central location. Estimation of the crystallite size, D, as well as the microstrain, RMS (Root Mean Square), was obtained by XRD line broadening using Popa model integrating in Maud software.

XRD diagrams were fitted with a pseudo-Voigt function in Maud software [LUT 00]. Instrumental parameters for the fit (Caglioti parameters, Lorentzian/gaussian ratio) were determined on a standard NIST powder of hexaboride of lanthanum (LaB_6). The formula proposed by Murugesan *et al.* [MUR 11] for the dislocation density calculation was used.

The dislocation density can be decomposed into two contributions:

$$\rho = (\rho_D \times \rho_S)^{1/2} \tag{4.10}$$

with ρ_D the domain contribution $\rho_D = \frac{3}{D^2}$ and ρ_S the deformation contribution $\rho_S = \frac{k<\varepsilon_L^2>}{b^2} = \frac{k<\varepsilon_L^2>\sqrt{2}}{a^2}$

with k the material constant, D the crystallite size, $<\varepsilon_L^2>$ RMS micro strain and b the burger vector (here $b = \frac{a}{\sqrt{2}}$). All uncertainties were calculated from the formulas given by Murugesan *et al.* [MUR 12].

The XRD part (measurement and data processing) was realized by RaphaëlleGuillou from CEA Paris-Saclay.

4.3 Results

4.3.1 Transmission Electron Microscopy

For each strain rate and for each phase, two to three grains of each phase were orientated in several TB conditions. All g_{hkl} diffracting vectors used for the analysis are listed in Table 4.1. The acquisition of dislocation images on the 10% deformed sample was difficult due to the strong disorientation present in the grains (about 5 to 6° for the most disoriented areas), and fewer diffraction conditions were observed for that sample. To limit the underestimation, the dislocation density for each grain was chosen as the maximum one measured on the different orientation conditions.

	Austenite			Ferrite		
	Sample 1	Sample 2	Sample 3	Sample 1	Sample 2	Sample 3
	0%	5%	10%	0%	5%	10%
Diffracting vectors	$(1\bar{1}1)$ $(\bar{2}20)$ (311)	$(1\bar{1}1)$ (110)	$(1\bar{1}1)$	(101) (110) $(1\bar{1}2)$	$(01\bar{1})$ (100) $(\bar{2}1\bar{1})$	(110) $(2\bar{1}1)$
Diffracting vectors	$(1\bar{1}1)$	(110) $(11\bar{1})$	(110)	$(\bar{1}10)$ $(0\bar{2}0)$	(110)	(110)
Diffracting vectors	(202) $(1\bar{1}\bar{1})$	$(1\bar{1}1)$ $(\bar{1}10)$ (311)	$(11\bar{1})$	$(01\bar{1})$		

Table 4.1: Summary of diffraction vectors used to characterize the three austenite grains and three ferrite grains, for different strain rates.

The analyzed area slightly varies for the different samples. For 5% and 10% deformed grains, the average image area is respectively 0.5 μm^2 and 0.3 μm^2, while it is 3.5 μm^2 for the undeformed sample. Indeed, for high deformation levels, disorientation within each grain increases. Therefore, contrasts conditions vary rapidly and the observable areas on each image are reduced. Moreover, with increasing dislocation densities, dislocations overlapping increases. It was then necessary to enhance the magnification in order to have sufficient resolution to distinguish them from each other.

Figure 4.1 shows typical TB TEM micrographs obtained in austenite and in ferrite for undeformed and deformed samples at 5 and 10%. The dislocations appear in black on a white background. In the undeformed state, only few dislocations are seen in the austenite in Figure 4.1(a). The density seems higher in ferrite (Figure 4.1(b)) where dislocations appear as points or lines which reveals that their orientation in the grain is random. After 5% deformation, the number of visible dislocations has greatly increased. In Figure 4.1(d), the dislocations in the 5% deformed ferrite have clustered and become more tortuous. The overlapping of dislocations is important, as in the deformed austenite (Figure 4.1(c)). In the case of the 10% deformed sample (Figure 4.1(e) and (f)), it is quite difficult to image dislocations over large surfaces, because the important disorientation locally modifies the contrast conditions. However, there is not much difference in the resulting micrographs, compared to the 5% deformed sample. It is necessary to remind that the local thickness of the diverse thin foil is quite different. For example, for the deformed ferrite at 5% it was measured to be 220 ± 37 nm , while it is 146 ± 37 nm for the 10% deformed sample (Figure 4.1 (d) and (f)). This can be misleading for a direct eye comparison of the images.

Dislocation densities were determined using the intercept method. The maximum values for each deformation level and phase are presented in table 4.2.

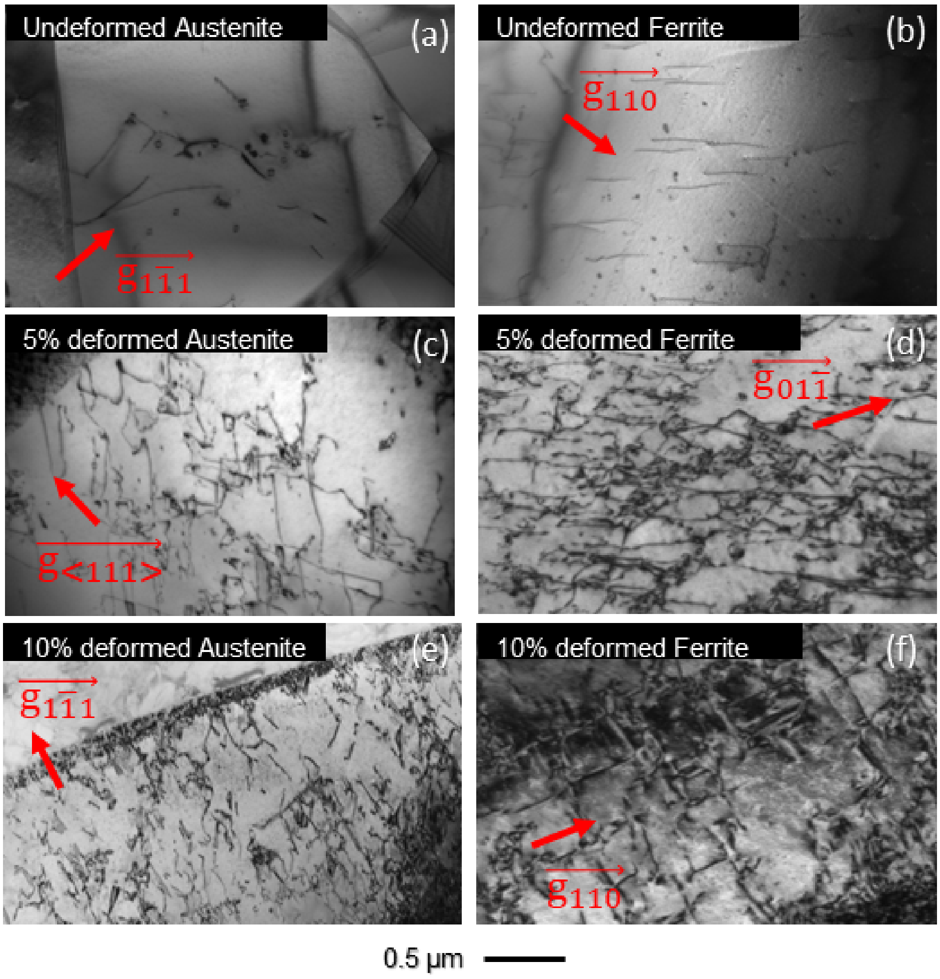

Figure 4.1: TEM image acquired on different grains. For each image, the dislocation lines are visible in black on a white background. (a) Undeformed austenite grain. (b) Austenite grain in sample deformed at 5%. (c) Austenite grain in sample deformed at 10%. (d) Undeformed ferrite grain. (e) Ferrite grain in sample deformed at 5%. (f) Ferrite grain in sample deformed at 10%.

	0%	5%	10%
Austenite	$(1.1 \pm 0.1) \times 10^{13}$	$(6.7 \pm 1.0) \times 10^{13}$	$(1.4 \pm 0.3) \times 10^{14}$
Ferrite	$(1.2 \pm 0.1) \times 10^{13}$	$(5.7 \pm 0.8) \times 10^{13}$	$(1.2 \pm 0.2) \times 10^{14}$

Table 4.2: Mean value of the dislocation density m^{-2} obtained on ferrite and austenite grains for different strain rates with intercept method

The dislocation density is measured to be similar in both phases. As expected, the dislocation density increases with deformation, with a slightly quicker increase in austenite compared to ferrite, as austenite deforms before ferrite [ZHA 21]. After 10% deformation, dislocation densities measured in ferrite and in austenite are about 10 times higher than before deformation. However, in the 10% deformed sample, it is very hard to observe the dislocations on a large surface on a single image because of the deformation but also because of the thin foil which is slightly twisted. This adds to the difficulty of observing the dislocations but also to the measurement, especially on the top of the image of the 10% deformed ferrite (Figure 4.1(f)). This is why the measurement uncertainty increases for the latter values as it becomes problematic to distinguish dislocations from each other, due to the overlapping of dislocations and the rapidly changing observation conditions, but also due to the uncertainty of the volume which may lack accuracy.

4.3.2 R-ECCI and Clustering

The ECCI allows the observation of dislocations in white on a black background. In the received state, Figure 4.2(a and b), the dislocations appear as straight lines or as dots, indicating it is rather parallel or perpendicular to the surface. Moreover, at first sight, there would be more dislocations in the ferrite on the ECCI images (Figure 4.2(b)) than in the TEM images (Figure 4.1(b)) which could be due to the thinner thickness observed on the TEM images. In austenite, after deformation, the dislocations appear as straight lines and are mainly aligned along 111 planes, Figure 4.2(c) and (e). The high concentration of dislocations in the 10% deformed austenite (Figure 4.2(e), blue arrow) results in a large variation in contrast, especially at the grain boundaries, making it difficult to detect dislocations using the clustering algorithm. In the case of ferrite Figure 4.2(b, d and f), the dislocations are more tortuous and seem to have random directions including in the deformed cases Figure 4.2(d and f). Moreover, the contrast variations are already visible after 5% in the deformed ferrite Figure 4.2(d) and become even more significant after 10% deformation (red arrow).

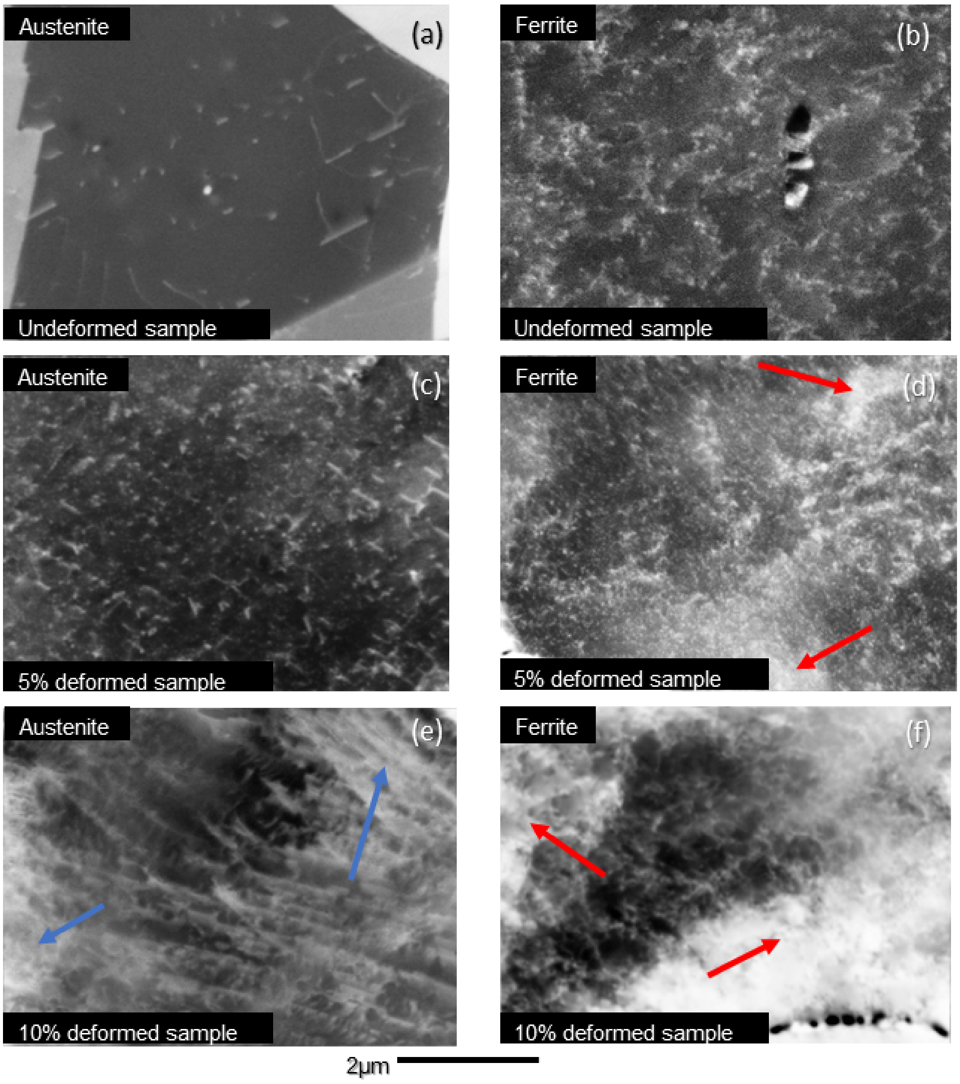

Figure 4.2: BSE image acquired with an accelerating voltage of 20 kv, aperture of 120 μm and pixel size of 4.5 nm. (a), (c) and (e) show respectively three austenite grains present in an undeformed, 5% deformed and a last 10% deformed sample. Similarly, images (b), (d) and (f) show respectively three ferrite grains present in an undeformed, 5% deformed and a last 10% deformed sample.

After analysis, detected dislocations are represented as green pixels on a dark matrix, Figure 4.3(b), (d) and (f) for the undeformed, 5%, and 10% deformed sample respectively. The dislocation density calculated by the clustering algorithm is $(1.5 \pm 0.1) \times 10^{13}$ m^{-2} for undeformed austenite (Figure 4.3(a) and (b)) for which almost all dislocations were detected. This first case illustrates the effectiveness of the algorithm when the dislocations are well distinct and show a good contrast with the grain. In the case of ferrite after 5% deformation, the BSE image in Figure 4.3(c) shows more clustered dislocations that are harder to distinguish (blue circle). In that area, some dislocations are not indexed by the algorithm, Figure 4.3(d), and a local underestimation of the density is expected. Moreover, in some other area, the large amount of dislocation creates local disorientation that affects the contrast (yellow arrows). After analysis, those areas appear as large cluster (yellow arrows) much thicker than what they should be compared to the apparent width of the dislocations (Figure 4.3(c)). This probably leads to a local over's estimation of the density. As a result, for this ferrite grain, the density was measured to be $(5.6 \pm 1.0) \times 10^{13}$ m^{-2}.

Finally, an austenitic grain subjected to 10% strain is displayed in Figure 4.3(e). This grain is highly disoriented, resulting in significant contrast variations in the grain (red arrows). Although the dislocations present in austenite are easier to image in ECCI than in ferrite, austenite deforms before ferrite, so that dislocation densities quickly reach values that are no longer measurable by clustering. Indeed, the dislocations form cells and become difficult to distinguish from each other. As with the previous ferritic grain, the clustering algorithm finds areas where all dislocations are merged (yellow arrows on Figure 4.3(f)), which gives an overestimation of the density. These "large clusters‘' are partly due to the strong contrast variation but also to the proximity or overlapping of the dislocations. Moreover, for some areas there is an information loss (blue circles). For this sample, the clustering is more efficient in the center of the image than on the edges because of the more important disorientation at the grain boundaries. For all those reasons, the obtained value of $(7.4 \pm 1.5) \times 10^{13}$ m^{-2} seems underestimated. In that case, and for comparison's sake, single ECCI images were used and dislocations density were measured manually. The measured density for the 10% deformed austenite is $(1.3 \pm 0.4) \times 10^{14}$ m^{-2}, which confirms that it is well beyond the current limits of the method.

	0%	5%	10%
Austenite	$(1.5 \pm 0.1) \times 10^{13}$	$(4.5 \pm 1.0) \times 10^{13}$	$(7.4 \pm 1.5) \times 10^{13}$
Ferrite	$(2.5 \pm 0.1) \times 10^{13}$	$(5.6 \pm 1.0) \times 10^{13}$	$(5.4 \pm 1.0) \times 10^{13}$

Table 4.3: Mean value of the dislocation density m^{-2} obtained on ferrite and austenite grains for different strain rates measured from ECCI imaging.

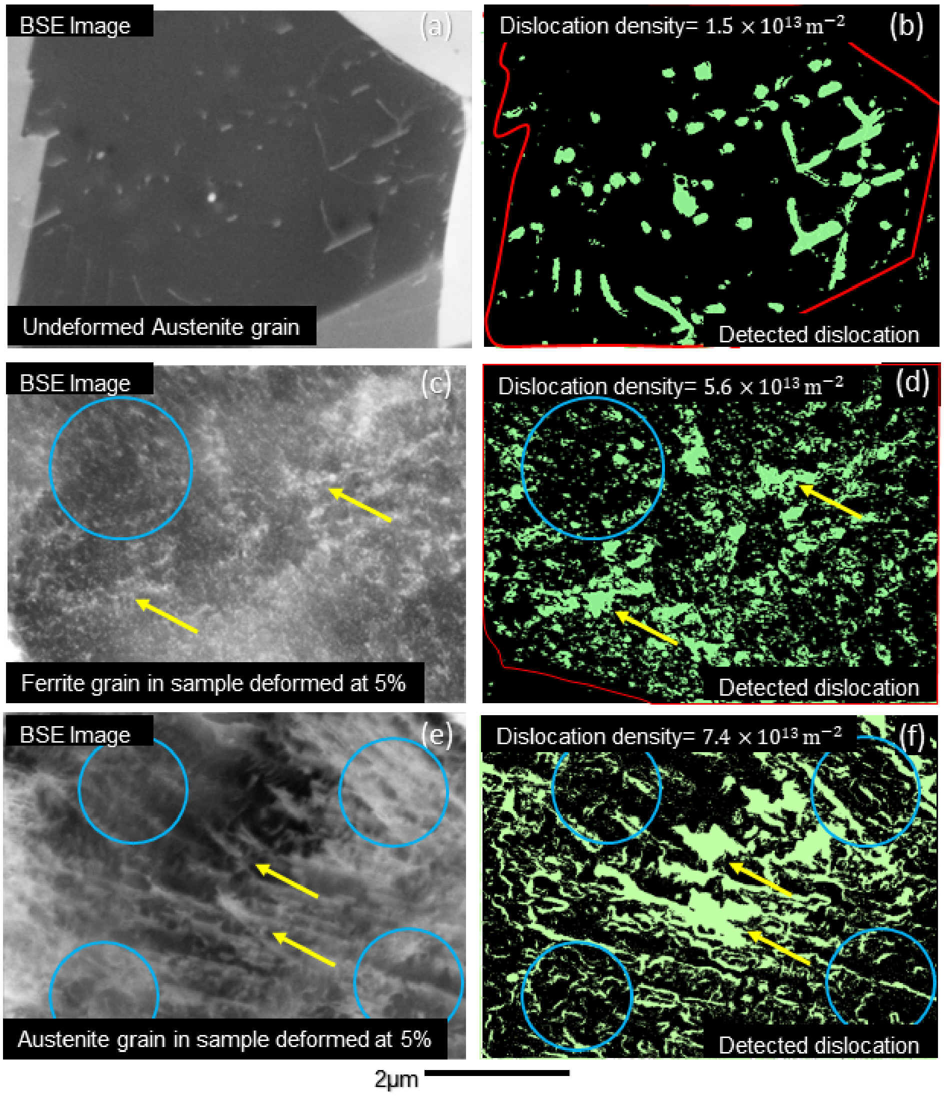

Figure 4.3: BSE images acquired with an acceleration voltage of 20 kv, an aperture of 120 μm and a pixel size of 4.5 nm. (a), (c) and (e) show respectively an undeformed austenite grain (a), a ferrite grain present in a sample deformed at 5% (c) and an austenite grain present in a sample deformed at 10% (e) The images (b), (d) and (f) show the results obtained by the clustering algorithm where the detected dislocations appear in green and the densities thus measured on the grains (a), (c) and (e) respectively. Only the pixels in the red box (b) and (d) were considered for the calculation of the dislocation densities. The blue circles show the areas where information was lost and all dislocations are not or partially detected. The yellow arrows show the areas where dislocations are detected but much thicker than in the BSE images.

4.3.3 Electron Back Scattered Diffraction

Several EBSD acquisitions were carried out for each strain rate. The areas chosen usually covered both phases and contain interfaces or grain boundaries, where deformation is known to localize for this type of alloys. Note that the investigated areas are rather small (5×5 μm maximum).

Acquisition time was indeed limited to around 23 min per map, since the high sensitivity of the HR-EBSD technique can make image drift becoming visible for longer acquisitions.

In a first time, orientation mappings are post-processed in a standard way by assessing the norm of the Nye tensor from Euler angles. The so-obtained GND density maps are shown in Figure 4.4, bottom row, and they will be further discussed in the light of HR-EBSD measurements.

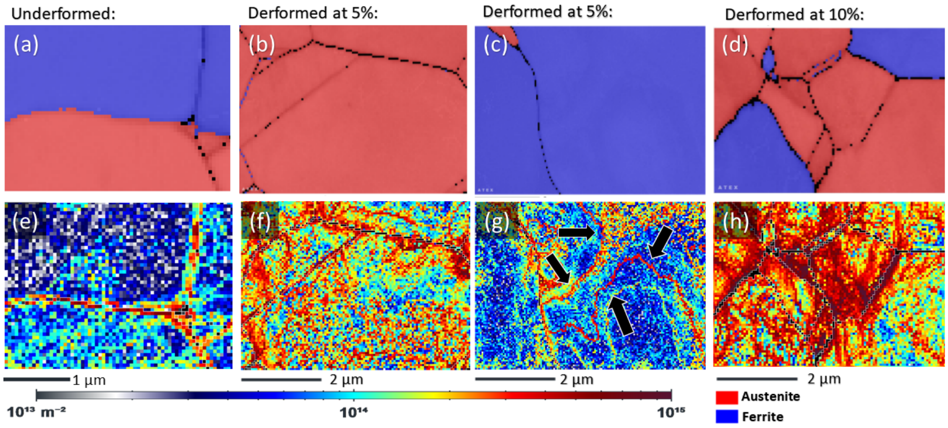

Figure 4.4: Example of EBSD phase maps (top line, with austenite in red and ferrite in blue) obtained on undeformed, 5 and 10% deformed steel samples. Norm of Nye tensor map obtained by EBSD (bottom line).

To obtain a dislocation density value which can be compared with the other used methods, average values were calculated, for each present grain, and given in Table 4.4. With increasing strain, the density in austenite (red in Figure 4.4, top row) evolves faster than that contained in ferrite (blue), which is consistent with the fact that austenite deforms before ferrite [ZHA 21].

	0%	5%	10%
Austenite	$(1.2 \pm 0.7) \times 10^{14}$	$(2.1 \pm 0.8) \times 10^{14}$	$(3.3 \pm 1.2) \times 10^{14}$
Ferrite	$(4.6 \pm 1.4) \times 10^{13}$	$(1.1 \pm 0.5) \times 10^{14}$	$(2.1 \pm 0.9) \times 10^{14}$

Table 4.4: Average value of the dislocation density m^{-2} obtained with the norm of Nye tensor, on ferrite and austenite grains for different strain rates.

4.3.4 High Resolution-Electron Back Scattered Diffraction

An HR-EBSD analysis is now conducted on each one of the previous EBSD data sets. The strain concentration at the grain boundaries for both phases is now more clearly observed from the GND mappings in Figure 4.5.

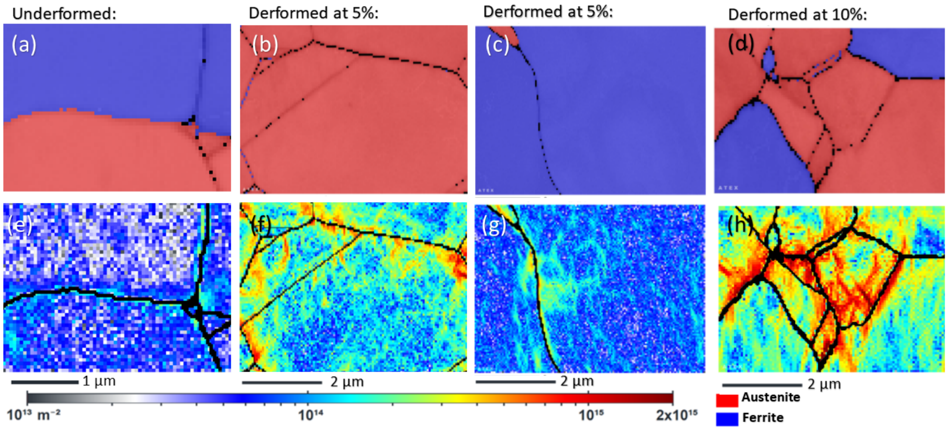

Figure 4.5: Example of EBSD map (top line) obtained on undeformed, 5 and 10% deformed steel samples. GND-map obtained by HR-EBSD (bottom line).

Same as for EBSD, the dislocation density is averaged at the grain scale and values are summarized in Table 4.5. Overall, both the EBSD and the HR-EBSD techniques are quite in agreement, but the average GND density obtained by EBSD is always higher than with HR-EBSD. This is attributed to the noisier character of the maps derived in Euler angles (Figure 4.4), while the measurement uncertainty is estimated at 1.1×10^{13} m^{-2} with HR-EBSD (minimum of GND obtained).

This is particularly visible in Figure 4.4(g), where the continuous red lines (spotted with back arrows) do not correspond to any obvious dislocation structure, that the sensitivity of the HR-EBSD technique on orientation changes would have detected in Figure 4.5(g). This is also confirmed by the absence of such marked features in the virtual backscatter electron diode image in Figure 4.6(a) either, although its contrast is very sensitive to orientation changes as well (see [ERN 20b] for more details). Note that it only provides qualitative information whereas the HR-EBSD technique is quantitative.

The aforementioned red lines in Figure 4.4(g) come from a discretization of orientations by the indexing software. Indeed, they superimpose with the relative rotation w_2 within grain derived from Euler angles in Figure 4.6(b), which locally presents discontinuities of the order of 0.2°, in agreement with the angular resolution of the indexing techniques. Note that the considered axis is here parallel to the image height, but its choice is not relevant for the purpose. Point is to underline that knowledge of the disorientation axis is essential for the accurate assessment of GND densities (since a tensor is to be computed). That is why those artifacts are less visible from the disorientation angle in practice (not shown here), since the latter does not carry information about the axis.

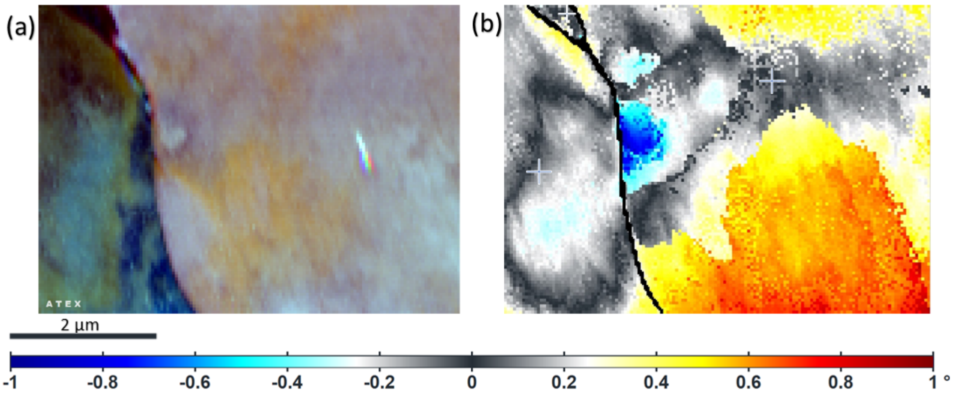

Figure 4.6: (a) Virtual forescatter electron diode image computed form the Kikuchi patterns stored for the HR-EBSD analysis. (b) Relative rotation around the second axis of the sample frame. These rotations are computed from Euler angles, relatively to a reference point within each grain (spotted by a white cross).

Note that the largest discrepancy between EBSD and HR-EBSD is observed at 0% strain in austenite, where the value obtained by EBSD is twice higher than the one obtained by HR-EBSD. Although such a gap is not observed in ferrite, it is not surprising it concerns the sample with the lowest grain internal disorientations. As already mentioned, uncertainty on the disorientation axis derived from Euler angles is maximal.

	0%	5%	10%
Austenite	$(5.6 \pm 1.1) \times 10^{13}$	$(1.7 \pm 0.2) \times 10^{14}$	$(2.6 \pm 0.2) \times 10^{14}$
Ferrite	$(4.2 \pm 1.1) \times 10^{13}$	$(8.6 \pm 1.5) \times 10^{13}$	$(1.9 \pm 0.2) \times 10^{14}$

Table 4.5: Average value of the dislocation density m^{-2} obtained using of HR-EBSD on ferrite and austenite grains for different strain rates.

Overall, the average GND density obtained by HR-EBSD follows the same trends than with EBSD. Between the undeformed sample and the 5% deformed sample, the dislocation density in Ferrite increases by a factor of 2 whereas in austenite the evolution is 3 times faster. This slower increase in ferrite for the first stages of the deformation is consistent with the fact that Austenite is deforming first. However, between the 5% deformed stage and the 10% deformed stage, the austenite keeps increasing but at a slower rate than in the previous stage (from a factor of 3 to 1.5) while dislocation density in ferrite has a slightly higher factor and increases from 2 to 2.2

4.3.5 X-Ray Diffraction

XRD diffractogram obtained for 0%, 5% and 10% deformed samples are presented on Figure 4.7.

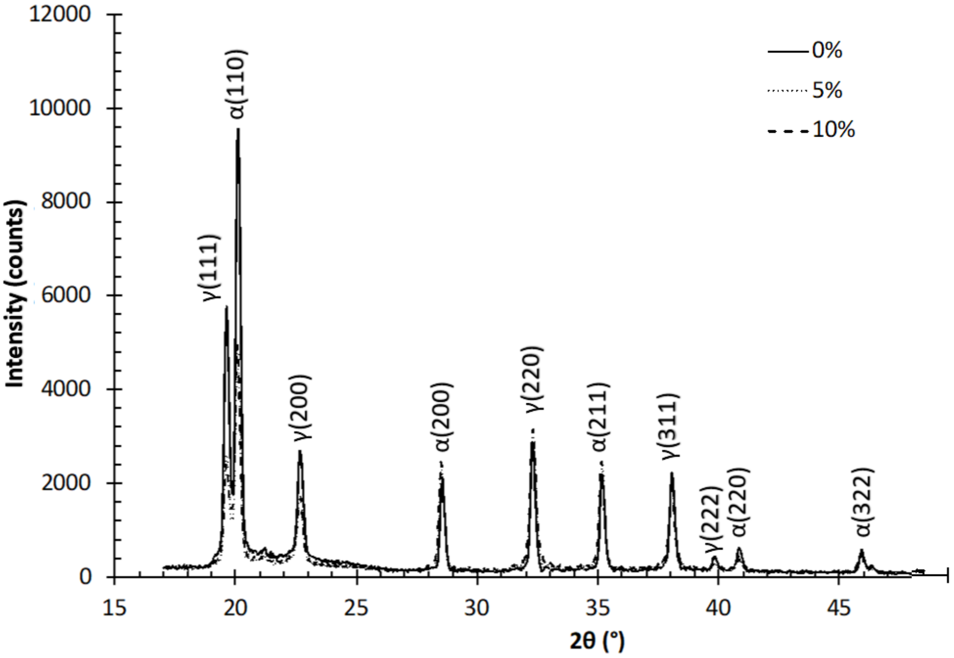

Figure 4.7: Experimental XRD diffractograms for 0%, 5% and 10% deformed samples.

Density dislocation obtained on ferrite and austenite grains for different strain rates are summarized on the table 4.6.

	0%	5%	10%
Austenite	$(4.0 \pm 10.7) \times 10^{13}$	$(1.7 \pm 0.3) \times 10^{14}$	$(1.8 \pm 0.3) \times 10^{14}$
Ferrite	$(6.1 \pm 13.1) \times 10^{13}$	$(7.6 \pm 4.6) \times 10^{13}$	$(9.0 \pm 2.6) \times 10^{13}$

Table 4.6: Average value of the dislocation density m^{-2} obtained thanks to XRD on ferrite and austenite grains for different strain rates.

The measurement uncertainties on the undeformed sample are on the order of 200%. This is because the RMS microstrain $< \varepsilon_L^2 >$ is included in the curve fitting parameters and is difficult to obtain accurately on the undeformed sample. In the deformed sample, RMS microstrain $< \varepsilon_L^2 >$ is higher and can be more precisely determined. Thus, its uncertainty drops by a factor of 10, and the global measurement uncertainty is then three to four times smaller.

During deformation, the dislocation density present in the austenite measured by XRD increases faster than the density present in the ferrite, which is consistent with the deformation mechanism of a duplex steel [ZHA 21]. For instance, the density in austenite is measured to be twice higher than in ferrite after 5% and 10% of deformation. After 10% of deformation, the density does not evolve much compared to 5% deformation, for both phases. For austenite phase, it was observed that the austenite grains were partly transformed into martensite. Thus, the crystallite size D was overestimated in this sample and therefore the dislocation density present in the 10% deformed sample may be underestimated.

4.4 Discussion

All methods presented here do not measure the same type of dislocation (ρ_c , ρ_w , ρ_{GB}). Moreover, each method has its own limitations and uncertainties so it is important to compare them carefully.

Each used measurement method relies on different computational means, based on diffraction, disorientation, channeling contrast or manual dislocation counting. Figure 4.8(a) shows a schematic representation of the dislocation configuration that can be observed within one grain (group of random dislocations ρ_c, dislocation cell ρ_w, dislocations grouped at the grain boundary $\rho_G B$).

XRD measurements allow to measure disorientations, within what is defined as crystallites, Figure 4.8(b). This means that the dislocations close to the grain boundaries (ρ_{GB}) or grouped in cells (ρ_w) which are the main source of GND will not be considered when calculating the dislocation density. Moreover, a crystallite is defined as an area showing a low disorientation, it can be a grain, but also a dislocation cell. Therefore, dislocation cells will be observed as grain with this method. The size of crystallite is often very complicated to obtain [UNG 01] because it can vary enormously from case to case and it becomes difficult to calculate it precisely if the shape of the crystallite [LOU 83] or if the deformation [CAG 58] becomes anisotropic.

In the case of TEM and ECCI imaging methods, dislocations are theoretically all visible but it is often very difficult to distinguish dislocations near grain boundaries as the disorientation is important and the conditions for observing dislocations change rapidly, Figure 4.8(c). Moreover, imaging methods give images projected on a surface and overlapping dislocations, such as at the ones present at grain boundary or at cell walls, cause a non-negligible uncertainty [GAL 22]. This is why the densities measured by imaging can be considered to be mainly dislocations isolated from the dislocation clusters (ρ_c).

In the case of the EBSD or HR-EBSD methods presented Figure 4.8(d), the relative rotation and elastic strain fields are measured from which a GND dislocation density is derived. The most influential parameter on the results is the pixel size used. As shown by Jiang et al. [JIA 13] the dislocation density can vary by an order of magnitude when the pixel size is doubled. Indeed, if the maps are acquired with a very fine step, as on the Figure 4.8(d) (left) then the dislocations will be discernible and will be defined as GND's. However, if a larger step is used (as in the Figure 4.8(d) right), some dislocation clusters could have their Burgers vector opposed and no longer cause lattice rotation. These dislocations will then be considered as SSDs. As specified by Jiang et al. [JIA 13], these variation in measured density are the consequence of a change in the threshold defined between SSDs and GNDs.

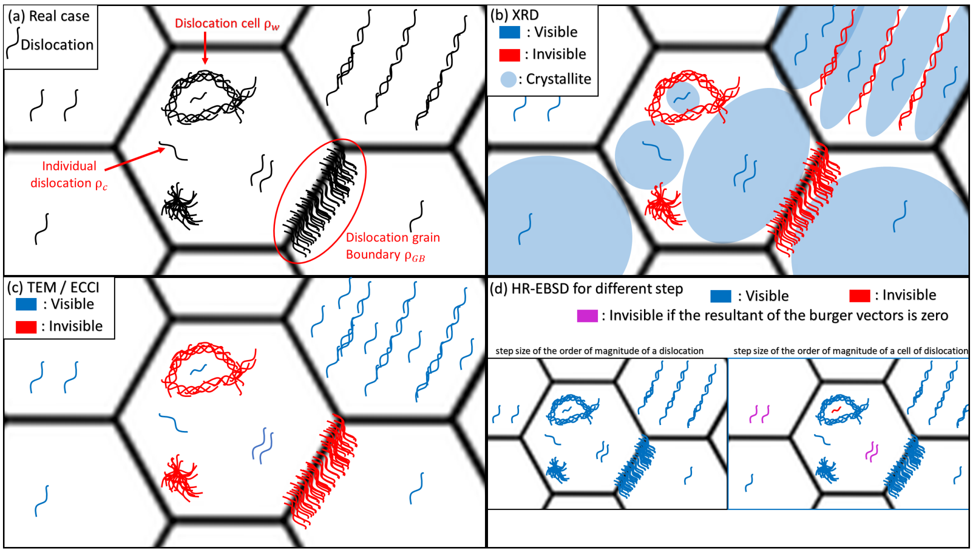

Figure 4.8: Grain pattern with several cases of dislocations observable: dislocation cluster, isolated dislocation, dislocation cell, dislocation cluster present in particular planes. (a) Real case, (b) Illustration of dislocations analyzed by XRD and the crystallite size used. (c) Illustration of dislocations analyzed by TEM/ECCI imaging methods. (d) Two cases illustrating what the HR-EBSD method can distinguish according to the pixel size used (very fine pixel size on the left and a larger pixel size on the right).

The quantitative comparison of all measurements results is presented on Figure 4.9. The values obtained for the 0% sample remain in the same order of magnitude regardless of the method, although XRD measurement uncertainty is very high (271%, calculated with the method of Murugesan *et al.* [MUR 12]).

After 5% of deformation, a higher dislocation density is expected in austenite compared to ferrite. XRD and HR-EBSD results are close to each other and both indicate dislocation density twice higher in austenite than in ferrite for this state (around 1.7×10^{14} m^{-2} and 0.7×10^{14} m^{-2} respectively). However, imaging-based measurements such as ECCI and TEM indicate smaller densities with around 5×10^{13} m^{-2}, for both phases. In austenite, where the dislocation density evolves faster during the deformation, the imaging methods ECCI and TEM give underestimated measurements due to the overlapping of dislocations.

For the 10% deformed sample, ECCI measurement were not possible as the density is over the acceptable measurement range. All other three methods reveal a large increase in dislocation density. HR-EBSD gives the highest dislocation density with $(2.6 \pm 0.2) \times 10^{14}$ m^{-2} for austenite and $(1.9 \pm 0.2) \times 10^{14}$ m^{-2} for ferrite. However, the results from TEM imaging indicate a similar density for both phases with $(1.2 \pm 0.2) \times 10^{14}$ m^{-2} for ferrite and $(1.4 \pm 0.3) \times 10^{14}$ m^{-2} for austenite. Finally, XRD measurements, are different for both phases with $(9.0 \pm 2.6) \times 10^{13}$ m^{-2} for ferrite and $(1.8 \pm 0.3) \times 10^{14}$ m^{-2} for austenite. Those values are very close to that measured in the 5% deformed sample, which is quite surprising as the dislocation is expected to increase between those two states.

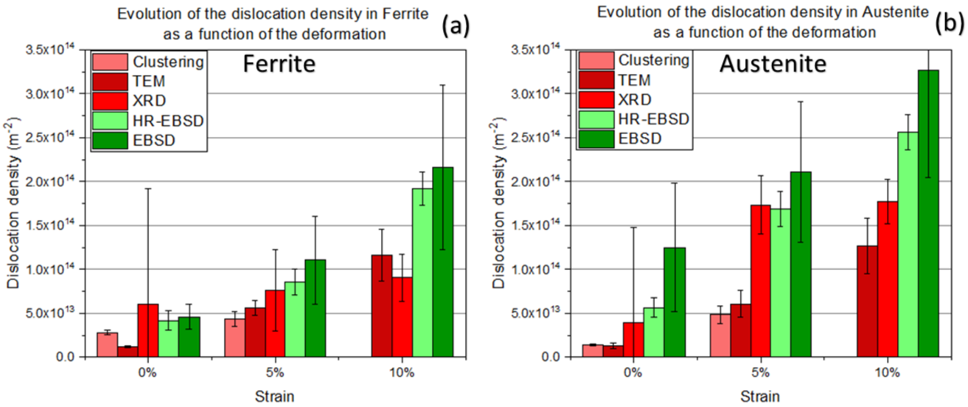

Figure 4.9: Comparison of dislocations densities measured with XRD, TEM, HR-EBSD, and R-ECCI for (a) austenite and (b) ferrite, in the undeformed, 5% and 10% deformed samples.

We should note that TEM, ECCI-based and EBSD/HR-EBSD are all local measurement techniques, that will provide data on a limited number of grains. In a polycrystalline material, the deformation process of individuals grains is dependent on their relative orientation to the loading geometry and on their relative neighborhood.

4.4.1 SSD measurement (TEM; ECCI and XRD)

Both ECCI and TEM observations provide a majority determination of the SSD dislocation density. Indeed, imaging methods lose a lot of information due to dislocation overlapping [GAL 22], as is observed at grain boundaries and in dislocation cells. In practice, these methods are applied at the center of the grain (relatively far from ρ_{GB}) and cannot accurately measure the number of dislocations in cells or walls (ρ_w). Even if it is difficult to know how far the dislocations generated at the grain boundaries by the deformation will disperse inside the grain [ALL 15] we consider that all observations were performed inside the grains, and do not take into account the dislocations at grain boundaries. Moreover, both methods are very local. For all those reasons one can expect similar measurements from both techniques, which is the case, considering the uncertainty of both measurements. However, we observed that for higher dislocation densities, and specifically for the 10% deformed sample, the disorientation within the grains, and the dislocation overlapping, made ECCI measurement irrelevant while some values could still be obtained from TEM measurements. We guess that this was due to the fact that for those high-density values, it could be possible with TEM to perform images close to the thin foil hole, i.e. in very thin areas, while the measurements depth is fixed for SEM-ECCI measurements to the accelerating voltage chosen. For ECCI measurements, the main uncertainty arises from the probed depth determination. The probed depth was assumed to be equal to $5\xi_g$ [ZAE 14] but some author also provide values of $5\xi_g$ [WIL 93]. In the present case, the choice of $5\xi_g$ seem to better reproduce TEM observations.

XRD measurements indicate an almost similar dislocation density for austenite and ferrite deformed at 5 and 10%, which is not representative of the microstructure expected. Sidor *et al.* [SID 21] also observed this saturation in XRD measurements in a cold rolled aluminum alloy. The densities obtained between two rolling steps remain equal to $(1.2 \pm 0.2) \times 10^{14}$ m^{-2}. This effect can be partly explained by the dynamic equilibrium between dislocation multiplication and annihilation, giving a saturation of the dislocation density. Moreover, in the case studied here, the formation of martensite has not been taken into account. 316L steels are mainly composed of austenite which, during deformation, transforms into martensite, thus decreasing the size of the crystallites, as shown by Han *et al.* [HAN 21][64] or Gubicza *et al.* [GUB 16]. The formation of this third phase in the steel studied here will therefore reduce the crystallite size D of the observed phases, which will increase the value of the density ρ_D (in equation (4.10) for the 10% deformed sample.

However, XRD measurements are global measurements and should allow for the determination of SSDs densities, such as TEM and ECCI. Indeed, Lee *et al.* [LEE 14] reproduced a torsionally deformed copper sample with a Finite Element Method (FEM). They were able to compare their simulated value with the experimental TEM and XRD measurement. This allowed them to conclude that the dislocation density measured by XRD was located inside the cells, *i.e.* ρ_c. Even if the uncertainty in the measurement without deformation is very large for XRD measurements, the determined values are in the same range as the ones obtained by TEM/ECCI. The increase observed for 5% and 10% in the ferrite is in fairly well agreement with the results obtained with the imaging techniques. However, for austenite, there is a much larger discrepancy between XRD and the imaging techniques. However, one can see that the obtained measures are always slightly larger than the one obtained from ECCI/TEM. A first reason for that could be that TEM and ECCI measurements are subjected to surface effects. Surface dislocation are always subjected to the image force, that tends to attract them to the surface. There is a relaxation of the dislocation structure near the free surfaces of the sample, which extends about approximately 65 nm into the sample as demonstrated by Field *et al.* [FIE 10]. In the case of TEM, measurements are performed on a thin film with a small thickness (about 146 ± 10 nm), therefore, the image force cannot be neglected, and the dislocation density is underestimated. Kohnert *et al.* [KOH 20] determined that the structure of a bcc steel loses 40% of the dislocations it contains, once in the state of a thin blade.

4.4.2 GND measurement (HR EBSD and EBSD)

The HR-EBSD method enables to visualize the expected localization of the deformation at grain boundaries for this microstructure, Figure 4.5. This phenomenon, which is explained by the incompatibility of the deformation between the two phases, is often observed in Duplex steels, [KHA 20] but also in Dual Phase steels [MAT 20].

Taking the average GND density on these maps seems to be biased since the disorientation is mainly located at the grain boundaries and there are very few grains present in totality on the maps. Moreover, as the results obtained by the two methods seem to converge for large deformations, the significant data storage (about 15 GB per map) and post-processing required by the HR-EBSD technique is no longer justified, and standard EBSD can be preferred. Which is because the uncertainty of indexing on the disorientation axis becomes less critical as the angular disorientation is increasing. That is why HR-EBSD measurements should be preferred at small deformation, where the contribution of elastic strains are not negligible and for which the lower sensitivity of an indexing-based approach is preventing fine dislocation structures from being observed and quantified. In severely deformed materials, the degradation of the diffraction contrast in Kikuchi patterns strongly degrades the accuracy of HR-EBSD measurements. The slower acquisition speed and significant data storage associated with this technique is therefore no more justified. In between, a synergy of EBSD and HR-EBSD is expected. The first one provides statistics while the second one can be applied to further investigate local details of the microstructure.

Finally, one must be cautions in the interpretation of GND mappings, especially when derived from Euler angles (EBSD). As pointed out in Figure 4.4 and Figure 4.6, GND mappings are sensible to orientation noise and may present alleged dislocation walls, whereas they are artifacts. The latter typically result from a discretization of orientations, which occurs when using dictionary indexing techniques [CHE 15] or applying spatial filters (Kuhawara). Smoothing orientations to reduce noise in GND mappings is also not advisable, GND accounting for discontinuities in the crystal orientations. Regarding HR-EBSD analyses, possible artifacts rather stem from drift during acquisition. Because of the higher sensitivity of the method, drift may become visible in form of horizontal bands. The falsely associated GND density is however closer to the noise floor than what is seen in Figure 4.4(f) with EBSD.

4.4.3 Discussion about the relative amount of GND and SSD

Although dislocation imaging by TEM or ECCI allows us to see both GND and SSD dislocations, it allows mainly the measurement of ρ_c, *i.e.* mainly SSD. An average is performed from the XRD, TEM and ECCI measurements to obtain a value of ρ_{SSD} which is compared to the measurement obtained by HR-EBSD, ρ_{GND}. In Figure 4.10, the ρ_{GND} and ρ_{SSD} density is almost identical in the undeformed sample. During deformation, GND densities increase faster than SSD, especially for the 10% deformed sample. This is consistent with the fact that the early stages of deformation are driven by austenite, as described by Zhang *et al.* [ZHA 21]. However, the values obtained in this study seem to contradict what is expected in the literature. Zheng *et al.* [ZHE 15] found from a high-energy XRD and TEM experiment in a pearlitic ferritic steel that the density of GND is 10 times greater than that of SSD during deformation. In the 10% deformed sample, the density of GND is only twice that of SSD. Furthermore, the factor of 2 measured on the 10% sample seems to be inconsistent with what was found with mechanical models by Zhi *et al.* namely about twice as many SSD as GND during deformation in a TWIP steel [ZHI 20].

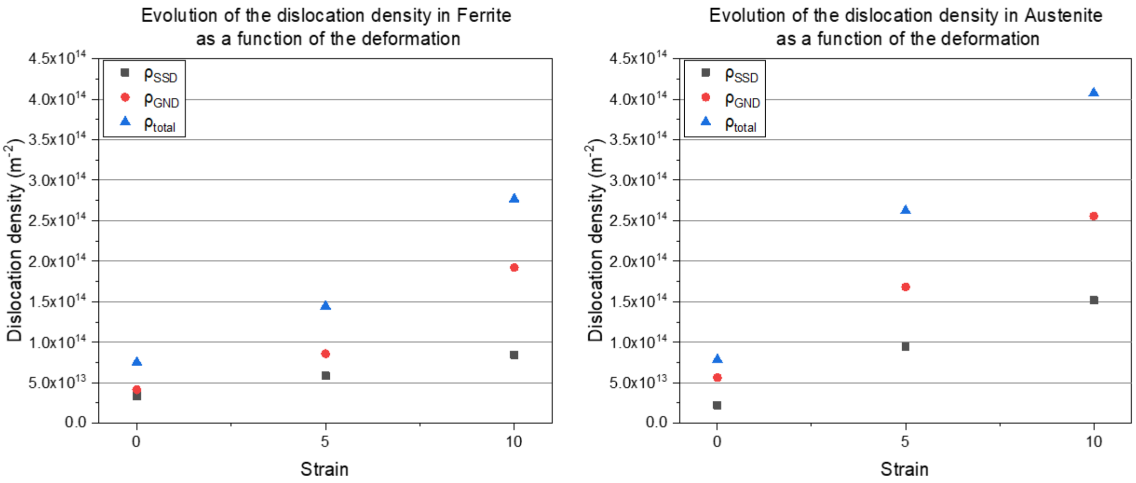

Figure 4.10: Comparison of measured dislocation densities as a function of strain. With ρ_{SSD}, the average of measurements obtained with XRD,TEM and SEM imaging, ρ_{GND} the measurement obtained with HR-EBSD and ρ_{total} the addition of ρ_{SSD} and ρ_{GND}. For (a) austenite and (b) ferrite, in the undeformed, 5% and 10% deformed samples.

4.4.4 Towards the prediction of yield stress

In the field of metallurgy, mechanical models are commonly used to predict the characteristics of a material. The dislocation density used in these models is often characterized by a single method. However, each method can only see a portion of the dislocations contained in the material. Even if the density most often used is the density initially present in the material, the acquisition parameters or the choice of the area can vary the result obtained and thus distort the model. For example, in a model describing the mechanical behavior of ferrite, the contribution to the yield stress σ_y is described by the term σ_R (which is the forest dislocation hardening or isotropic hardening) and is formulated by:

$$\sigma_R = \alpha_T M_T \mu b_{111} \sqrt{\rho_0}, \tag{4.11}$$

where α_T is the forest hardening coefficient, M_T is the Taylor factor, μ is the elastic shear modulus, b_{111} is the burger vector (other possible directions of the burger vector are neglected). The model and the values of the constants used were taken from the study by Mathevon *et al.* [MAT 20]. When using the different values of the dislocation density obtained by the different methods, the values of σ_R differ by 76 MPa between $\rho_{Clustering}$ and ρ_{total} (see table 4.7).

	ρ_0 (m^{-2})	σ_R (Mpa)
$\rho_{Clustering}$	$(2.5 \pm 0.1) \times 10^{13}$	108 ± 3
ρ_{TEM}	$(1.2 \pm 0.1) \times 10^{13}$	70 ± 3
ρ_{XRD}	$(6.1 \pm 13.1) \times 10^{13}$	159 ± 124
$\rho_{HR-EBSD}$	$(4.2 \pm 1.1) \times 10^{13}$	132 ± 19
ρ_{EBSD}	$(4.6 \pm 1.4) \times 10^{13}$	138 ± 23
$\rho_{SSD+GND}$	7.5×10^{13}	177

Table 4.7: isotropic hardening obtained from the values of the different types of initial densities measured in the ferrite.

The contribution due to SSD dislocations (TEM, ECCI-clustering and XRD), lead to an error of a factor two depending on the choice of the characterization technique. However, for the determination of the contribution of GNDs to the YS, it is relatively equivalent to use results obtained from HR-EBSD or EBSD measurements. Finally, the variation of the total value of σ_R considering both GND and SSD contribution will be of 55,1 MPa. This represents 11% of the value of σ_y for ferrite in this case.

As a conclusion, the determination of both GNDs and SSDs dislocations density can be done by a combination of R-ECCI and EBSD measurements. This will afford the best compromise in terms of sample preparation and observation time with measurement accuracy. This is of particular interest for this type of multi component systems as the same areas can be characterized using both techniques, and the large size of the samples can allow to choose adequate locations to feed the models (inside grains, at grains boundaries, at phase boundaries, etc…).

4.5 Conclusion

In this study, several approaches for measuring dislocation density in deformed and undeformed materials were compared. XRD, EBSD, HR-EBSD, TEM and ECCI imaging were used to obtain the dislocation density present in industrial steel samples composed of austenite and ferrite phases for the following strain rates: 0, 5 and 10%.

Imaging methods saturate for densities above 10^{14} m^2. Density obtained by XRD is always high and not very accurate for low densities. The HR-EBSD and classical EBSD methods seem to be more versatile, for all observed densities and the increase the dislocation density with the strain is well capture by EBSD or HR-HEBSD. At the grain scale, the GND density obtained with both method is very similar. Locally, dislocations structures and strain concentration are better evidenced using the HR-EBSD technique.

Imaging techniques such as TEM and ECCI, as well as XRD, primarily measure the contribution of SSDs.

EBSD and HR-EBSD mainly measure the GND denisty. In this case: EBSD and HR-EBSD measurements (GND) are always higher than TEM, ECCI and XRD measurements (SSD), and they are located at the grain boundaries. The ratio between SSD and GND varies with the level of deformation, for the highest cases there are twice as many GND as SSD. These differences directly affect the calculation of hardening in micromechanical models, and must be carefully chosen.

Chapter 5

Validation of the R-ECCI Clustering method on a KME type mechanical model

Sommaire

5.1 Introduction

The R-ECCI method presented in the previous chapter allowed us to characterize dislocation densities and to establish the limits and uncertainties of the method. The chapter 4 showed that the different methods for measuring dislocation densities all have their particularities. Indeed, each method observes only a part of the information, either the density of Geometrically Necessary Dislocations (GND) for EBSD and HR-EBSD or of Statistically Stored Dislocations (SSD) for XRD. The imaging methods (TEM and SEM) theoretically observe both types of dislocation densities. However, the superposition of dislocations in the form of dislocation cells or walls can make it difficult to characterize the SSDs contained in the material.

The mechanical models based on flow stress, grain size and dislocation evolution are validated by experimental data. However, the studies comparing the models with experimental values use different methods such as TEM imaging [BAB 13], X-ray diffraction [MUÑ 21] or EBSD [FOL 22]. Moreover, the literature is not always clear on what each method can measure. For exemple in the case of XRD: Zribi *et al.* [ZRI 19] declare that it mainly measure GND densities while for Wauthier-Monnin *et al.* [WAU 15], XRD is more sensitive to SSD. It is therefore legitimate to wonder which density should be used in mechanical models and how it can be characterized.

The dislocation densities obtained by the R-ECCI clustering method can be used in mechanical models. However, it is necessary to compare the experimentally measured values with those predicted by mechanical models. Mathevon *et al.* [MAT 20] recently developed a mechanical model based on the physical parameters of the microstructure (martensite fraction, initial ferritic grain size), which allows to accurately describe the mechanical behavior of Dual Phase (DP) steels. Hybrid model does not use the dislocation density as input. It is calculated from other microstructure and deformation parameters. By using the dislocation density as an internal variable, the hybrid model can faithfully reproduce the experimental observations.

In addition, a disorientation gradient has been observed at the ferrite-martensite grain interfaces for DP600 steels. This gradient is generated by the existing deformation incompatibility between the two phases and causes additional GND-type dislocations to appear at the ferrite-martensite grain boundaries to accommodate the deformation of the material.

Therefore, this model can be used to validate the measurements performed by R-ECCI Clustering. Indeed, it will be possible to compare the experimental measurements along the deformation gradient with the values calculated from a model that accurately reproduces the mechanical behavior of the sample. The difference between the measured and predicted dislocation density will be discussed and the experimental densities will be implemented into the predictive models to observe the differences between the model fits and the experimental curves.

5.2 State of the art

The following section will focus on the mechanical behavior of Dual Phase (DP) steels. They are characterized by a low yield strength (YS), high fracture toughness (UTS) and high work hardening (WH). Therefore, they present a good energy absorption capacity. The high strain hardening of DP steels is obtained by the deformation of a hard phase (martensite) contained in a soft matrix (ferrite).

In the case of DP steels, the mechanical properties are particularly dependant on the martensite fraction, the chemical composition and grain size. It was shown (Figure 5.1) that the martensite fraction is an important parameter that controls the UTS and YS [MAR 82], [LIE 02].

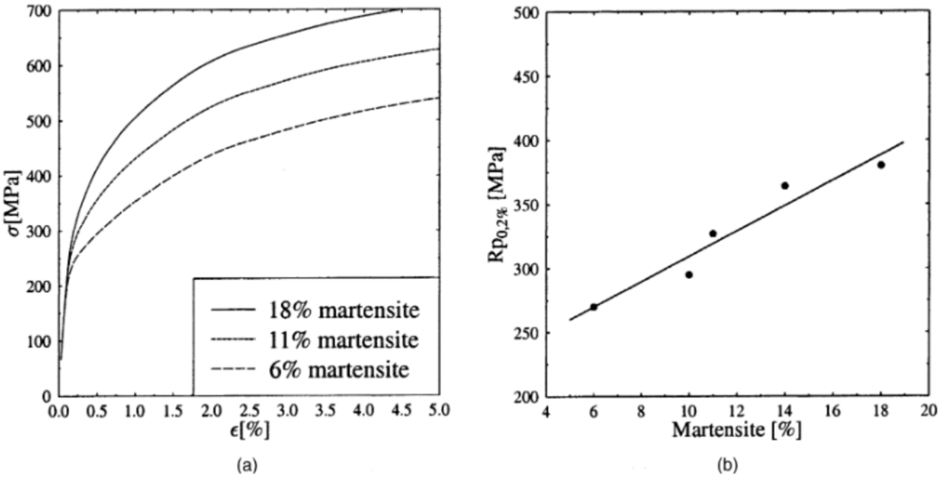

Figure 5.1: Experimental results of tensile tested dual-phase steel grades: (a) stress–strain diagrams for different martensite volume contents and (b) 0.2% yield strength (Rp0:2%) over the martensite volume content by U. Liedl *et al.* [LIE 02]

A Hybrid Mean-Field Composite (Hy-MFC) model has recently been developed by Mathevon *et al.* to predict the mechanical properties of DP steels during tensile tests. It takes into account the grain size and the volume percentage of each phase. This model is applicable to DP steels (for any proportion of martensite) and can be coupled to the hybrid models (or Hybrid Mean-Field Composite (Hy-MFC) model) for predicting the microstructural state. The Hy-MFC model is composed of two different models, the first one for a 100% ferritic steel and the second one for a 100% martensitic steel and a mixing law to couple these models. The model mainly based on the work of Allain *et al.* [ALL 15] uses the properties of each phase separately (ferrite and martensite) and then combines them by a homogenization law according to the phase fractions to obtain the macroscopic properties of the steel.

5.2.1 Ferrite model

E.O. Hall and N.J.Petch [HAL 51b], [PET 53a] first studied the mechanical properties of ferrite. Subsequently, many studies have developed physical models to reproduce the hardening mechanism [DEL 07], [SIN 06a]. These studies have shown that the grain size and dislocation density are important parameters. The constitutive law used by Mathevon *et al.* is based on the work of Bouaziz *et al.* [BOU 08].

It is possible to consider the flow stress σ_f as a function of the plastic strain such that:

$$\sigma_f(\varepsilon_p^f) = \sigma_0^f + \sigma_R^f + \sigma_X^f \tag{5.1}$$

With ε_p^f the plastic deformation, σ_0^f the sum of the Peierls force and frictional stress contributions related to the alloying elements in solution. σ_R^f is the isotropic hardening (or forest dislocation hardening) dependant on ρ_f, the density of SSD contained in the ferrite (5.2) and σ_X^f the kinematic hardening generated by the density of GND created during deformation (5.3).

σ_R^f and σ_X^f are defined as:

$$\sigma_R^f = \alpha_T M_T \mu b_{111} \sqrt{\rho_f} \tag{5.2}$$

$$\sigma_X^f = \frac{M_T \mu b_{111}}{D_\alpha^0} n^f \tag{5.3}$$

Where α_T is the forest hardening coefficient, M_T is the Taylor factor, μ is the elastic shear modulus, b_{111} is the burger vector (other possible directions of the burger vector are neglected), D_α^0 is the initial ferrite grain size and n^f is the average number of GND-type dislocations accumulated to accommodate the deformation and calculated through:

$$\frac{dn^f}{d\varepsilon_p^f} = \frac{\lambda^f}{b_{111}} \left(1 - \frac{n^f}{n_0^f}\right) \tag{5.4}$$

Allain *et al.* [ALL 15] used a KME type law to describe the evolution of the dislocation density as a function of the deformation. In addition to the dislocation creation and annihilation terms, a third term is added to take into account the effect of grain size on the increase of the dislocation density, by assuming an accumulation of GND at the grain boundaries [SIN 06a], [BOU 08], such as :

$$\frac{\partial \rho^f}{\partial \varepsilon_p^f} = M_T \left(\frac{1 - \frac{n^f}{n_0^f}}{b_{111} D_\alpha^0} + k^f \sqrt{\rho^f} - f^f + \rho^f \right) \tag{5.5}$$

With k^f and f^f two parameters controlling the KME law and n_0^f representing the maximum number of dislocations needed to accommodate the deformation at the grain boundaries.

Mathevon *et al.* [MAT 20] were able to reproduce the behavior of ferrite with this model and compare it to experimental measurements (Figure 5.2) on steels with different grain sizes.

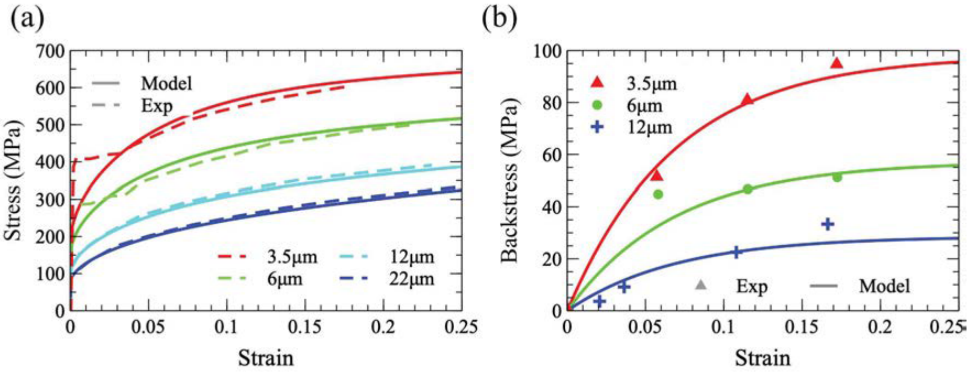

Figure 5.2: Model calibration for ferritic steels with grain sizes ranging between 3.5 and 22 µm: stress evolution during tensile test [MAT 20]

5.2.2 Martensite model

It is difficult to reproduce the mechanical behavior of a martensitic steel because traditional work hardening mechanisms do not explain the behavior observed between the yield point and the fracture point. It is therefore necessary to consider martensite as a «heterogeneous and continuous» composite. Many studies have shown that internal stresses and carbon content in martensite influence the mechanical properties in DP or martensitic steels only [PUS 13], [HE 14], [HUT 18].

In this section Mathevon *et al.* uses a continuous composite approach (CCA) by assuming that the harder phase of the composite remains elastic while the softer phase controls the plastic deformation. The different yield strength and a constant Young's modulus Y for the two phases allow for perfect control of the mechanical behavior of the composite material. The function $f(\sigma_l)$ is a continuous probability density distribution allowing to find a domain with a yield point σ_l.

$$\frac{d\sigma^m}{d\varepsilon^m} = \frac{1}{\frac{1}{Y} + \frac{F(\sigma_l)}{\beta}}(1 - F(\sigma_l)) \tag{5.6}$$

With $F(\sigma_l) = \int_0^{\sigma_l} f(\sigma) d\sigma$ is the probability density and β is a constant that describes the interraction between the different element of the composite.

To generate the work hardening contribution due to the stress difference between the two phases of the composite, it is necessary to condition the values of $F(\sigma_l)$ such as:

$$\text{if } \sigma_l < \sigma_0^m + \sigma_{min} \text{ then } F(\sigma_l) = 0 \tag{5.7}$$

$$\text{else } F(\sigma_l) = 1 - exp\left[-\left(\frac{\sigma_l - (\sigma_{min} + \sigma_0^m)}{\Delta}\right)^m\right] \tag{5.8}$$

σ_0^m is the sum of the Peierls force and frictional stress contributions related to the alloying elements in solution. σ_{min} is the yield strength (equal to 320 MPa [MAT 20]) and m is the strain hardening rate of the composite according to the Avrami law. Δ is the local yield strength distribution and is related to the work hardening between yield strength and ultimate tensile strength [ALL 12], [MAT 20].

The models presented by Mathevon *et al.* [MAT 20] have been calibrated for a wide range of DP steels with different carbon and manganese contents in order to predict the mechanical properties of martensite. Indeed, for a constant manganese content and a constant grain size, increasing the carbon content significantly increases the tensile properties of the steel but also the strain hardening rate. The manganese content, on the other hand, has only a small impact on the tensile properties of the material under consideration. Grain size in DP steels is an important parameter for martensite and its mechanical properties [VAN 17]. In Figure 5.3, it can be seen that the grain size has a significant effect on the tensile properties of ternary and industrial steels of identical composition.

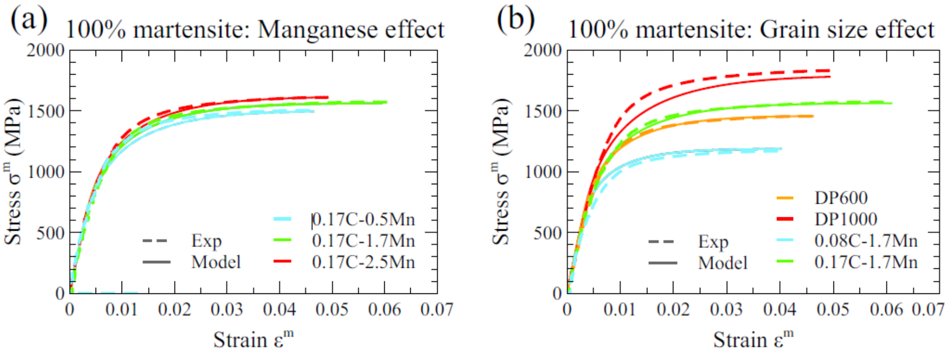

Figure 5.3: Comparison between experimental data and modelling. Effect on the tensile properties of the manganese content (a) and prior austenitic grain size (b) [MAT 20].

5.2.3 Hybrid Mean-Field Composite (Hy-MCF) model

Using the laws previously detailed for fully ferritic and fully martensitic steels, Mathevon *et al.* [MAT 20] have developed a composite law taking into account their interaction. The formalization of the interaction used is that of Allain *et al.* [ALL 15]. The equations governing ferrite have been modified, as they were only valid for a single phase material. They now take into account the creation of GND in the ferrite. The first source of GND comes from the expansion of the martensite during its formation:

$$\rho^f(\varepsilon_p^f = 0) = f_{\alpha'} \frac{M_T}{b111 D_\alpha^0} \varepsilon_0 \tag{5.9}$$

$f_{\alpha'}$ is the martensite fraction, D_0 the initial ferritic grain size and ε_0 is an initial deformation factor that integrates the dislocation density inside the ferrite and allows to reproduce the observed experimental curves.

The second source of GND comes from the incompatibility of the two phases during the deformation of the material. Indeed, the mechanical properties of ferrite and martensite are different and the deformation will be privileged in the ferrite grains for the first stages of the deformation.

$$\rho^{GND} = \frac{f_{\alpha'}}{b_{111} L_F} \frac{\left[1 - exp(-\beta_{GND}(\varepsilon_{tot}^f - \varepsilon^m + \varepsilon_0))\right]}{\beta_{GND}} \tag{5.10}$$

With L_F is the characteristic dispersion length of Ashby GND and β_{GND} is a parameter limiting the saturation effect of GND.

Schematically (Figure 5.4), these two phenomena consist in assuming that the interaction between ferrite grains and adjacent martensite grains takes place only over a characteristic distance Lf inside the ferrite grain.

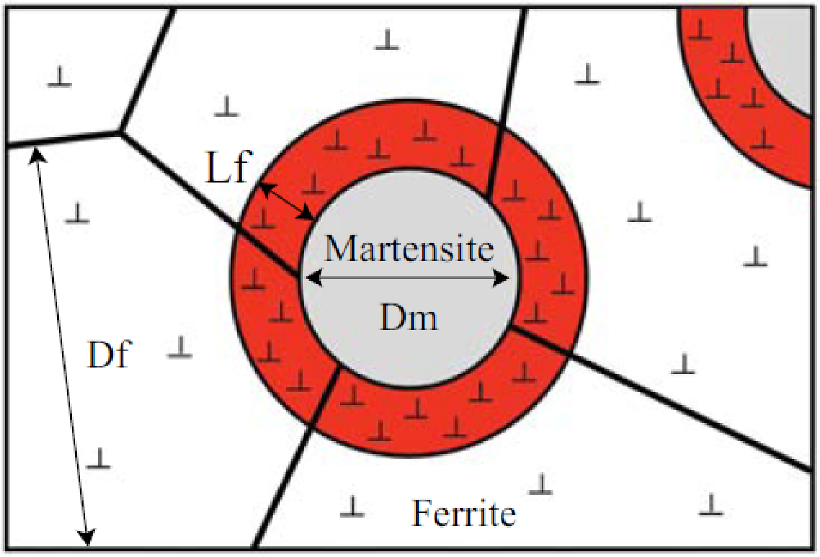

Figure 5.4: Scheme describing the characteristic length L_f of the martensitic island interaction zone within ferritic grain [MAT 20]. With L_f the characteristic dispersion length of Ashby GND

The characteristic dispersion length L_F is the length over which the GNDs disperse in the ferrite around the interface with the martensite and depends on the grain size of both phases. It has been shown that the length L_F can be calculated as follows [ALL 15]:

$$L_F = 0.0225 D^0_\alpha \frac{f_{\alpha'}^{\frac{1}{3}}}{1 - f_{\alpha'}^{\frac{1}{3}}} \tag{5.11}$$

In addition to the martensite concentration $f_{\alpha'}$ and the initial ferrite grain size D^0_α, it is necessary to know the carbon concentration C^m_c in the martensite, as specified in the previous section.

In this model, the new forms of σ^f_R (5.2) and of $\frac{\partial \rho^f}{\partial \varepsilon^f_p}$ (5.5) are modified to consider ρ^{GND} and become:

$$\sigma^f_R = \alpha_T M_T \mu b_{111} \sqrt{\rho^f + \rho_{GND}} \tag{5.12}$$

$$\frac{\partial \rho^f}{\partial \varepsilon^f_p} = M_T \left(\frac{1 - \frac{n^f}{n^f_0}}{b_{111} D^0_\alpha} + k^f \sqrt{\rho^f + \rho_{GND}} - f^f + \rho^f \right) \tag{5.13}$$

To model the DP600 steel and its mechanical properties, a mixing law is used [BOU 02] to express the macroscopic stresses of the steel as a function of the properties of the two phases weighted by their volume fractions. However, this model does not consider the interaction between the two phases. To solve this problem, Mathevon *et al.* [MAT 20] uses a scale transition law between the two phases, a so called « iso-work » law [BOU 02]. This law assumes the equality of the mechanical work dissipated by each of the phases and it is particularly effective for small fraction of martensite. When the martensite fraction exceeds 20%, the proposed model underestimates the work hardening of the material. Therefore, the model proposed by Mathevon *et al.* is based on an iso-deformation law at the beginning of the deformation that will then tend linearly towards an iso-work law. The martensitic structure will thus block the ferrite deformation at the beginning. Such that :

If $\varepsilon^f < 0.04$ and $f_{\alpha'}$ >20% then :

$$d\varepsilon^f = d\varepsilon^m \left(1 + \left(\frac{\sigma^m}{\sigma^f} - 1\right)\left(\frac{\varepsilon^m}{\varepsilon_c^m}\right)\right) \tag{5.14}$$

Else:

$$d\varepsilon^f \sigma^f = d\varepsilon^m \sigma^m \tag{5.15}$$

With ε_c^m is the critical deformation for which we assume martensite fracture and above which the iso-work law is assumed.

This model was able to reproduce experimental curves accurately for DP600 steels (Figure 5.5(a)). The experimental observations and the good reproduction of the mechanical properties show the importance of the term ρ_{GND} in the prediction of the mechanical model, validating the hypothesis of the deformation incompatibility between the phases.

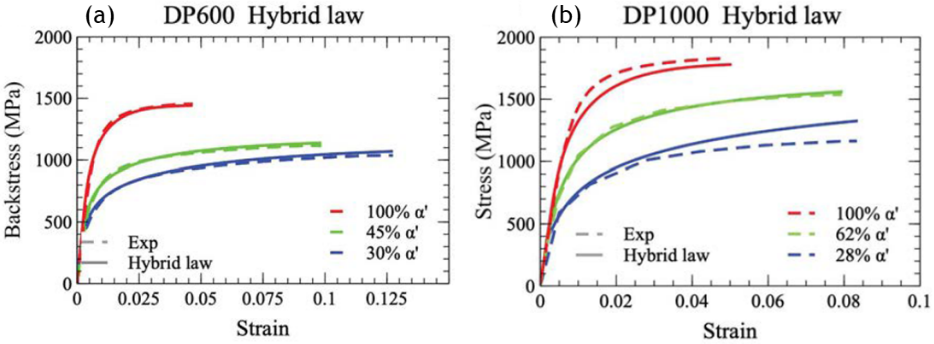

Figure 5.5: (a) Comparaison of simulated tensile and experimental curves with hybrid law for DP600 (b) Comparaison of simulated tensile and experimental curves with hybrid law for DP1000 [MAT 20]

In this study, it was decided to focus on the DP600 steel because the model was closer to the experimental curves than the DP1000 (Figure 5.5(b)). Since the dislocation density is an internal variable for both models, the value calculated by the model may be closer to reality in the case of DP600 than in the case of DP1000.

5.3 Material and method

This study was performed on an industrial dual phase (DP) steel and its chemical composition is summarized in the table below. It is a low carbon steel to which few alloying elements were added to improve the manufacturing process and its mechanical properties. The steel was hot rolled in the austenitic range, coiled at 600°C and slowly cooled to a ferritic-perlitic structure. A final cold rolling step with a reduction ratio of 55% was performed to obtain the plates used in this study.

Steel grades	Chemical composition C_i^0 (in wt.%)						
	C	Mn	Cr	Si	Nb	Ti	N
DP600	0.09	1.5	0.5	0.3	0.002	0.000	0.005

Table 5.1: Chemical composition C_i^0 of industrial steels for each element i.

5.3.1 Thermal traitements

In order to compare the results of this study with those found by Mathevon *et al.* [MAT 20], it was necessary to make the DP600 samples under the same conditions as the author. The use of salt baths was therefore mandatory. Salt baths have several advantages, in particular a high heating rate (200°C/s) which ensures a good control of the temperature and the treatment time while neglecting the time of temperature rise in comparison with the holding time. Moreover, the salt baths guarantee a homogeneous thermal zone over the whole length of the sample.

The sample was heated to 800°C in a barium chloride salt bath. The temperature was monitored by a thermocouple and the water quenching was performed after 3 minutes of heating to allow the appearance of martensite.

5.3.2 Deformation

In order to compare several values of the model, two specimens were used, one undeformed and the other deformed at 2%. A microtraction specimen was machined and deformed using a MTS tensile machine. Standard digital image correlation (DIC) was used to follow and precisely measure the deformation at each point of the sample surface and analyzed with the Ufreckles software [RÉT 18]. Figure 5.6(b) shows the appearance of a strain gradient on the specimen. This may be due to displacement of the tensile specimen during the test, so the tensile test was not purely uniaxial. However, an area of interest was identified for characterization and comparison with the model.

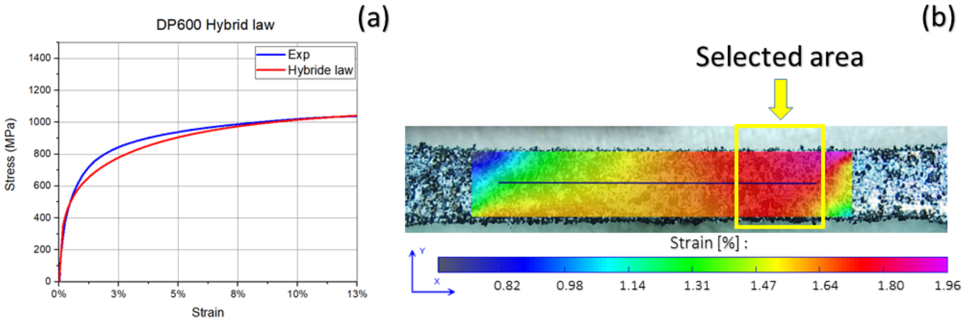

Figure 5.6: (a) Comparaison of experimental and simulated tensile curves with hybrid law. (b) Image obtained by DIC on the DP600 steel sample at the end of the tensile test.

The tensile curve obtained with the DIC treatment gives higher stress values than those predicted by the hybrid model (Figure 5.6(a)). However, the microtensile machine used in the mechanical test is a “soft‘’ machine, which deforms along with the sample. In addition, the specimen can move during the tensile test, therefore the tensile test is not uniaxial and overestimates the stress applied during the deformation. The DIC method was used to determine the strain rate and avoid errors due to the microtraction machine.

5.3.3 EBSD map and grain selection

The data acquisition time required for clustering can be very long depending on the case (several hours) and therefore the analysed grains must be carefully choosen. The Hybrid-Model developed on DP600 steels considers the dislocation density initially contained in the ferrite grains (ρ_f) and adds a contribution from the deformation of the ferrite grains next to the martensite grains (ρ_{GND}). It is therefore necessary to choose ferrite grains having a common interface with martensite grains. For this purpose EBSD maps were acquired. Martensite has the disadvantage of being indexed as ferrite on EBSD images, however on the Band Contrast map (Figure 5.7), the martensite grains appear dark (white arrows). Moreover, the martensite grains have the shape of small spheres surrounding much larger ferrite grains (yellow arrows).

The dislocation density ρ_{GND} can be measured on a characteristic dispersion length L_F (5.11) up to several μm. In order to reduce the number of grains to be characterized, the choice is made on the large ferrite grains which have a common grain boundary with another ferrite grain and also a common part with martensite grains.

For both samples (deformed and undeformed), four grains were chosen so that a dislocation density measurement could be made at three locations of these grains:

- at the level of the grain boundary with the neighboring ferrite ρ_{f-f} ;
- at the grain boundary with the neighboring martensite grains ρ_{f-m} ;
- at the center of the grain ρ_c.

These dislocation densities will be compared to those predicted by the model. The differences between the densities at the center of the grains and those near the martensite are expected to be close to those observed by Mathevon *et al.*.

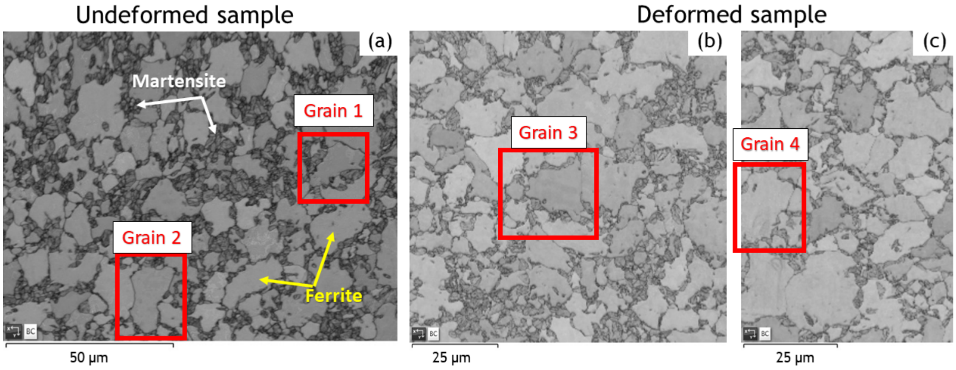

Figure 5.7: Band contrast obtained on DP600 samples. (a) Undeformed sample with grains 1 and 2 selected and examples of ferrite grain (yellow arrows) and martensite grain (white arrows). (b) and (c) Selection of grains 3 and 4 in the deformed sample.

5.4 Results

5.4.1 R-ECCI Clustering

As mentioned in the previous section, three density measurements were made per grain. In Figure 5.8 the three density measurements are shown (ρ_c at the center of the ferrite grain, ρ_{f-f} at the grain boundary of two ferrite grains and ρ_{f-m} at the grain boundary with martensite grains).

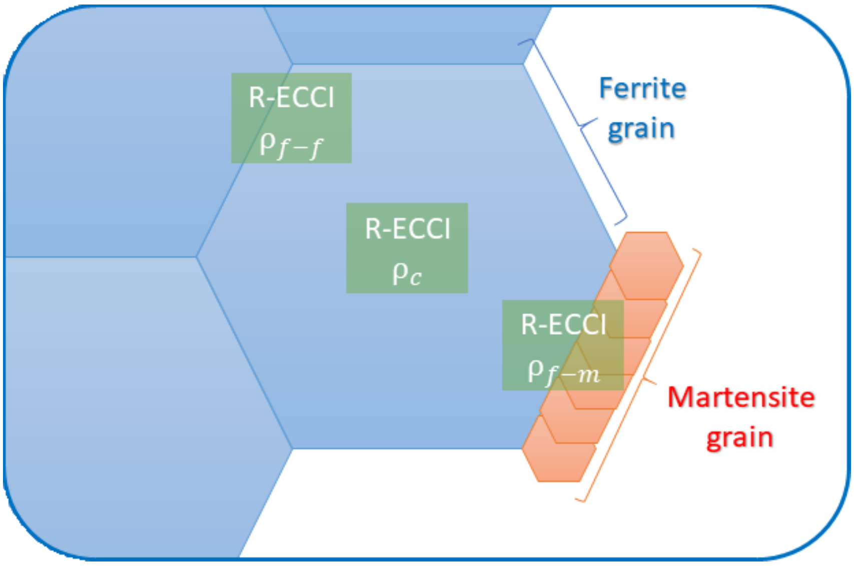

Figure 5.8: Illustration of the zones characterized with the R-ECCI method (in green) on ferrite grains (in blue) and near martensite grains (in red).

Figure 5.9(a) shows an example of the R-ECCI acquisition result at the center of an undeformed ferrite grain. In the BSE image, dislocations appear in white on a black background and a deformation contrast is observed. As in Chapters 2 and 4, the ferrite is deformed and dislocation appear diffuse, which adds to the difficulty of clustering. In addition, the dislocation density in the initial state is already high, so it was necessary to proceed in steps for post-processing the data. A first density measurement was obtained by the clustering software on the complete image series. This value was then refined by using a mask to remove the parts where the loss of information was important. By superimposing the images obtained by the clustering software (Figure 5.9(b)), there are still areas where dislocations were only partially detected (yellow circles) and the formation of important clusters appears on the edge of the images (red arrows). In these conditions, the dislocation density measured at the center of the grain by the clustering method is $\rho_c = (7.9 \pm 1.4) \times 10^{13}$ m^{-2}. Even if the dislocation density relies within the measurable range, the dislocation detection is not very convincing in this case, and does not seem to well describe the dislocation population. Therefore, an additional manual measurement of the density was performed on the image stack. Stacking all the images allowed to partially delete the contrast changes within the grains and obtain an image with an homogeneous matrix/dislocation contrast, for which an image analysis is rather possible.

The measurement obtained by the clustering method is high for this method and approaches the possible characterizable limits. In order to ensure that the measurements obtained by clustering are close to reality, a similar measurement was performed by hand. By plotting all the dislocations visible in red on Figure 5.9(a), it is possible to use the same formula as for clustering by counting the number of red pixels contained in Figure 5.9(c). The dislocation density measured is $\rho_c = (8.0 \pm 1.5) \times 10^{13}$ m^{-2}.

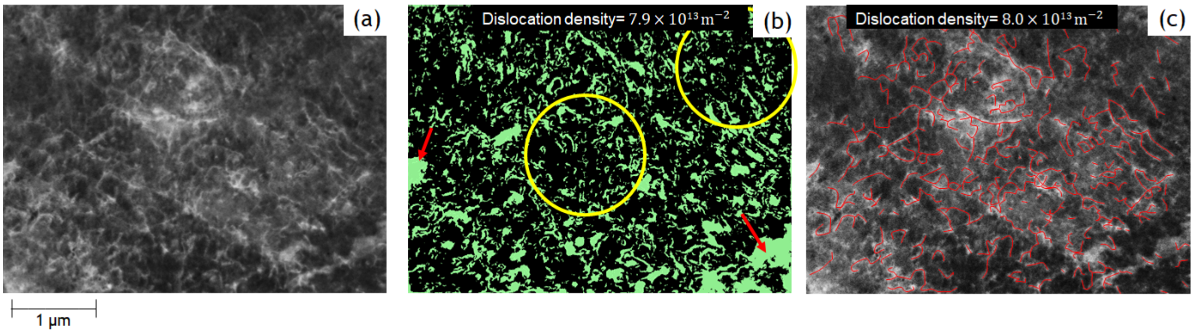

Figure 5.9: Ferrite grain in the undeformed sample. (a) Sum of BSE image stack acquired at the center of the grain with a voltage of 20kv and a pixel size of 4.5 nm. (b) Image from clustering showing dislocations detected in green.(c) Sum of BSE image stack where dislocations were manually drawn in red.

In the sample deformed at about 2%, the same data post-processing was used. However, the contrast changes near the grain boundaries become significant and impossible to remove with post-processing (Figure 5.10(d) yellow circle). This contrast is partly due to the deformation but also due to the presence of the grain boundary with martensite, since these significant contrast changes are not observed inside the grain or on the ferrite-ferrite interface (Figure 5.10(a)). In addition, the presence of martensite makes image acquisition more difficult. Indeed, martensite is magnetic and requires a fine tuning of the focus and astigmatism parameters for each image. Moreover, the acquisition time per image had to be increased to between 2 and 3 minutes to keep a good image quality, compared to 1 minute 30 seconds for the images of the undeformed sample. When detecting dislocations, large clusters appear near the image edge or grain boundary (Figure 5.10(b) and (e) yellow circle). Moreover, very clustered dislocations are detected as a single cluster (Figure 5.10(b) and (e) red arrow). The detection error is therefore too high, and clustering measurement are not reliable in this case. Indeed, clustering gives dislocation densities $\rho_c = (1.4 \pm 0.4) \times 10^{14}$ m^{-2} for the ferrite-ferrite interfacial and $\rho_c = (1.3 \pm 0.4) \times 10^{14}$ m^{-2} for the ferrite-martensite interfacial. These dislocation densities are high and close to the limit of what clustering can measure. therefore, a verification was performed manually by tracing all dislocations by hand (Figure 5.10(c) and (f)) and dislocation densities close to what clustering gave were obtained, $\rho_c = (1.3 \pm 0.4) \times 10^{14}$ m^{-2} for the ferrite-ferrite interface and $\rho_c = (1.5 \pm 0.5) \times 10^{14}$ m^{-2} for the ferrite-martensite interface. Even if the manual measurement is very close to the measurement obtained by clustering, it is important to point out that the clustering measurement is no longer reliable for these dislocation density ranges ($< 10^{14}$m^{-2}).

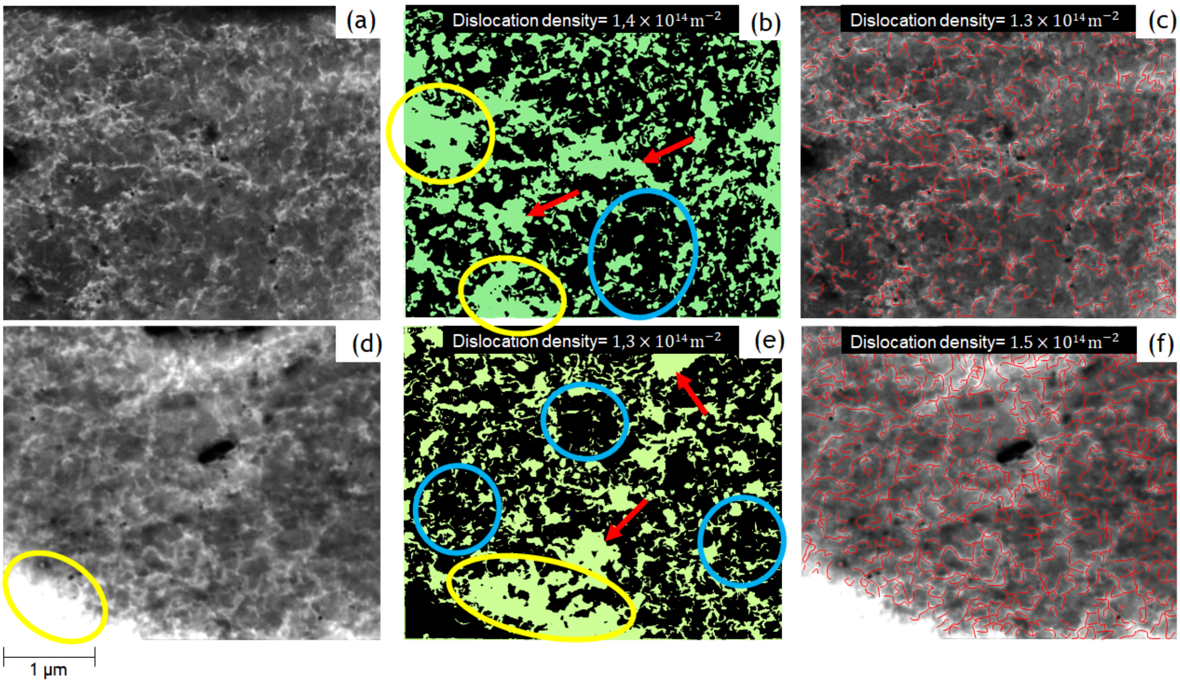

Figure 5.10: Ferrite grain in the sample deformed to about 2%. (a) Sum of BSE image stack acquired at the ferrite-ferrite interface and (d) at the ferrite-martensite interface with a voltage of 20kv and a pixel size of 4.5 nm. (b) and (e) Images from clustering showing dislocations detected in green. (c) and (f) Sum of BSE images stack where dislocations have been manually drawn in red.

The average values of the measured density are summarized in Table 5.2. In the measured grain set, the values obtained manually and by clustering have overlapping uncertainties. However, in the undeformed sample, the densities measured by clustering are systematically higher than the values obtained manually. On average, clustering finds 0.9×10^{13} m^{-2} more than the manual value. However, this difference is no longer found in the values obtained for the deformed sample. These differences can be explained by the different areas that are either over-or undervalued by the clustering. Although the undervalued areas are larger in the distorted sample than in the deformed sample, the overvalued areas are also larger. However, the difference between these two types of areas may be negligible in the distorted sample since the undervalued areas are much larger than in the undistorted sample.

Ferrite grain underformed		
	cluster	manually
ρ_c	$(9.2 \pm 1.3) \times 10^{13}$ m^{-2}	$(8.0 \pm 1.2) \times 10^{13}$ m^{-2}
ρ_{f-f}	$(1.1 \pm 0.2) \times 10^{14}$ m^{-2}	$(9.9 \pm 1.5) \times 10^{13}$ m^{-2}
ρ_{f-m}	$(9.8 \pm 1.5) \times 10^{13}$ m^{-2}	$(9.0 \pm 1.3) \times 10^{13}$ m^{-2}
Ferrite grain derformed at 2%		
	cluster	manually
ρ_c	$(1.2 \pm 0.3) \times 10^{14}$ m^{-2}	$(1.0 \pm 0.3) \times 10^{14}$ m^{-2}
ρ_{f-f}	$(1.3 \pm 0.4) \times 10^{14}$ m^{-2}	$(1.4 \pm 0.4) \times 10^{14}$ m^{-2}
ρ_{f-m}	$(1.4 \pm 0.4) \times 10^{13}$ m^{-2}	$(1.3 \pm 0.4) \times 10^{14}$ m^{-2}

Table 5.2: Average density value obtained on the undeformed and approximately 2% deformed samples. For the different positions ρ_c, ρ_f and ρ_{f-m}.

5.4.2 Comparison with the theoretical model

The hybrid model (My-MCF) developed by Mathevon *et al.* [MAT 20] uses two distinct densities ρ_f (density in ferrite due to deformation) and ρ_{GND} (density in ferrite due to the presence of martensite). The density ρ_{GND} induced by the martensite formation located at the grain boundaries. Figure 5.11 shows the evolution of ρ_f and ρ_{GND} during deformation. Both densities are internal variables that are calculated and originates from the input data (stress strain curve, microstructural data, and variables chosen).

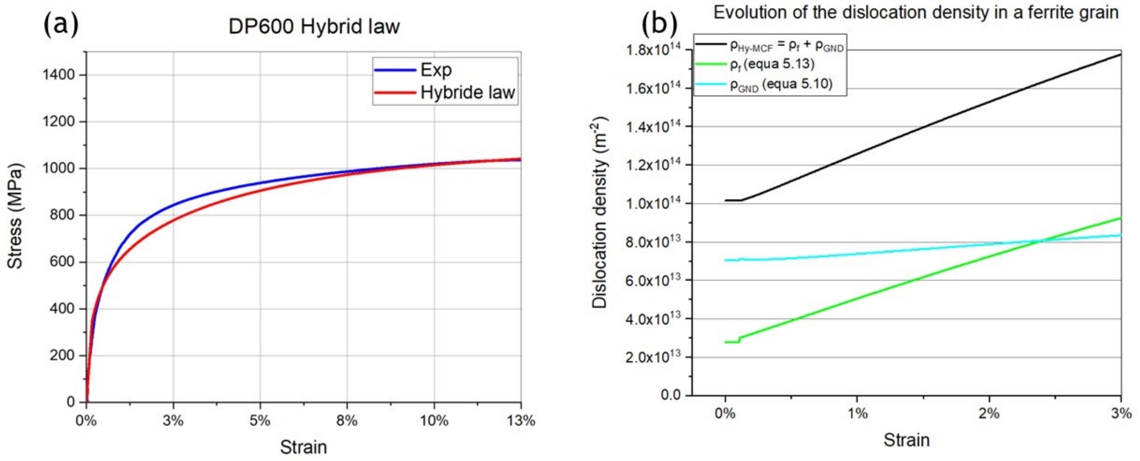

Figure 5.11: (a) Comparaison of simulated tenisle and experimental curves with hybrid law for DP600 [MAT 20]. (b) Evolution of the total dislocation density (black curve), the dislocation density in the ferrite alone (green curve) and in the GND due to the presence of martensite (blue curve).

The values used in the Mathevon *et al.* model are the same and all variables used (Taylor factor, Shear modulus, Burgers vector, Young's modulus, *etc*) are described in [MAT 20].

As ECCI imaging allows to measure all dislocations, ρ_{f-m} will be comparable to the sum of ρ_{GND} and ρ_f. The densities measured in isolated ferrite grains will be comparable to ρ_f. However, it was not possible to find ferrite grains perfectly isolated from the martensite. Therefore, measurements were made in the same ferrite grains as ρ_{f-m} but in different positions, close to the center (ρ_c) and close to the grain boundaries between two ferrite grains (ρ_{f-f}). The aim was to observe a measurement closer to ρ_f or a potential deformation gradient caused by the presence of martensite (Figure 5.12).

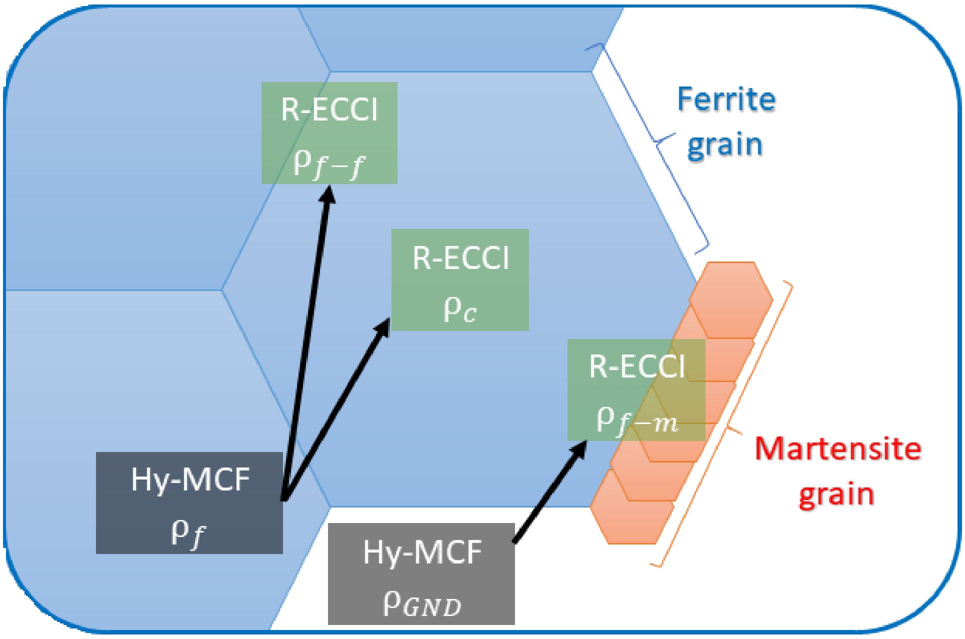

Figure 5.12: Illustration of the zones characterized with the R-ECCI method (in green) on ferrite grains (in blue) and near martensite grains (in red) and the correspondence with the values simulated by the model of Mathevon *et al.* [MAT 20]

Model calculation and experimental results are compared on Figure 5.13. In the undeformed sample, the densities measured at the ferrite/martensite interface (Figure 5.13(a)) are comparable: $\rho_{f-m} = (9.8 \pm 1.5) \times 10^{13}$ m^{-2} and $\rho_{GND} + \rho_f = 10.1 \times 10^{13}$ m^{-2}.

At the center of the grains, (Figure 5-13) the density measured in the ferritic grains is homogeneous with that at the ferrite martensite interface: $\rho_c = (9.2 \pm 1.4) \times 10^{13}$ m^{-2} and $\rho_f = (10.0 \pm 1.5) \times 10^{13}$ m^{-2}.

After deformation, the density measured at the grain boundary (Figure 5.13(a)) is higher than the one in the undeformed state, with $\rho_{f-m} = (1.4 \pm 0.4) \times 10^{14}$ m^{-2} and still rather in agreement with the one calculated : $\rho_{GND} + \rho_C = 1.5 \times 10^{14}$ m^{-2}.

At the center of the grain (Figure 5.13(b)), the increase observed experimentally is in godd agrement with the increase derivated from the model.

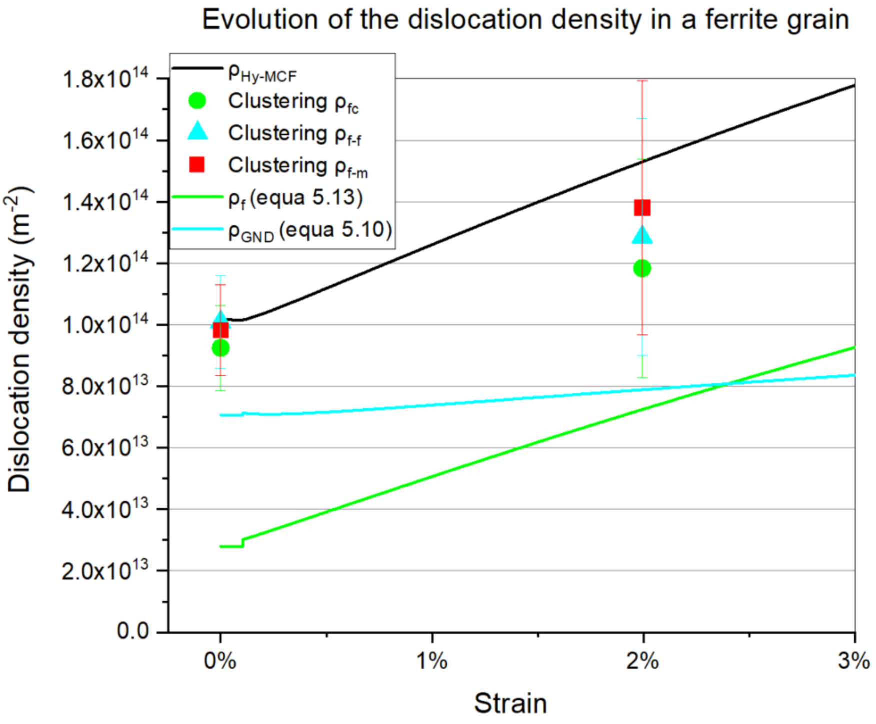

Figure 5.13: Comparison of dislocation density for different positions in a ferrite grain as a function of strain. (a) ρ_{f-m} obtained with R-ECCI near the common grain boundaries with martensite, measurements of ρ_f and ρ_c obtained with R-ECCI near grain boundaries in common with other ferrite grains and at the center of the ferrite grain compared with the total density values ($\rho_f + \rho_{GND}$) obtained by the Hy-MCF model.

5.5 Discussion

The density experimentally measured and the one derived from the modelling are of the same order, which validates the model data. In particular, there is a very good agreement between the dislocation densities located at martensite/ferrite grain boundaries. The esperimental values are slighlty lower than the one measured, which is expected, as, for those density values, ECCI systematically leads to an underestimation (see. Chapter 4).

The width of the ferrite affected region due to the presence of martensite (L_f) was however measured to be slighlty larger than the one used in the model. In the model, it was calculated to be around 560 nm while observations revealed homogeneous dislocation densities over areas larger than 5-10μm.

The ECCI observations are in agreement with EBSD measurement previsouly made on this sample (Figure 5.14 [MAT 20]), that indicate that some areas are affected over more than a μm (Figure 5.14(d) red arrows).

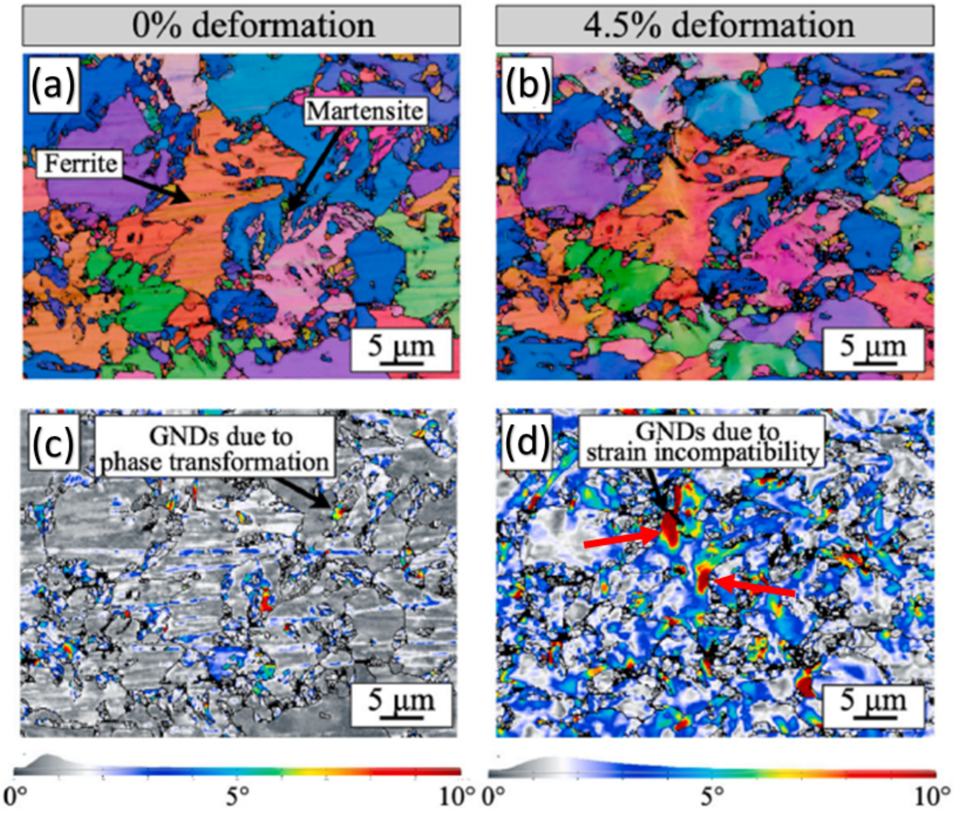

Figure 5.14: (a–c) IPFZ colour maps and (d–f) Kernel Average Misorientation (KAM) maps of EBSD observation made on the DP600 steel with 41% martensite for three 2 deformation values (0%, 4.5%). (For interpretation of the references to colour in this figure legend, the reader is referred to the Web version of this article [MAT 21]).

The dislocation density in the center of the ferrite grains is homogeneous to the density found near the ferrite-martensite interface. The homogeneous dislocation density in the grain is in agreement with the observations made by EBSD in the undeformed sample. No significant difference in dislocation density was observed in the 2% deformed sample. At 2% of deformation, no deformation gradient is observed within the grains from those ECCI measurement, whereas it is present after 4% of deformation (see EBSD results)

Moreover, the experimental increase in dislocation density seems slightly smaller than the one predicted from the model, but still within the measurement uncertainties.

Finally, the measurements and simulations are well in agreement, and do validate the experimental approach as well as the model used. It enhances the fact that it is of primary importance to well consider which population are imaged, and which one are considered into the modelling. Such density measurement could be used as input data in the model to fit those stress-strain curves.

5.6 Conclusion

The experimental values of the density have been checked and re-measured by hand (see Figure 5.10 (c) and (f)) for safety and even if differences appear, especially for the deformed sample, they remain within the measurement uncertainty. It can be concluded that the measured dislocation densities are close to the values expected by the model, even the experimental conditions present limitations and important uncertainties for densities above 10^{14} m^{-2} and cannot be used without a manual check.

It is difficult to conclude which density is closer to reality. The density obtained by the model is calculated from other internal variables and can give an approximate value. For the experimental values, other parameters come into play, such as the volume explored or the overlapping of dislocations. However, the model allows to reproduce very well the experimental curves. The volume used experimentally is in good agreement with other studies and the observations of chapter 2 allow to conclude that it is close to the optimized value. The fact of finding close values, whether by calculation or by imaging, is rather reassuring on the capacities of the R-ECCI method to characterize dislocation densities and to feed mechanical models, in the case of low dislocation density.

In this configuration, the use of the experimental values is not possible since the values obtained for the undeformed sample are very close to the simulated values and the deviation of the values in the deformed sample can be explained by the superposition of the dislocations and the loss of precision of the clustering for these density values. A third point of comparison at 1% strain would be ideal in Figure 5.11. This would allow us to determine if the trend of the curve is respected but with a shift in values which would imply a possible error in the determination of the volume analyzed. In the case where this new point is close to the theoretical curve, this would mean that the deviation at 2% deformation is due to the overlapping of dislocations.

Another possibility would be to repeat these observations on another sample, the DP1000. The simulated curves (Figure 5.5(b)) show differences with the experimental curves. This could allow measuring a dislocation density different from the one predicted by the model. In this case, it would be possible to apply the measurements obtained by R-ECCI Clustering to see if the model curves are close to the experimental curves.

Conclusion and Perspectives

Conclusion

The first objective of this thesis was to improve the method of automatic characterization of dislocations by the R-ECCI method and clustering and to bring precision on the limits and uncertainties of measurement. The change of algorithm and clustering strategy allowed to apply the method to deformed materials. The limit characterizable by the R-ECCI clustering method at the maximum of the order of magnitude of 10^{14} m^{-2} and at the minimum of about 10^{10} m^{-2}. The main sources of error are the explored volume and the superposition of dislocations. The uncertainty caused by the superposition and the apparent width of the dislocations evolves between 7 and 27% at most, depending on the observed density (Figure 2.11). This uncertainty does not consider the error made on the analyzed volume. Indeed, a change in the value of ξ_g can lead to errors on the analyzed volume of 20 to 70%. The uncertainty on the volume remains the weak point of the method. However, the observations made in Chapter 3 show that the thicknesses observed in ECCI would be closer to 140 nm than the 60 nm announced in the literature. Therefore, the average depth used in Chapters 2 and 4 seems to be consistent with all the observations and measurements made.

The second objective was to compare the different dislocation density measurement methods commonly used (R-ECCI, TEM, XRD, EBSD and HR-EBSD). This study has allowed to highlight the strengths of each method and their field of application. The imaging methods (TEM and ECCI) seem to be particularly efficient on dislocation densities lower than 10^{14} m^{-2} and on undeformed samples, whereas the indirect methods such as XRD and EBSD seem to be more efficient when the dislocation density is higher than 10^{14} m^{-2}. The HR-EBSD method seems to be the most versatile and gives values close to EBSD for high densities but with lower uncertainties. It also keeps good correspondence with the imaging methods for lower densities. Nevertheless, the HR-EBSD method is more expensive in acquisition time and more constraining than the classical imaging methods. To summarize, the imaging methods seem to be the most accurate for low dislocation density (from 10^{11} m^{-2} to 10^{13} m^{-2}), the XRD seems to be the most relevant for high density (higher than 10^{14} m^{-2}) and the HR-EBSD method seems to be the most versatile. The term σ_R (which is the forest dislocation hardening or isotropic hardening) and has been calculated with the different values obtained for each method. Values of σ_R far from the theory can be obtained if the wrong approach is used. Indeed, it is necessary to measure the initial density for the calculation and this gives an error of about 50% for the XRD against an error of about 5% for the imaging methods.

The third objective was to compare the measurements obtained with the R-ECCI clustering method with a mechanical prediction model. Chapter 5 compares the measurements obtained with the R-ECCI Clustering method on a dual phase 600 (DP600) steel with the values calculated from a mechanical model. The dislocation density values obtained in the undeformed and slightly deformed sample showed that the R-ECCI Clustering method can measure consistent values that can be implemented in mechanical prediction models. However, it is important to note that a model developed with EBSD data will be different from a model developed with ECCI data, due to the difference in measurement methods.

Perpectives

To continue this study, many directions are possible to enrich the knowledge on ECCI imaging, improve the clustering algorithm and diversify it. The main ideas are developed below:

Algorithms

Initially, the clustering algorithm was shown to be robust enough to obtain dislocation densities accurately. However, poorly indexed areas can appear (cf figure 4.3 blue circles and yellow arrows). These indexing problems come in part from the contrast that varies on the images (figure 1.24). Indeed, this contrast varies according to the deformation but can also be disturbed by the grain boundaries as it is the case on the images figure 5.10(d) and (e) (yellow circle).

The results obtained via clustering could be improved via a new method of processing the profiles by defining different zones. This would allow to treat the more difficult to characterize areas with finer parameters, without overestimating the thickness of dislocations in the more visible areas. Currently, during processing, a compromise is regularly made between these two types of zone in order to have a maximum of elements detected by clustering without overestimating the dislocation density in the other zones.

During these studies, another problem related to the algorithm appeared, that of "fictitious grain boundaries". This problem comes from the construction of the algorithm. Indeed, to optimize the speed of data processing, groups of neighboring pixels with similar profiles are made. This step is important in particular to build the different grains contained in the images. However, this optimization parameter is still present during the clustering steps. When the dislocations are strongly packetized as shown on figure 5.15(a), the algorithm can make appear grains which have for grain joint the dislocations (5.15(c) red circle). In this case, dislocations are "excluded" from the clustering and are not considered in the calculation of the dislocation density.

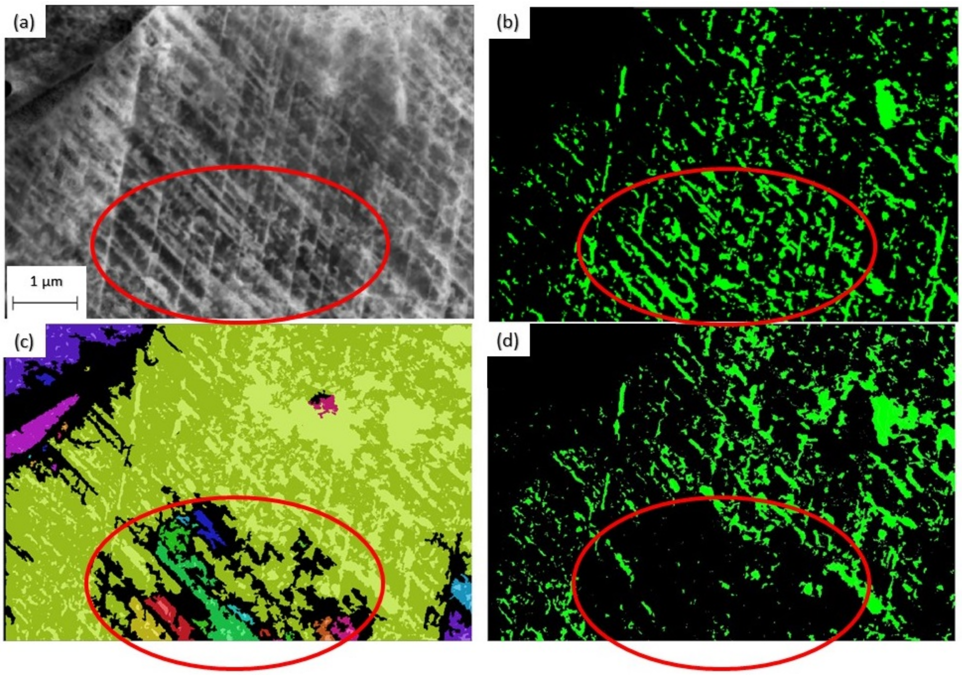

Figure 5.15: Highlighting of the dummy grain boundary problem. (a) EBSD map obtained on an austenite grain in a 3% deformed duplex steel sample. (b) clustering result obtained on (a) with optimized parameters. (c) cluster map obtained on (a) with fine parameters that confuse dislocation clusters with grain boundaries. (d) clustering results obtained on (a) with the parameters of (c) where dislocation clusters contained in the red circle have disappeared from the clustering.

Although the problem is simple, its solution is not trivial. The optimization of the algorithm is necessary. Otherwise, the duration of the calculations could take several hours and make the parameter iterations impossible to perform quickly. There are several ways to solve this problem. First, defining different areas in which different detection parameters will be applied can solve this problem, since these dummy grain boundaries are located at a single point in the grain. However, this method could still limit the accuracy of clustering in these areas. A second option may be to modify the pixel clustering method with more accurate mathematical algorithms to improve the process.

Acquisition

In order to develop the method and its possibilities, one of the next important steps would be to determine the crystallographic orientation of the grain within the data treatment software. The orientation was achieved in Chapter 3 using the CHORD method but in post processing. If it were possible to obtain this orientation during the tests in a faster way, it would greatly facilitate the acquisitions.

Indeed, when using the R-ECCI method, a fast acquisition at low magnification is performed (between 15 and 25 minutes) and a grain is chosen, generally the one with the most peaks in its intensity profile (sign of an orientation close to a zone axis). However, in a FIB sample, the choice of grain is very limited and it is possible to come across diffraction conditions that will be difficult to image (for example by being too close to another diffraction band (Figure 5.16, yellow circle green dot).

Rapid orientation determination during the low magnification acquisition would allow the ECP to be obtained and new tilt and rotation conditions to be defined in order to achieve more accurate Two Beam conditions (Figure 5.16 blue circle dot green).

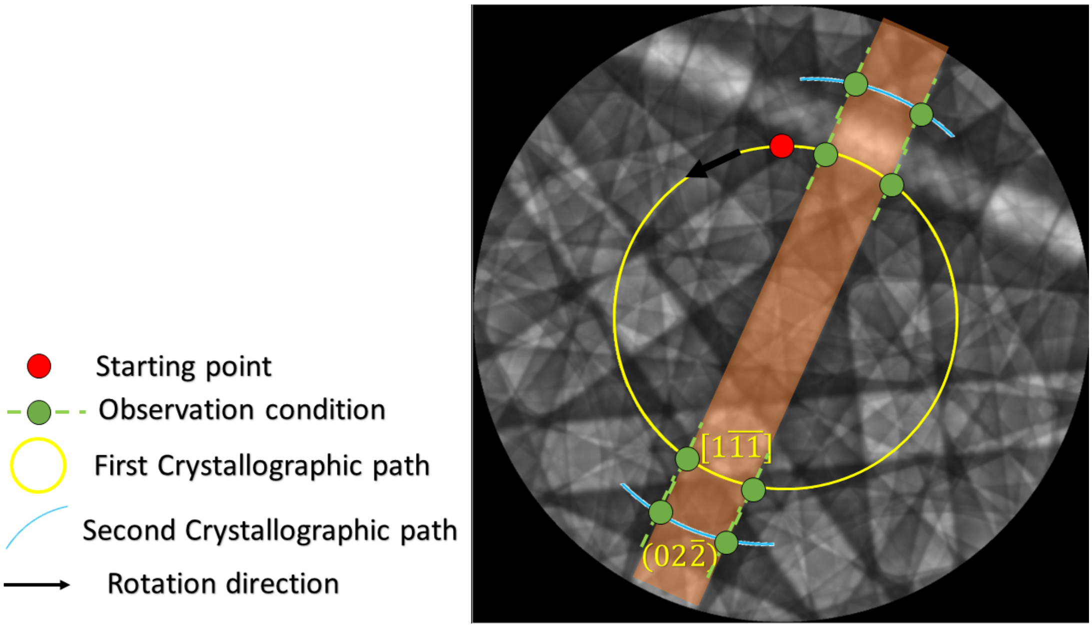

Figure 5.16: Simulation of the ECP of the austenite grain obtained with Emsoft [SIN 17] [GRA 19] showing the analysed rotation path associated with the R-ECCI method.

Obtaining the orientation and the ECP directly after the acquisition of the series of low magnification images would not only allow to multiply the characterizable observation conditions (with using a double tilted object holder) but also to use the R-ECCI method for other studies, in particular in the framework of the electron tomography of dislocations [BAR 06] or the indexing of vector bursters. Indeed, the application of the electronic tomography of dislocations to the SEM would allow to be more representative of the material but also to go back to a 3D dislocation density and thus to remove the uncertainty due to the overlapping of dislocations (2D projection effect, cf chapter 2). To perform these acquisitions, it is necessary to obtain several images at different positions on the Kikuchi band, which would be possible with the acquisition of the live ECP.

Moreover, being able to obtain a 3D volume of dislocations in a material can be a good starting point and comparison for Dislocation Dynamics simulations. The SEM allows to observe dislocations in microtensile specimens, which allows to make different acquisition on the same grain at different stage of deformation and to compare it to the results of a simulation obtained by DDD (Discrete Dislocation Dynamics).

One method to improve automatic acquisition would be to use image correlation. Currently, Joël Lachambre and Cyril Langlois are using a method for lower magnifications. Their image correlation method allows automatic CHORD-type acquisitions down to a pixel size of about 11 nm. The series acquired during this thesis were obtained with pixel sizes of about 4 to 5 nm.

However, for these pixel sizes, landmarks may be missing, which would require an additional step with a low magnification correlation. Doing so will result in much longer acquisition times for R-ECCI series, but manufacturers such as Tescan are improving instruments and detectors so that there are fewer problems with astigmatism and focus.

Uncertainty on the probed depth

Although the objective of chapter 3 was to specify the probed depth with the R-ECCI method, it was only possible to show that the depth is underestimated compared to those available in the literature and that the interactions between the different diffraction conditions (figure 3.10) also impact this value.

In order to obtain more precise information on the depth probed, one possibility would be to redo these analyses with a thin foil and to place oneself in the thickest possible grains and this for different diffraction conditions. Since the use of the CBED method allows us to obtain the local thickness in a precise way, the only difficulty is once again the ability of the R-ECCI method to find the orientation, to compare the right diffraction conditions and to find the same dislocations. Another possibility would be to use another material that has smaller values of ξ_g than austenite, which leads to smaller depth explored with the ECCI method.

ECCI Image Simulation

In order to better understand the channeling contrast, the domain around the diffraction bands where the dislocations are visible and to determine the visible characteristics of the dislocations which are different depending on the sample (tortuous shape, more or less contrasted etc), it is necessary to go through simulation steps.

Several samples were tested in order to determine the most suitable (Copper, Steel, Nickel). Even if the choice was made for Duplex steel and its two phases (ferrite and austenite), series of images were acquired on copper and nickel. The result is the appearance of significant differences in the apparent thickness of dislocations (Table 5.3). Moreover, as shown in chapters 2 and 4, dislocations appear differently in austenite and in ferrite (which is also the case in copper and nickel).

Sample	Apparent size (SEM)
Cooper	220 ± 14 Å
Ferrite	300 ± 26 Å
Austenite	320 ± 17 Å
Nickel	270 ± 24 Å

Table 5.3: Apparent width of dislocations present in different materials.

The use of the elastic theory of dislocations allows to simulate the deformation of the perfect crystal induced by the presence of a dislocation (Figure 5.17). With this deformation field defined for all the components of the ϵ matrix, it would be interesting to implement them in the simulation of ECCI images.

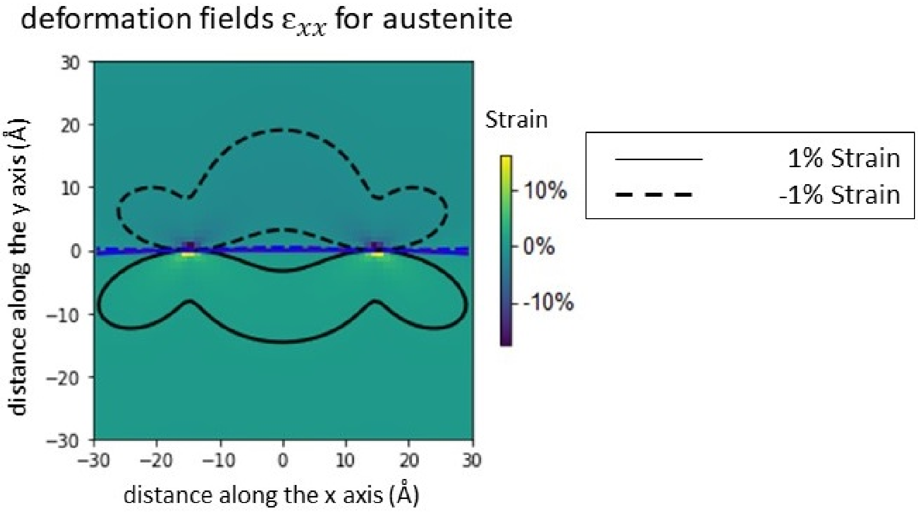

Figure 5.17: Elasticity field around a dislocation dipole in an austenite sample. The shape of the deformation field at 1% of the maximum deformation (at the core of the dislocation) is represented in black and in dotted lines

Currently, these ECCI imaging simulations consider the dynamic electron scattering matrix and incorporate the Darwin-Howie-Whelan dynamic equations for backscattered electrons moving from a range of depths within the sample towards the surface and towards the detector [PIC 14b]. However, the characteristics of the dislocation-induced deformation field are not yet considered.

Appendix A

Dislocation and mechanical properties

A.1 Plastic deformation and dislocation notion

When a material is deformed under a mechanical stress, it is possible to plot the evolution of this applied uniaxial stress, σ, on the material as a function of the deformation ϵ (Figure A.1). The material then passes through two distinct domains. The first is the elastic domain, which is linear for the metallic material and reversible. The second domain is the plastic domain, which is generally non-linear and irreversible. These two domains are delimited by a stress level σ_c (critical stress) that represents the elastic limit (Figure A.1).

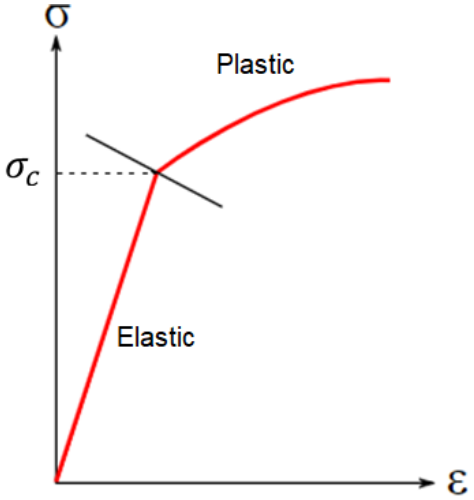

Figure A.1: Example of perfect stress/strain curve with the elasic limit separating the two domains (elastic and plastic).

A first explanation to describe the plastic deformation, by shear, of metallic materials consists in considering that each atomic plane 'slides' over its neighbor. Thus, the minimum stress 'τ' to be applied to shear the crystal is given by [FRE 26]:

$$\tau = \frac{G}{2\pi} \tag{A.1}$$

Where G is shear modulus.

Unfortunately, there is a large discrepancy between experimental observations and calculated values of τ, which indicates that another mechanism occurs during plastic deformation. G.I Taylor [TAY 34] explains that this difference is due to linear defects named dislocation, which break the periodic aspect of the structure.

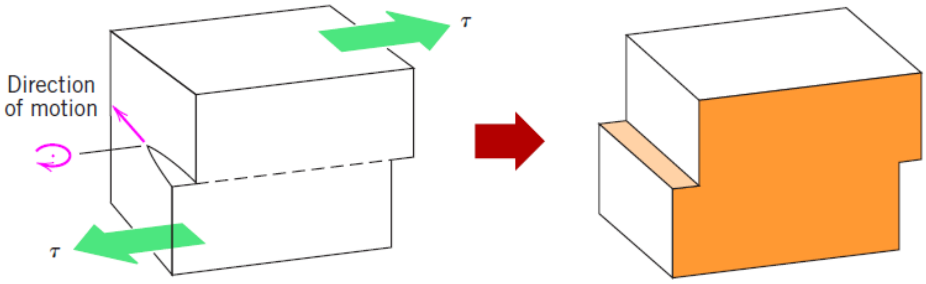

Figure A.2: Crystal sheared by the application of two forces (green arrow) [CAL 20]

When this linear defect is in movement in the crystal by the application of forces (Figure A.2), the crystal is sheared and the atomic rows which compose it will shift gradually until the appearance of a "step" on the edges crystal. This step is defined by the Burgers vector b, which represents the amplitude of the deformation and its direction. It is possible to define a second vector, the line vector $\vec{u}$, which defines the direction of the dislocation line.

To define the Burgers vector, there is a procedure, [HIR 83] which consists in describing a closed circuit in the indirect direction (Figure A.3.a). We call this closed circuit the Burgers circuit. The two points A and B define the start and the end of the circuit. When this circuit is reproduced in a deformed crystal (Figure A.3.b and c), the points A and B don't coincide anymore. We find then that the Burgers vector b is the circuit's closure failure, oriented from B to A. This vector, noted $\vec{b}$, does not depend on the form or the origin of the Burgers circuit.

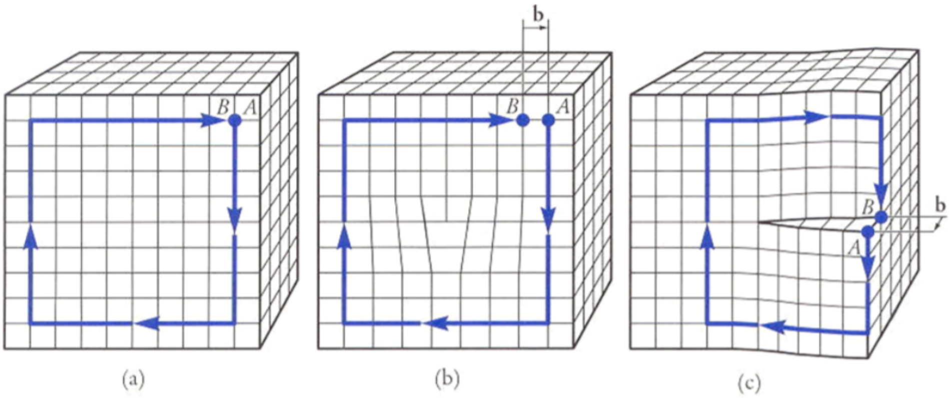

Figure A.3: Definition of the circuit that determines the Burgers vector. figure from [LAO 12].

There are two types of dislocation, the “screw” type (when $\vec{b}$ and $\vec{u}$ are collinear) (Figure A.3c) and the “edge” type (when $\vec{b}$ and $\vec{u}$ are orthogonal). For this last case, there is an additional half plane in the structure (Figure A.3b). However, in general, the dislocations are curved and their shape are complex. They can be considered as “edges” in some places and “screws” in others, or both at the same time. This last case is “mixed” and has edge and screw components.

The presence of dislocations in the structure will locally distort the crystal (the surrounded zone in Figure A.4, in the case of an edge dislocation). The dislocation generates a field of deformation and internal stresses in all the crystal. The closer to the dislocation, the more the atomic arrangement will be disturbed. This area is named the “core” and its size r_0 equals several times the norm of the Burgers vector $||b||$.

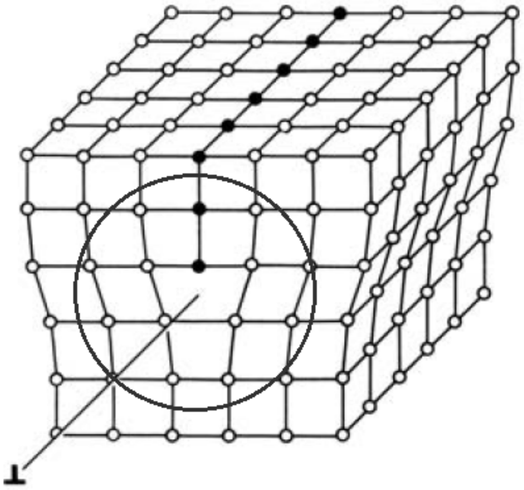

Figure A.4: Distorsion area [MES 10].

In order to describe the deformation field generated by a dislocation, the Hooke’s law can be applied. At the dislocation core, this theory is not valid anymore, due to the discontinuity of the atomic planes. This law allows the evaluation of the stress generated by the dislocation.

If we consider a purely “screw” dislocation, oriented along the axis and the height of a cylinder (Figure A.5). We can write the displacement along u_z, in polar coordinates, as follows:

$$u_z(r,\theta) = \frac{b}{2\pi}\theta \tag{A.2}$$

The resulting stress from this displacement is given by the following equation [FRI 64]:

$$\sigma = \begin{bmatrix} 0 & 0 & 0 \\ 0 & 0 & \sigma_{\theta z} \\ 0 & \sigma_{\theta z} & 0 \end{bmatrix} ; \sigma_{\theta z} = \frac{\mu b}{2\pi r} \tag{A.3}$$

With μ the Shear modulus, approximately equal to 80 GPa for metals. The “screw” dislocations only cause shear stresses. This is not the case for an “edge dislocation”, as shown in Figure A.5(b).

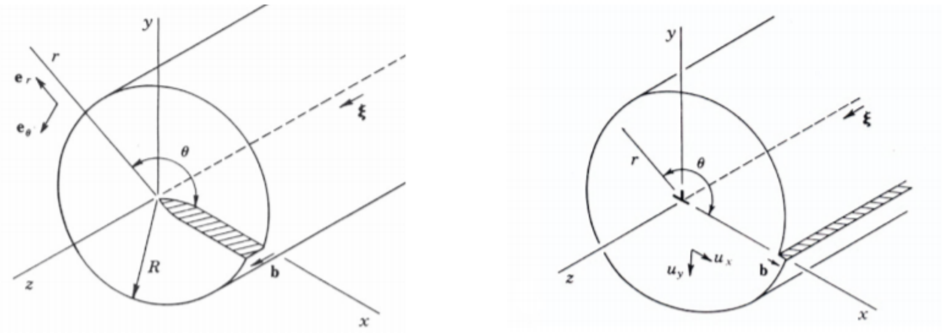

(a) Dislocation vis

(b) Dislocation coin

Figure A.5: Representation of a screw (left) and an edge (right) dislocation [HIR 83].

This edge dislocation will cause a shear stress field but also a compression [HIR 83]:

$$\sigma = \begin{bmatrix} \frac{\mu b \sin\theta}{2\pi(1-\nu)r} & \frac{\mu b \cos\theta}{2\pi(1-\nu)r} & 0 \\ \frac{\mu b \cos\theta}{2\pi(1-\nu)r} & \frac{\mu b \sin\theta}{2\pi(1-\nu)r} & 0 \\ 0 & 0 & \frac{\mu b \sin\theta}{\pi(1-\nu)r} \end{bmatrix} ; \sigma_{\theta z} = \frac{\mu b}{2\pi r} \tag{A.4}$$

With ν is the Poisson's ratio.

The total energy W of a dislocation is related to the generated stress field. The energy W per unit volume due to the linear elastic deformation can be calculated as follows:

For the shearing part:

$$W = \frac{\sigma^2}{2\mu} \tag{A.5}$$

For the compression part:

$$W = \frac{\sigma^2}{2E} \tag{A.6}$$

With E the Young's modulus.

Generally, the energy varies between 0.1 and $0.05\mu b$ [HIR 83] for a compact structure. Therefore, the energy per unit of length of a screw dislocation in a region limited by the dislocation core r_0 and the radius R of the cylinder is equal to:

$$\frac{W}{L} = \int_{r_0}^{R} \frac{\sigma_{\theta r^2}}{2\mu} 2\pi r \, dr = \frac{\mu b^2}{4\pi} \ln \frac{R}{r_0} \tag{A.7}$$

We can see that the energy diverges when R converges towards ∞, or when r_0 converges towards zero. The divergence due to R shows that we cannot attribute a characteristic energy to a dislocation because it depends on the size of the crystal. However, for a crystal containing several dislocations of opposite signs, we can approximate R being half the distance between two dislocations. Indeed, the logarithm shows that the choice of R has a very little influence on the energy's value.

In the case of an edge dislocation, the energy's form is:

$$\frac{W}{L} = \int_{r_0}^{R} r\,dr \int_{2\pi}^{0} d\theta \left[\frac{1}{2\mu}\sigma_{r\theta}^2 + \frac{1}{2E}(\sigma_{rr}^2 + \sigma_{\theta\theta}^2 + \sigma_{zz}^2)\right] = \frac{\mu b^2}{4\pi(1-\nu)} \ln\frac{R}{r_0} \tag{A.8}$$

This is similar to the case of a screw dislocation, with an additional $\frac{1}{1-\nu}$ term.

A.2 Link between dislocations and mechanical properties

Each dislocation has one or more slip planes. The slip plane is the plane containing both $\vec{b}$ and $\vec{u}$. For screw dislocation, there are several slip planes, whereas for edge dislocations only one slip plane is possible. It is in this plane that the dislocation can move when an external stress is applied.

When an external stress noted σ' is applied, the dislocations are subjected to a normal force F per unit of length, and defined by the law of Peach and Koelher [FRI 64]:

$$F = (\overline{\overline{\sigma'}}.\vec{b}) \wedge \frac{\vec{u}}{u} \tag{A.9}$$

This force F will allow the dislocations to move in the material and to shear it (illustrated in Figure A.2). As the dislocation moves through the crystal, the atomic rows move from their original position (before deformation) to their new position (after displacement). These two positions, before and after deformation, are two stable states. During deformation, the atomic row goes through a state of higher energy that will oppose the movement. It corresponds to a braking force, also called a lattice friction. This force is the “Peierls-Nabarro‘’ stress.

The Peierls-Nabarro stress depends on the size of the dislocation core. If the deformation is concentrated in a monoatomic line, during the displacement, all the atoms on the line will undergo an important displacement, which requires a significant amount of energy. However, if the core is spread out over several atomic rows, when the dislocation advances one atomic row, the atoms in the row will undergo a smaller displacement, and they will need less energy.

The dislocations will slide in sliding planes that allow the dislocation to spread easily and thus minimize the frictional force. The sliding will follow dense directions (small distance between two successive atoms) to minimize the energy required for deformation. This sliding plane and this direction define what is called a slip system.

We can predict which slip plane will be activated according to the projected component τ of the force F on each of the planes. The active slip system will generally be the one with the highest value of τ (called main slip system). We write the component τ (with the notations of the Figure A.6) as:

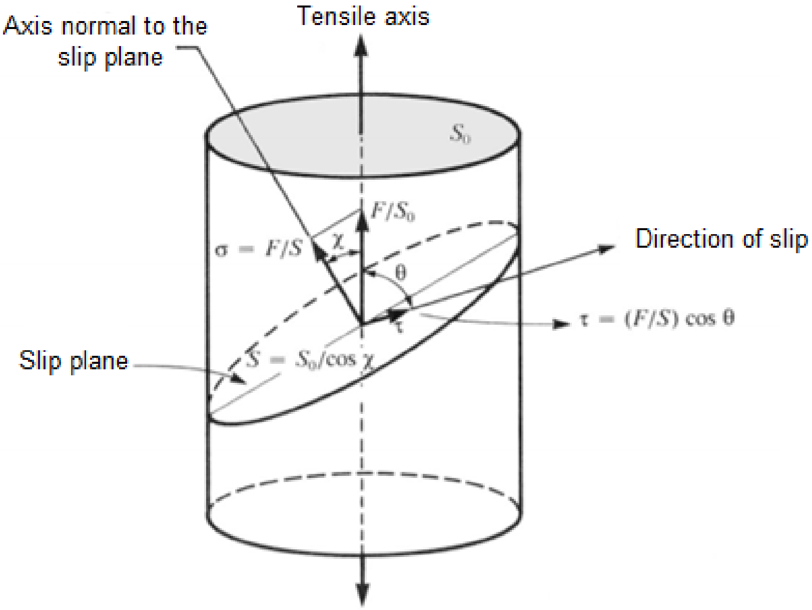

Figure A.6: Schmid's law. Projection of the traction force applied on a slip plane (with a resolved split in a sliding direction) [HAU 89].

S_0 is the surface of the sample, θ the angle between the direction of the stressing force F and the slip plane considered and the angle between the stressing force F and the normal to the slip plane.

The Schmid factor is the term $cos\theta cos\chi$ for the plane system that we are considering. With the equation (A.9), we can calculate the necessary macroscopic stress to activate the desired slip system as a function of the angle of application of the external force F. We can also see that the movement of the dislocations in their slip plane will not be collinear with the applied force (except in special cases) and it shows that the plastic deformation is anisotropic.

The applied force and the associated stress to move into the plastic domain is modeled by the Von Mises criterion. This criterion does not consider hydrostatic stresses and only considers plastic deformation. The plastic domain is defined as:

$$f(\sigma) = \sigma_{VM} - \sigma_c > 0 \tag{A.10}$$

σ_{VM} is the equivalent stress in the sense of Von Mises and σ_c is the material's elastic limit (Figure A.1). The equivalent constraint in the sense of Von Mises is :

$$\sigma_{VM} = \sqrt{[(\sigma_1 - \sigma_2)^2 + (\sigma_2 - \sigma_3)^2 + (\sigma_3 - \sigma_1)^2]} \tag{A.11}$$

σ_1, σ_2 and σ_3 are the principal stresses, in the principal coordinate system, the orthonormal coordinate system where the stress tensor is diagonalized.

The elastic limit σ_c is not a fixed value. It will depend on the history of the material and on its microstructure. For example, during a tensile test, we can determine the elastic behavior of a material and the evolution of this limit. The purpose of this test is to measure the elongation of the material, as a function of the applied force and to convert these measurements into deformation and stress.

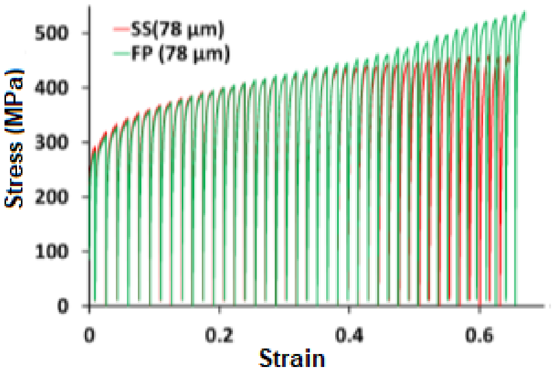

Figure A.7: Tensile test cycle at constant temperature and strain rate, for two samples of nickel-based alloy put under Solid Solution (SS) and with Fully Precipitates (FP) [BLA 16].

If we conduct several tensile tests on the same sample, we can see that its elastic limit increases with the number of cycles (see Figure A.7). This phenomenon is due to the hardening of the material (or work hardening). The hardening is due to the difficulty of deforming the material because of dislocations that locks one another: the more the stress increases to continue to deform the material the more the hardening is important. This phenomenon depends on the previous deformation state of the material when the stress is applied.

Appendix B

Electronic diffraction

B.1 Notion of diffraction

To understand the imagery TEM dislocations, it is necessary to know about the geometry of the perfect crystal and its property. The perfect crystal is defined by a vector $\vec{r} = u.\vec{a} + v.\vec{b} + w.\vec{c}$ located in an orthonormal reference $\vec{a}$, $\vec{b}$ and $\vec{c}$, which forms the direct lattice (see Figure B.1).

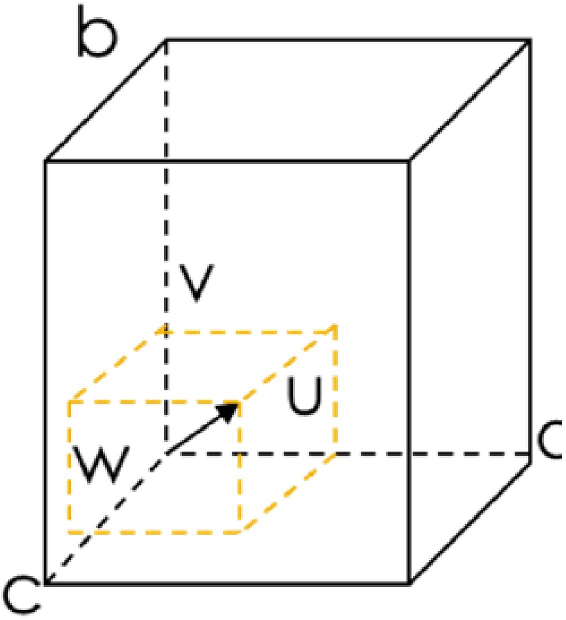

Figure B.1: Perfect crystal.

When an incident wave interacts with a crystal, the diffracted waves by a plane family (hkl) will enter into constructive or destructive interference, according to their phase shift related to the path difference δ.

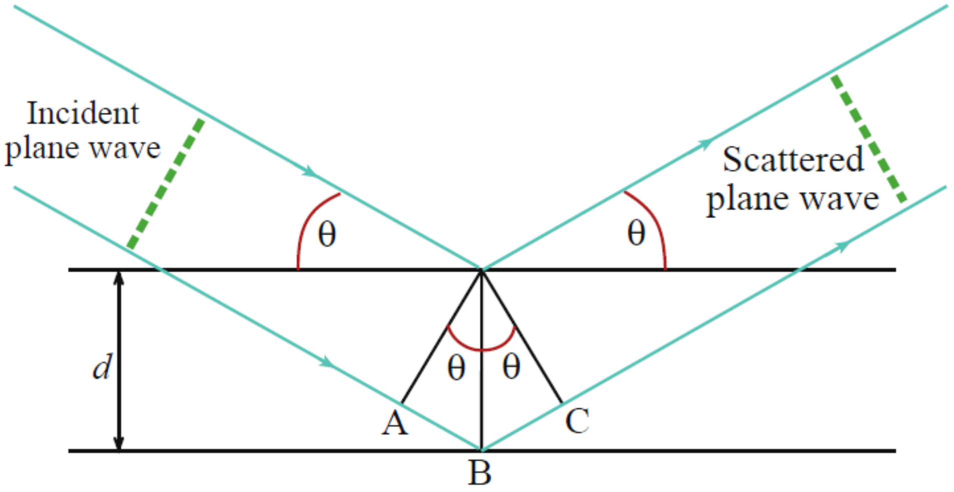

Figure B.2: The Bragg description of diffraction in terms of the reflection of a plane wave (wavelength) incident at an angle to atomic planes of spacing d [CAR 16].

The phase shift φ is defined as:

$$\varphi = \frac{2\pi\delta}{\lambda} = \frac{2\pi}{\lambda}\vec{r}(\vec{I} - \vec{I_0}) \tag{B.1}$$

$\vec{I}$ is the direction of the total wave (scattered) and $\vec{I_0}$ the directing vector of the incident wave.

To know how the planes of a crystal will diffract we need the distance d_{hkl} between crystalline planes, which composes it because our path difference δ is proportional to this distance. In addition, in order to demonstrate the diffraction of a crystal lattice easily, we cannot use the direct lattice. This is due to the fact that a plane is defined by its normal and that the normal to a plane (hkl) is not $h.\vec{a} + k.\vec{b} + l.\vec{c}$. This is why we use the reciprocal lattice (or “dual” lattice in mathematics), which is also called the “normal to the plan” lattice. The use of the reciprocal lattice is also justified by the fact that the immediately accessible information is normal to the plan and not the directions (direct lattice).

The reciprocal lattice is a difficult mathematical concept. It corresponds to a point lattice, like the direct lattice. However, this is not an atomic site but an association of planes in the crystal. Although it is more abstract, the reciprocal lattice is just as real as the direct lattice.

We can write any vector $\vec{r*}$ of the reciprocal lattice as:

$$\vec{r^*} = n_1\vec{a^*} + n_2\vec{b^*} + n_3\vec{c^*} \tag{B.2}$$

$\vec{a^*}$, $\vec{b^*}$ and $\vec{c^*}$ are the basic vectors of the reciprocal lattice. Their directions are defined by the following relationships:

$$\vec{a^*}\vec{b} = \vec{a^*}\vec{c} = \vec{b^*}\vec{c} = \vec{b^*}\vec{a} = \vec{c^*}\vec{a} = \vec{c^*}\vec{b} = 0; \tag{B.3}$$

This means that, for example, $\vec{a^*}$ is in a normal direction to $\vec{b}$ and $\vec{c}$. Their lengths are defined by the following relationships:

$$\vec{a^*}\vec{a} = 1; \vec{b^*}\vec{b} = 1; \vec{c^*}\vec{c} = 1; \tag{B.4}$$

The reciprocal lattice is similar to a phase space also called wave vectors. This space, although abstract, is very useful because the wave vectors have the specificity of being the eigenvectors of the different linear and homogeneous transformations. In our case, it allows us to have access to the normal plan.

A simple way to obtain the diffraction condition is $\|\vec{g}\| = \frac{\delta}{\lambda} = 2\frac{sin\theta}{\lambda}$ and we can rewrite φ as:

$$\varphi = 2\pi\vec{r}.\vec{g} \tag{B.5}$$

With $\vec{r}$ is the vector of the direct lattice between atoms A and B.

For the diffracted wave to be in constructive interference, the phase shift must follow some conditions called "Laue conditions":

$$\vec{a}.\vec{g} = h \ , \ \vec{b}.\vec{g} = k \ , \ \vec{c}.\vec{g} = l \text{ with } h, k, l \text{ integer} \tag{B.6}$$

By definition, in Laue's conditions, $\vec{g}$ is a vector of the reciprocal lattice. We can then write:

$$\|\vec{g}\| = \| \ h.\vec{a^*} + k.\vec{b^*} + l.\vec{c^*}\| = \frac{1}{d_{hkl}} \tag{B.7}$$

This gives us the diffraction conditions of Bragg (Bragg's law) [CAR 16]:

$$2d_{hkl}\sin\theta = \lambda \tag{B.8}$$

For a clearer visualization of the diffraction phenomenon, we use the Ewald Sphere [EWA 62](Figure B.3), this representation is purely visual and has no physical meaning:

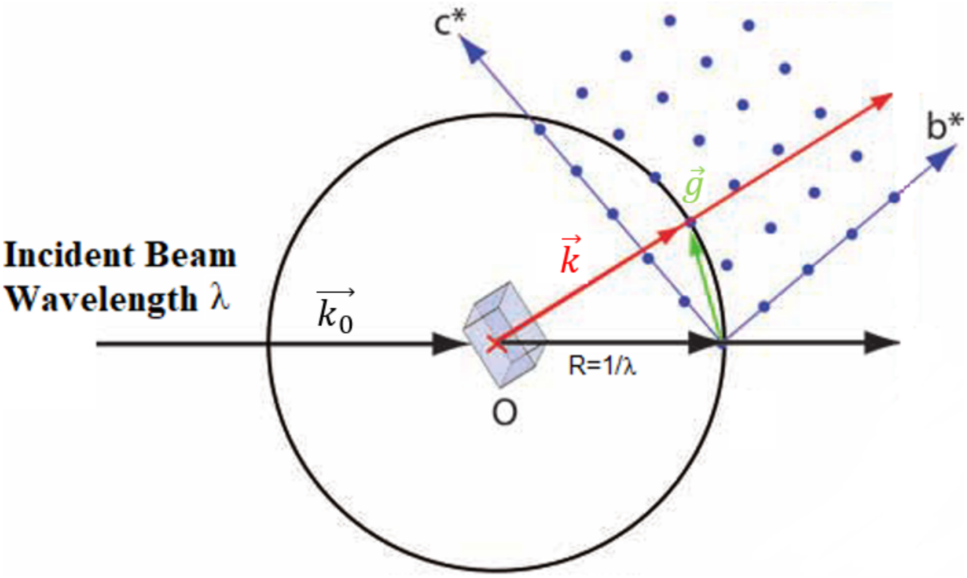

Figure B.3: Diagrame of the Ewald sphere [?].

The Ewald sphere is defined as a circle of radius $1/\lambda$ (with λ the wavelength of the incident beam), centered on the crystal which is crossed by the incident beam.

We can thus define $\vec{g}$ as the diffracting vector:

$$\vec{g} = \frac{\vec{k} - \vec{k_0}}{\lambda} \tag{B.9}$$

With $\vec{k}$ is the directing vector of the diffracted wave and $\vec{k_0}$ the directing vector of incident wave.

In this configuration, there is diffraction when the three Laue conditions are respected (equations(B.6)) and that means when the Ewald sphere cuts the reciprocal lattice at a point, as in the case on the Figure B.3.

B.2 Notion of Bragg deviation

Ewald's sphere describes a perfect situation, with an infinite crystal. In these conditions, we will have a diffraction of the crystalline planes only if the end of the diffracting vector g `[U+20D7]` touches a point of the reciprocal lattice, which makes this event rare. However, the observable samples with TEM (thin blade) have a thickness of 100 nm or so. This thickness in the electron beam makes the nodes of reciprocal lattice relrods:

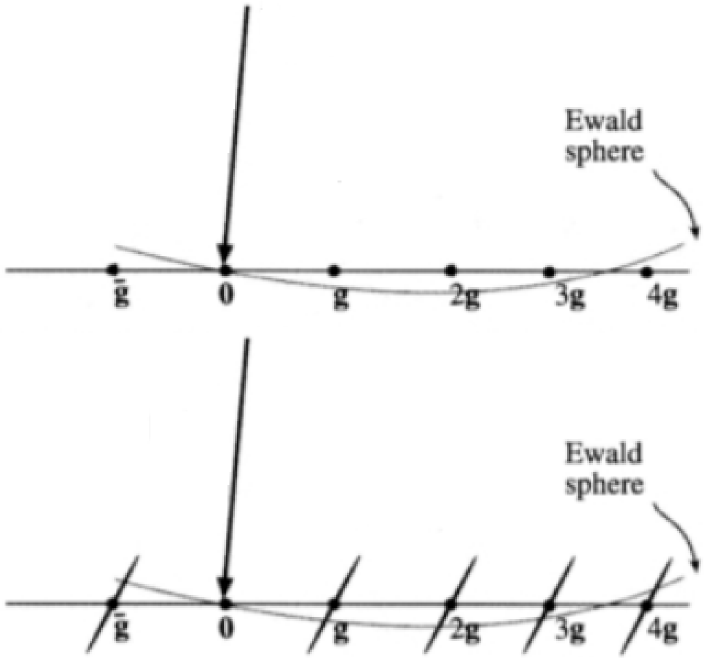

Figure B.4: Ewald sphere of an infinite crystal (up) and of a thin blade (bottom) [CAR 16] .

We can see that, in the infinite crystal, the sphere passes through no node of the lattice. However, for the thin blade, the sphere passes through several relrolds. There is a greater probability of cutting a node of the reciprocal lattice with the Ewald sphere and therefore a greater probability of being in diffraction conditions even if we do not respect the Bragg angle(B.8). This phenomenon is called the relaxation of Bragg conditions.

It is important to note that the diffracted intensity depends on where the Ewald sphere cuts the relrods. The deviation from the exact Bragg conditions can be represented by a deviation vector $\vec{s}$, which connects the center of the relrod to the Ewald sphere.

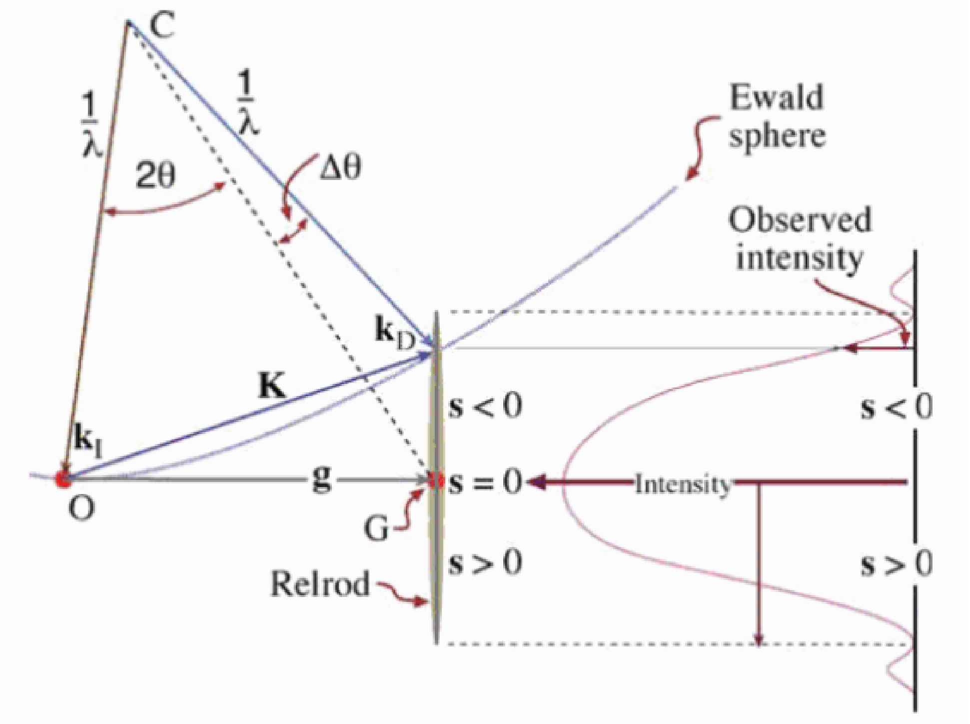

Figure B.5: Diffracted intensity as a function of the Bragg deviation vector s [CAR 16].

In Laue's conditions, the diffraction of a plane family (hkl) is possible if $\vec{g_{hkl}} = \vec{k_D} - \vec{k_0}$, but for a thin section we will then have to take into account the correction $\vec{s}$. The new diffraction conditions are:

$$\vec{g_{hkl}} + \vec{s} = \vec{K_D} - \vec{k_0} \tag{B.10}$$

In Figure B.5, the diffracted intensity will be greater when $\vec{s}$ tends to zero.

B.3 Diffraction in TEM

It is important to clarify the role of one of the electromagnetic lenses contained in the microscope (which has the same properties as a conventional optical lens), the objective lens that is located after the sample. This lens has two functions. The first is to make an enlarged image of the object. In Figure B.6, the beams parallel to the optical axis emitted by points A_0, A_1 and A_2 on the object will cross at the image focus point of the lens, before forming a magnified image on the image plane of the lens.

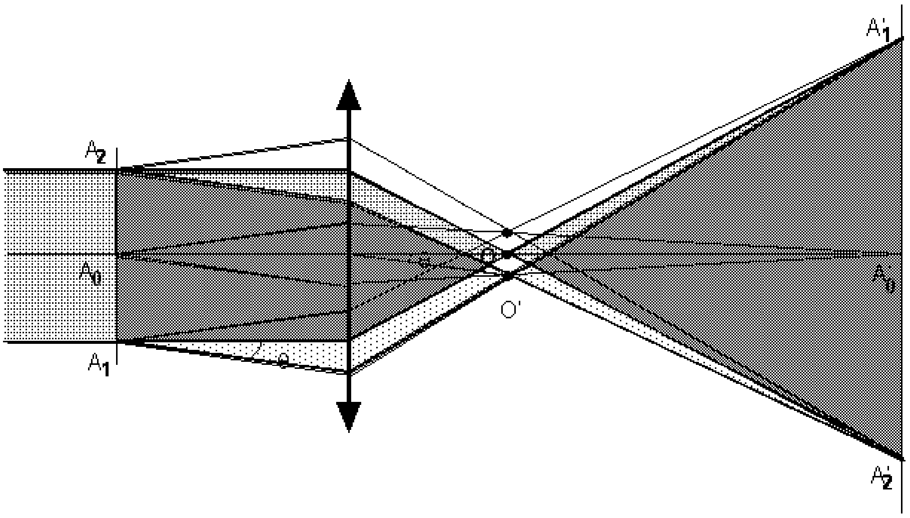

Figure B.6: Diagram of operation of the obejctive lens.

The different beams emitted by the points A_0, A_1 and A_2 which are deflected by an angle θ with respect to the parallel beams will focus on a point O' different from the point O but always in the same focal plane, before forming the same image in the image plane as the beams which are not deflected. It is easy to see that, in the focal plane of the lens, it is possible to distinguish the different trajectories of the beams that pass through it with different angles θ. By placing a screen in the focal plane of the lens, it is then possible to observe a diffraction pattern:

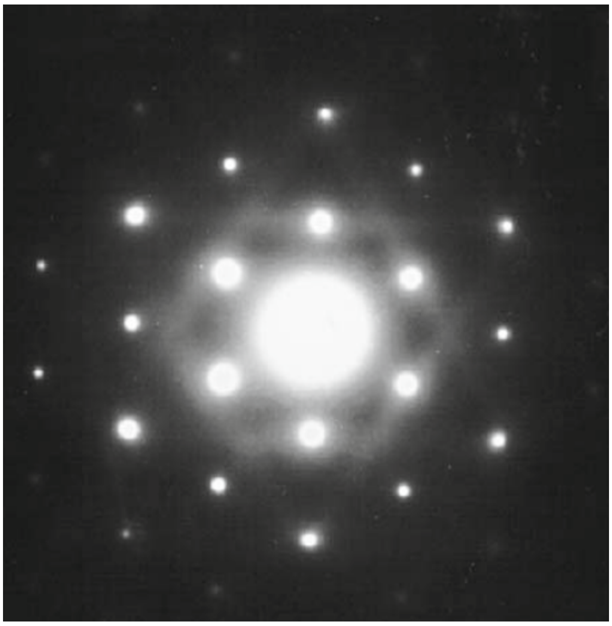

Figure B.7: Example of diffraction plates obtained on a single-crystal sample Aluminium [CAR 16] .

The sample will emit several types of beam. The beams that are emitted parallel to the optical axis will meet to form the central spot, later called the transmissive spot. But part of the beam arriving on the sample will be diffracted by the different crystal planes. These crystalline planes will deflect the incident beam from a different angle θ resulting in several diffraction spots in the focal plane of the lens.

It is then important to understand, from this diffraction picture, how the crystal has diffracted, in order to be able to link the observation of a dislocation type defect to its sliding system but also to be able to orientate itself.

Each spot corresponds to a different diffraction condition (Bragg condition) that is allowed to the electrons leaving the sample. As a reminder, the diffraction plane is a map of the directions normal to the diffraction plane, it is then possible to relate the distance separating the central spot to a spot by the diffraction vector $\vec{g_{hkl}}$ associated with the (hkl) planes in diffraction condition. Many software programs (JEMS, Electron diffraction, etc) allow to index diffraction plates in this way.

References

[ALL 12] Allain S., Bouaziz O., Takahashi M.
Toward a new interpretation of the mechanical behaviour of as-quenched low alloyed martensitic steels. vol. 52, n° 4, 2012, p. 717–722. ISBN: 0915-1559 Publisher: The Iron and Steel Institute of Japan.

[ALL 15] Allain S. Y. P., Bouaziz O., Pushkareva I., Scott C. P.
Towards the microstructure design of DP steels: A generic size-sensitive mean-field mechanical model. vol. 637, 2015, p. 222–234. ISBN: 0921-5093 Publisher: Elsevier.

[ASH 70] Ashby M. F.
The deformation of plastically non-homogeneous materials. vol. 21, n° 170, 1970, p. 399–424. ISBN: 0031-8086 Publisher: Taylor & Francis.

[BAB 13] Babu B., Lindgren L.-E.
Dislocation density based model for plastic deformation and globularization of Ti-6Al-4V. vol. 50, 2013, p. 94–108. ISBN: 0749-6419 Publisher: Elsevier.

[BAR 06] Barnard J., Sharp J., Tong J., Midgley P.
High-resolution three-dimensional imaging of dislocations. *Science*, vol. 313, n° 5785, 2006, p. 319–319, American Association for the Advancement of Science.

[BAR 14] Bardel D.
Rôle de la microstructure d'un alliage à durcissement structural sur son comportement et sa tenue mécanique sous sollicitations cycliques après un transitoire thermique. , 2014.

[BEA 17] Beausir B., Fundenberger J. J.
Analysis Tools for Electron and X-ray diffraction. , 2017.

[BET 28] Bethe H.
Theorie der beugung von elektronen an kristallen. vol. 392, n° 17, 1928, p. 55–129. ISBN: 0003-3804 Publisher: Wiley Online Library.

[BIS 11] Bissey-Breton S., Gravier J., Vignal V.
Impact of superfinish turning on surface integrity of pure copper. vol. 19, 2011, p. 28–33. ISBN: 1877-7058 Publisher: Elsevier.

[BLA 16] Blaizot J.
Etude de l'influence des procédés de fabrication sur les propriétés mécaniques des alliages de nickel. , 2016.

[BOR 00] Borbély A., Driver J., Ungár T.
An X-ray method for the determination of stored energies in texture components of deformed metals; application to cold worked ultra high purity iron. *Acta materialia*, vol. 48, n° 8, 2000, p. 2005–2016, Elsevier.

[BOU 02] Bouaziz O., Buessler P.
Mechanical behaviour of multiphase materials: an intermediate mixture law without fitting parameter. vol. 99, n° 1, 2002, p. 71–77. ISBN: 0035-1563 Publisher: EDP Sciences.

[BOU 08] Bouaziz O., Aouafi A., Allain S.
Effect of grain refinement on the mechanical behaviour of ferritic steels: Evolution of isotropic hardening and kinematic hardening. *Materials Science Forum*, vol. 584 Trans Tech Publ, 2008, p. 605–609.

[BRA 70a] Brandon D. G., Komem Y.
Quantitative analysis of dislocation distributions. vol. 3, n° 1, 1970, p. 111–126.

[BRA 70b] Brandon D. G., Komem Y.
Quantitative analysis of dislocation distributions. vol. 3, n° 1, 1970, p. 111–126. ISBN: 0026-0800 Publisher: Elsevier.

[CAG 58] Caglioti G., Paoletti A. t., Ricci F. P.
Choice of collimators for a crystal spectrometer for neutron diffraction. vol. 3, n° 4, 1958, p. 223–228. ISBN: 0369-643X Publisher: Elsevier.

[CAL 20] Callister Jr W. D., Rethwisch D. G.
Callister's materials science and engineering. John Wiley & Sons, 2020.

[CAR 16] Carter C. B., Williams D. B.
Transmission electron microscopy: Diffraction, imaging, and spectrometry. Springer, 2016.

[CAZ 19] Cazottes S., Bechis A., Lafond C., L'hôte G., Roth C., Dreyfus T., Steyer P., Douillard T., Langlois C.
Toward an automated tool for dislocation density characterization in a scanning electron microscope. vol. 158, 2019, Page 109954. ISBN: 1044-5803 Publisher: Elsevier.

[CHE 96] Chen M.-S., Han J., Yu P. S.
Data mining: an overview from a database perspective. vol. 8, n° 6, 1996, p. 866–883. ISBN: 1041-4347 Publisher: IEEE.

[CHE 15] Chen Y.-H., Park S. U., Wei D., Newstadt G., Jackson M., Simmons J. P., De Graef M., Hero A. O.
A Dictionary Approach to EBSD Indexing. *arXiv preprint arXiv:1502.07436*, , 2015.

[CLA 71] Clarke D. R., Howie A.
Calculations of lattice defect images for scanning electron microscopy. vol. 24, n° 190, 1971, p. 959–971. ISBN: 0031-8086 Publisher: Taylor & Francis.

[COA 67] Coates D.
Kikuchi-like reflection patterns obtained with the scanning electron microscope. *The Philosophical Magazine: A Journal of Theoretical Experimental and Applied Physics*, vol. 16, n° 144, 1967, p. 1179–1184, Taylor & Francis.

[COC 69] Cockayne D. J. H., Ray I. L. F., Whelan M. J.
Investigations of dislocation strain fields using weak beams. vol. 20, n° 168, 1969, p. 1265–1270. ISBN: 0031-8086 Publisher: Taylor & Francis.

[COT 64] Cottrell A. H.
The mechanical properties of matter. , 1964.

[DEC 09] De Carvalho F. d. A. T., Lechevallier Y.
Partitional clustering algorithms for symbolic interval data based on single adaptive distances. vol. 42, n° 7, 2009, p. 1223–1236.

[DEL 01] Delille D., Pantel R., Van Cappellen E.
Crystal thickness and extinction distance determination using energy filtered CBED pattern intensity measurement and dynamical diffraction theory fitting. vol. 87, n° 1, 2001, p. 5–18. ISBN: 0304-3991 Publisher: Elsevier.

[DEL 07] Delincé M., Bréchet Y., Embury J. D., Geers M. G. D., Jacques P. J., Pardoen T.
Structure–property optimization of ultrafine-grained dual-phase steels using a microstructure-based strain hardening model. vol. 55, n° 7, 2007, p. 2337–2350. ISBN: 1359-6454 Publisher: Elsevier.

[DHI 22] Dhinwal S. S., Ernould C., Beausir B.
Facilitating the occurrence of dynamic recrystallization in plain extra low-carbon steel by warm asymmetric rolling. *Materials Characterization*, vol. 189, 2022, Page 111942, Elsevier.

[DID 13] Diday E., Lechevallier Y., Schader M., Bertrand P., Burtschy B.
New Approaches in Classification and Data Analysis. Springer Science & Business Media, 2013. Google-Books-ID: CH7yCAAAQBAJ.

[DIN 10] Dini G., Ueji R., Najafizadeh A., Monir-Vaghefi S. M.
Flow stress analysis of TWIP steel via the XRD measurement of dislocation density. vol. 527, n° 10, 2010, p. 2759–2763. ISBN: 0921-5093 Publisher: Elsevier.

[DUD 95] Dudarev S. L., Rez P., Whelan M. J.
Theory of electron backscattering from crystals. vol. 51, n° 6, 1995, Page 3397. Publisher: APS.

[ELD 03] El-Dasher B. S., Adams B. L., Rollett A. D.
Experimental recovery of geometrically necessary dislocation density in polycrystals. vol. 48, n° 2, 2003, p. 141–145. ISBN: 1359-6462 Publisher: Elsevier.

[ERN 20a] Ernould C., Beausir B., Fundenberger J.-J., Taupin V., Bouzy E.
Characterization at high spatial and angular resolutions of deformed nanostructures by on-axis HR-TKD. *Scripta Materialia*, vol. 185, 2020, p. 30–35, Elsevier.

[ERN 20b] Ernould C., Beausir B., Fundenberger J.-J., Taupin V., Bouzy E.
Global DIC approach guided by a cross-correlation based initial guess for HR-EBSD and on-axis HR-TKD. vol. 191, 2020, p. 131–148.

[ERN 21] Ernould C., Beausir B., Fundenberger J.-J., Taupin V., Bouzy E.
Integrated correction of optical distortions for global HR-EBSD techniques. *Ultramicroscopy*, vol. 221, 2021, Page 113158, Elsevier.

[EST 84] Estrin Y., Mecking H.
A unified phenomenological description of work hardening and creep based on one-parameter models. vol. 32, n° 1, 1984, p. 57–70. ISBN: 0001-6160 Publisher: Elsevier.

[EST 96] Estrin Y.
Dislocation-density-related constitutive modeling. vol. 1, 1996, p. 69–106. Publisher: Academic Press San Diego, CA.

[EWA 62] Ewald P.
Fifty Years of X-Ray Diffraction Dedicated to the International Union of Crystallography on the Occasion of the Commemoration Meeting in Munich July 1962. , 1962, Springer.

[FAR 08] Farooq M. U., Villaurrutia R., MacLaren I., Kungl H., Hoffmann M. J., FUNDENBERGER J.-J., Bouzy E.

Using EBSD and TEM[U+2010]Kikuchi patterns to study local crystallography at the domain boundaries of lead zirconate titanate. vol. 230, n° 3, 2008, p. 445–454. ISBN: 0022-2720 Publisher: Wiley Online Library.

[FIE 10] Field D. P., Magid K. R., Mastorakos I. N., Florando J. N., Lassila D. H., Morris Jr J. W.
Mesoscale strain measurement in deformed crystals: A comparison of X-ray microdiffraction with electron backscatter diffraction. vol. 90, n° 11, 2010, p. 1451–1464. ISBN: 1478-6435 Publisher: Taylor & Francis.

[FOL 22] Foley D. L., Latypov M. I., Zhao X., Hestroffer J., Beyerlein I. J., Lamberson L. E., Taheri M. L.
Geometrically necessary dislocation density evolution as a function of microstructure and strain rate. vol. 831, 2022, Page 142224. ISBN: 0921-5093 Publisher: Elsevier.

[FRA 50] Frank F. C., Read Jr W. T.
Multiplication processes for slow moving dislocations. vol. 79, n° 4, 1950, Page 722. Publisher: APS.

[FRE 26] Frenkel J.
Zur theorie der elastizitätsgrenze und der festigkeit kristallinischer körper. *Zeitschrift für Physik*, vol. 37, n° 7, 1926, p. 572–609, Springer.

[FRE 18] Fressengeas C., Beausir B., Kerisit C., Helbert A.-L., Baudin T., Brisset F., Mathon M.-H., Besnard R., Bozzolo N.
On the evaluation of dislocation densities in pure tantalum from EBSD orientation data. *Matériaux & Techniques*, vol. 106, n° 6, 2018, Page 604, EDP Sciences.

[FRI 64] Friedel J.
Dislocations Pergamon Press. *New York*, , 1964.

[GAL 22] Gallet J., Perez M., Dubail S., Chaise T., Douillard T., Langlois C., Cazottes S.
About the automatic measurement of the dislocation density obtained by R-ECCI. , 2022, Page 112358.

[GRA 19] Graef M. D., Jackson M., Saransh13 W., Kleingers J., Wright S.
Josephtessmer. Emsoft-org/emsoft: Release 4.2 to synchronize with di tutorial paper (2019). 2019.

[GUB 16] Gubicza J., El-Tahawy M., Huang Y., Choi H., Choe H., Lábár J. L., Langdon T. G.
Microstructure, phase composition and hardness evolution in 316L stainless steel processed by high-pressure torsion. vol. 657, 2016, p. 215–223. ISBN: 0921-5093 Publisher: Elsevier.

[GUT 09] Gutierrez-Urrutia I., Zaefferer S., Raabe D.
Electron channeling contrast imaging of twins and dislocations in twinning-induced plasticity steels under controlled diffraction conditions in a scanning electron microscope. vol. 61, n° 7, 2009, p. 737–740. ISBN: 1359-6462 Publisher: Pergamon.

[GUT 12] Gutierrez-Urrutia I., Raabe D.
Dislocation density measurement by electron channeling contrast imaging in a scanning electron microscope. vol. 66, n° 6, 2012, p. 343–346. ISBN: 1359-6462 Publisher: Pergamon.

[HAL 51a] Hall E. O.
The deformation and ageing of mild steel: II characteristics of the Lüders deformation. vol. 64,

n° 9, 1951, Page 742. ISBN: 0370-1301 Publisher: IOP Publishing.

[HAL 51b] Hall E. O.
The deformation and ageing of mild steel: III discussion of results. vol. 64, n° 9, 1951, Page 747. ISBN: 0370-1301 Publisher: IOP Publishing.

[HAM 61] Ham R.
The determination of dislocation densities in thin films. *Philosophical Magazine*, vol. 6, n° 69, 1961, p. 1183–1184, Taylor & Francis.

[HAN 21] Han J.-K., Liu X., Lee I., Kuzminova Y. O., Evlashin S. A., Liss K.-D., Kawasaki M.
Structural evolution during nanostructuring of additive manufactured 316L stainless steel by high-pressure torsion. vol. 302, 2021, Page 130364. ISBN: 0167-577X Publisher: Elsevier.

[HAU 89] Haudin J.-M., Montheillet F.
Notions fondamentales sur les matériaux: déformation plastique et essais mécaniques: cours du certificat d'études supérieures de technologie des matériaux employés en art dentaire de l'Université de Nice... Ed. SNPMD, 1989.

[HE 14] He B. B., Zhu K., Huang M. X.
On the nanoindentation behaviour of complex ferritic phases. vol. 94, n° 7, 2014, p. 439–446. ISBN: 0950-0839 Publisher: Taylor & Francis.

[HIR 62] Hirsch P., Howie A., Whelan M.
On the production of X-rays in thin metal foils. *Philosophical Magazine*, vol. 7, n° 84, 1962, p. 2095–2100, Taylor & Francis.

[HIR 70] Hirsch P. B., Humphreys F. J.
The deformation of single crystals of copper and copper-zinc alloys containing alumina particles-I. Macroscopic properties and workhardening theory. vol. 318, n° 1532, 1970, p. 45–72. ISBN: 0080-4630 Publisher: The Royal Society London.

[HIR 83] Hirth J. P., Lothe J., Mura T.
Theory of dislocations. *Journal of Applied Mechanics*, vol. 50, n° 2, 1983, Page 476.

[HIT 14] Hite J. K., Gaddipati P., Meyer D. J., Mastro M. A., Jr C. R. E.
Correlation of threading screw dislocation density to GaN 2-DEG mobility. vol. 50, n° 23, 2014, p. 1722–1724. Publisher: IET Digital Library.

[HON 17] Honglong S., Minting L., Wenzhong W.
CBED Tools for semi-automatic measurement of crystal thicknesses. vol. 50, n° 1, 2017, p. 313–319. ISBN: 1600-5767 Publisher: International Union of Crystallography.

[HUA 98] Huang B.-P., Zheng Z.-Q.
Effects of Li content on precipitation in Al-Cu-(Li)-Mg-Ag-Zr alloys. vol. 38, n° 3, 1998, p. 357–362. ISBN: 1359-6462 Publisher: Elsevier.

[HUG 03] Hughes D. A., Hansen N., Bammann D. J.
Geometrically necessary boundaries, incidental dislocation boundaries and geometrically necessary dislocations. vol. 48, n° 2, 2003, p. 147–153. ISBN: 1359-6462 Publisher: Elsevier.

[HUT 18] Hutchinson B., Bate P., Lindell D., Malik A., Barnett M., Lynch P.
Plastic yielding in lath martensites–An alternative viewpoint. vol. 152, 2018, p. 239–247. ISBN: 1359-6454 Publisher: Elsevier.

[JAI 99] Jain A. K., Murty M. N., Flynn P. J.
Data clustering: a review. vol. 31, n° 3, 1999, p. 264–323.

[JAI 10] Jain A. K.
Data clustering: 50 years beyond K-means. vol. 31, n° 8, 2010, p. 651–666. ISBN: 0167-8655 Publisher: Elsevier.

[JIA 13] Jiang J., Britton T. B., Wilkinson A. J.
Measurement of geometrically necessary dislocation density with high resolution electron backscatter diffraction: effects of detector binning and step size. vol. 125, 2013, p. 1–9. ISBN: 0304-3991 Publisher: Elsevier.

[JOY 82] Joy D. C., Newbury D. E., Davidson D. L.
Electron channeling patterns in the scanning electron microscope. vol. 53, n° 8, 1982, p. R81–R122. ISBN: 0021-8979 Publisher: American Institute of Physics.

[Já 18] Jácome L. A., Pöthkow K., Paetsch O., Hege H.-C.
Three-dimensional reconstruction and quantification of dislocation substructures from transmission electron microscopy stereo pairs. vol. 195, 2018, p. 157–170. ISBN: 0304-3991 Publisher: Elsevier.

[KAC 91] Kaczorowski M., Gerberich W. W.
On the sensitivity of electron channelling line shapes to dislocation distribution. vol. 26, n° 7, 1991, p. 1910–1918. ISBN: 1573-4803 Publisher: Springer.

[KAL 20] Kalácska S., Dankházi Z., Zilahi G., Maeder X., Michler J., Ispánovity P. D., Groma I.
Investigation of geometrically necessary dislocation structures in compressed Cu micropillars by 3-dimensional HR-EBSD. *Materials Science and Engineering: A*, vol. 770, 2020, Page 138499, Elsevier.

[KHA 20] Khatami-Hamedani H., Zarei-Hanzaki A., Abedi H. R., Anoushe A. S., Karjalainen L. P.
Dynamic restoration of the ferrite and austenite phases during hot compressive deformation of a lean duplex stainless steel. vol. 788, 2020, Page 139400. ISBN: 0921-5093 Publisher: Elsevier.

[KOC 03] Kocks U. F., Mecking H.
Physics and phenomenology of strain hardening: the FCC case. vol. 48, n° 3, 2003, p. 171–273. ISBN: 0079-6425 Publisher: Pergamon.

[KOH 20] Kohnert A. A., Tummala H., Lebensohn R. A., Tomé C. N., Capolungo L.
On the use of transmission electron microscopy to quantify dislocation densities in bulk metals. vol. 178, 2020, p. 161–165. ISBN: 1359-6462 Publisher: Elsevier.

[KOS 39] Kossel W., Möllenstedt G.
Elektroneninterferenzen im konvergenten Bündel. *Annalen der Physik*, vol. 428, n° 2, 1939, p. 113–140, Wiley Online Library.

[KRI 17] Kriaa H., Guitton A., Maloufi N.
Fundamental and experimental aspects of diffraction for characterizing dislocations by electron channeling contrast imaging in scanning electron microscope. vol. 7, n° 1, 2017, Page 9742.

[KRI 18] Kriaa H., Guitton A., Maloufi N.
Fundamental and experimental aspects of diffraction for characterizing dislocations on bulk materials by electron channeling contrast imaging in scanning electron microscope. , 2018. Published: MRS Fall Meeting & Exhibit.

[KRÖ 58] Kröner E.
Kontinuumstheorie der versetzungen und eigenspannungen, vol. 5. Springer, 1958.

[LAF 18] Lafond C., Douillard T., Cazottes S., Steyer P., Langlois C.
Electron CHanneling ORientation Determination (eCHORD): An original approach to crystalline orientation mapping. vol. 186, 2018, p. 146–149. ISBN: 0304-3991 Publisher: Elsevier.

[LAF 20] Lafond C.
Cartographie d'orientations cristallines à partir du contraste de canalisation en microscopie électronique à balayage. , 2020.

[LAF 21] Lafond C., Douillard T., Saad H., Deville S., Meille S., Steyer P., Cazottes S., Langlois C.
eCHORD orientation mapping of bio-inspired alumina down to 1 kV. vol. 20, 2021, Page 101207. ISBN: 2589-1529 Publisher: Elsevier.

[LAO 12] LAOUINI A.
. Réalisation d'un appareil de fluage des métaux, 2012.

[LEE 14] Lee D. J., Yoon E. Y., Ahn D.-H., Park B. H., Park H. W., Park L. J., Estrin Y., Kim H. S.
Dislocation density-based finite element analysis of large strain deformation behavior of copper under high-pressure torsion. vol. 76, 2014, p. 281–293. ISBN: 1359-6454 Publisher: Elsevier.

[L'H 19] L'hôte G., Lafond C., Steyer P., Deschanel S., Douillard T., Langlois C., Cazottes S.
Rotational-Electron Channeling Contrast Imaging analysis of dislocation structure in fatigued copper single crystal. vol. 162, 2019, p. 103–107. ISBN: 1359-6462 Publisher: Elsevier.

[LIE 02] Liedl U., Traint S., Werner E. A.
An unexpected feature of the stress–strain diagram of dual-phase steel. vol. 25, n° 1, 2002, p. 122–128. ISBN: 0927-0256 Publisher: Elsevier.

[LOU 83] Louër D., Auffrédic J. P., Langford J. I., Ciosmak D., Niepce J. C.
A precise determination of the shape, size and distribution of size of crystallites in zinc oxide by X-ray line-broadening analysis. vol. 16, n° 2, 1983, p. 183–191. ISBN: 1600-5767 Publisher: International Union of Crystallography.

[LUT 00] Lutterotti L.
Maud: a Rietveld analysis program designed for the internet and experiment integration. vol. 56, 2000, p. s54–s54.

[MAN 14] Mansour H., Guyon J., Crimp M. A., Gey N., Beausir B., Maloufi N.
Accurate electron channeling contrast analysis of dislocations in fine grained bulk materials. vol. 84, 2014, p. 11–14.

[MAN 15] Mansour H., Crimp M. A., Gey N., Maloufi N.
Characterization of a sub-grain boundary using Accurate Electron Channeling Contrast Imaging. vol. 21, 2015, p. 601–602. ISBN: 1431-9276 Publisher: Cambridge University Press.

[MAR 82] Marder A. R.
Deformation characteristics of dual-phase steels. vol. 13, n° 1, 1982, p. 85–92. ISBN: 1543-1940 Publisher: Springer.

[MAT 20] Mathevon A.
Caractérisation et modélisation des évolutions microstructurales et des propriétés mécaniques durant le traitement thermique d'aciers Dual-Phase. , 2020.

[MAT 21] Mathevon A., Fabrègue D., Massardier V., Cazottes S., Rocabois P., Perez M.
Investigation and mean-field modelling of microstructural mechanisms driving the tensile properties of dual-phase steels. *Materials Science and Engineering: A*, vol. 822, 2021, Page 141532.

[MEN 21] Meng Y., Ju X., Yang X.
The measurement of the dislocation density using TEM. vol. 175, 2021, Page 111065. ISBN: 1044-5803 Publisher: Elsevier.

[MES 10] Messerschmidt U.
Dislocation dynamics during plastic deformation, vol. 129. Springer Science & Business Media, 2010.

[MOU 15] Moussa C., Bernacki M., Besnard R., Bozzolo N.
About quantitative EBSD analysis of deformation and recovery substructures in pure Tantalum. *IOP Conference Series: Materials Science and Engineering*, vol. 89 IOP Publishing, 2015, Page 012038. Issue: 1.

[MUÑ 21] Muñoz J. A., Khelfa T., Komissarov A., Cabrera J.-M.
Ductility and plasticity of ferritic-pearlitic steel after severe plastic deformation. *Materials Science and Engineering: A*, vol. 805, 2021, Page 140624, Elsevier.

[MUR 11] Murugesan S., Kuppusami P., Mohandas E., Vijayalakshmi M.
X[U+2010]Ray Diffraction Analysis of Defects in Cold Worked Type 316 Stainless Steel. *AIP Conference Proceedings*, vol. 1349 American Institute of Physics, 2011, p. 485–486. Issue: 1.

[MUR 12] Murugesan S., Kuppusami P., Mohandas E., Vijayalakshmi M.
X-ray diffraction Rietveld analysis of cold worked austenitic stainless steel. vol. 67, n° 1, 2012, p. 173–176. ISBN: 0167-577X Publisher: Elsevier.

[NAD 88] Nadgornyi E.
Dislocation dynamics and mechanical properties of crystals. vol. 31, 1988, p. 1–530. ISBN: 0079-6425 Publisher: Elsevier.

[NOR 08] Norfleet D. M., Dimiduk D. M., Polasik S. J., Uchic M. D., Mills M. J.
Dislocation structures and their relationship to strength in deformed nickel microcrystals. vol. 56, n° 13, 2008, p. 2988–3001. ISBN: 1359-6454 Publisher: Elsevier.

[NYE 53] Nye J. F.
Some geometrical relations in dislocated crystals. vol. 1, n° 2, 1953, p. 153–162.

[PAN 08] Pantleon W.
Resolving the geometrically necessary dislocation content by conventional electron backscattering diffraction. *Scripta Materialia*, vol. 58, n° 11, 2008, p. 994–997, Elsevier.

[PET 53a] Petch N. J.
The cleavage strength of polycrystals. vol. 174, 1953, p. 25–28.

[PET 53b] Petch N. J.
J iron steel inst. vol. 174, n° 1, 1953, p. 25–8.

[PIC 14a] Picard Y. N., Liu M., Lammatao J., Kamaladasa R., De Graef M.
Theory of dynamical electron channeling contrast images of near-surface crystal defects. vol. 146, 2014, p. 71–78. ISBN: 0304-3991 Publisher: Elsevier.

[PIC 14b] PICARD Y., LIU M., LAMMATAO J., KAMALADASA R., DE GRAEF M.
Theory of dynamical electron channeling contrast images of near-surface crystal defects. *Ultramicroscopy*, vol. 146, 2014, p. 71–78, Elsevier.

[PRI 99] PRIOR D.
Problems in determining the misorientation axes, for small angular misorientations, using electron backscatter diffraction in the SEM. *Journal of Microscopy*, vol. 195, n° 3, 1999, p. 217–225, Wiley Online Library.

[PUS 13] PUSHKAREVA I., SCOTT C. P., GOUNÉ M., VALLE N., REDJAÏMIA A., MOULIN A.
Distribution of carbon in martensite during quenching and tempering of dual phase steels and consequences for damage properties. vol. 53, n° 7, 2013, p. 1215–1223. ISBN: 0915-1559 Publisher: The Iron and Steel Institute of Japan.

[RÉT 18] RÉTHORÉ J.
UFreckles (version v 2.0). Zenodo. , 2018.

[RUG 18] RUGGLES T., BOMARITO G., QIU R., HOCHHALTER J.
New levels of high angular resolution EBSD performance via inverse compositional Gauss–Newton based digital image correlation. *Ultramicroscopy*, vol. 195, 2018, p. 85–92, Elsevier.

[RUG 20] RUGGLES T. J., YOO Y. S. J., DUNLAP B. E., CRIMP M. A., KACHER J.
Correlating results from high resolution EBSD with TEM-and ECCI-based dislocation microscopy: Approaching single dislocation sensitivity via noise reduction. vol. 210, 2020, Page 112927. ISBN: 0304-3991 Publisher: Elsevier.

[RUS 31] RUSKA E., KNOLL M.
Die magnetische Sammelspule für schnelle Elektronenstrahlen. vol. 12, 1931, p. 389–400.

[SAK 88] SAKAI T., OHASHI M., CHIBA K., JONAS J.
Recovery and recrystallization of polycrystalline nickel after hot working. *Acta Metallurgica*, vol. 36, n° 7, 1988, p. 1781–1790, Elsevier.

[SCH 09] SCHWARTZ A. J., KUMAR M., ADAMS B. L., FIELD D. P.
Electron backscatter diffraction in materials science, vol. 2. Springer, 2009.

[SCH 12] SCHINDELIN J., ARGANDA-CARRERAS I., FRISE E., KAYNIG V., LONGAIR M., PIETZSCH T., PREIBISCH S., RUEDEN C., SAALFELD S., SCHMID B. et al.
Fiji: an open-source platform for biological-image analysis. *Nature methods*, vol. 9, n° 7, 2012, p. 676–682, Nature Publishing Group.

[SHA 20] SHAMSUJJOHA M.
Evolution of microstructures, dislocation density and arrangement during deformation of low carbon lath martensitic steels. vol. 776, 2020, Page 139039. ISBN: 0921-5093 Publisher: Elsevier.

[SHA 21] SHANG C., SELVIDGE J., HUGHES E., NORMAN J. C., TAYLOR A. A., GOSSARD A. C., MUKHERJEE K., BOWERS J. E.
A Pathway to Thin GaAs Virtual Substrate on On-Axis Si (001) with Ultralow Threading Dislocation Density. vol. 218, n° 3, 2021, Page 2000402. _eprint: https://onlinelibrary.wiley.com/doi/pdf/10.1002/pssa.202000402.

[SHI 19] SHI Q., ROUX S., LATOURTE F., HILD F.
Estimation of elastic strain by integrated image correlation on electron diffraction patterns. *Ultramicroscopy*, vol. 199, 2019, p. 16–33, Elsevier.

[SID 21] Sidor J. J., Chakravarty P., Bátorfi J. G., Nagy P., Xie Q., Gubicza J.
Assessment of Dislocation Density by Various Techniques in Cold Rolled 1050 Aluminum Alloy. vol. 11, n° 10, 2021, Page 1571. ISBN: 2075-4701 Publisher: MDPI.

[SIM 96] Simkin B. A., Crimp M. A.
Dislocation detection depth measurements in silicon using electron channelling contrast imaging. , 1996.

[SIN 06a] Sinclair C. W., Poole W. J., Bréchet Y.
A model for the grain size dependent work hardening of copper. vol. 55, n° 8, 2006, p. 739–742. ISBN: 1359-6462 Publisher: Elsevier.

[SIN 06b] Sinclair C., Poole W., Bréchet Y.
A model for the grain size dependent work hardening of copper. vol. 55, n° 8, 2006, p. 739–742. Publisher: Elsevier.

[SIN 17] Singh S., Ram F., De Graef M.
EMsoft: open source software for electron diffraction/image simulations. vol. 23, 2017, p. 212–213. ISBN: 1431-9276 Publisher: Cambridge University Press.

[SPE 72] Spencer J. P., Humphreys C. J., Hirsch P. B.
A dynamical theory for the contrast of perfect and imperfect crystals in the scanning electron microscope using backscattered electrons. vol. 26, n° 1, 1972, p. 193–213. ISBN: 0031-8086 Publisher: Taylor & Francis.

[SPE 80] Spencer J. P., Humphreys C. J.
A multiple scattering transport theory for electron. vol. 42, n° 4, 1980, p. 433–451. ISBN: 0141-8610 Publisher: Taylor & Francis.

[SUN 00] Sun S., Adams B., King W.
Observations of lattice curvature near the interface of a deformed aluminium bicrystal. *Philosophical Magazine A*, vol. 80, n° 1, 2000, p. 9–25, Taylor & Francis.

[TAY 34] Taylor G. I.
The mechanism of plastic deformation of crystals. Part I.—Theoretical. vol. 145, n° 855, 1934, p. 362–387. ISBN: 0950-1207 Publisher: The Royal Society London.

[TOL 07] Tolédano J.-C.
Bases physiques de la plasticité des solides. Editions Ecole Polytechnique, 2007.

[UNG 84] Ungar T., Mughrabi H., Rönnpagel D., Wilkens M.
X-ray line-broadening study of the dislocation cell structure in deformed [001]-orientated copper single crystals. *Acta Metallurgica*, vol. 32, n° 3, 1984, p. 333–342, Elsevier.

[UNG 01] Ungár T., Gubicza J., Ribárik G., Borbély A.
Crystallite size distribution and dislocation structure determined by diffraction profile analysis: principles and practical application to cubic and hexagonal crystals. vol. 34, n° 3, 2001, p. 298–310. ISBN: 0021-8898 Publisher: International Union of Crystallography.

[VAN 71] Van Essen C., Schulson E. M., Donaghay R. H.
The generation and identification of SEM channelling patterns from 10 µm selected areas. vol. 6, n° 3, 1971, p. 213–217. ISBN: 1573-4803 Publisher: Springer.

[VAN 17] Van Bohemen S. M. C., Morsdorf L.
Predicting the Ms temperature of steels with a thermodynamic based model including the effect of the prior austenite grain size. vol. 125, 2017, p. 401–415. ISBN: 1359-6454 Publisher: Elsevier.

[VEN 98] Venkatesh V., Rack H.
Elevated temperature hardening of INCONEL 690. *Mechanics of Materials*, vol. 30, n° 1, 1998, p. 69–81, Elsevier.

[VER 18] Vermeij T., Hoefnagels J.
A consistent full-field integrated DIC framework for HR-EBSD. *Ultramicroscopy*, vol. 191, 2018, p. 44–50, Elsevier.

[WAN 16] Wang A., De Graef M.
Modeling dynamical electron scattering with Bethe potentials and the scattering matrix. vol. 160, 2016, p. 35–43. ISBN: 0304-3991 Publisher: Elsevier.

[WAU 15] Wauthier-Monnin A., Chauveau T., Castelnau O., Réglé H., Bacroix B.
The evolution with strain of the stored energy in different texture components of cold-rolled IF steel revealed by high resolution X-ray diffraction. vol. 104, 2015, p. 31–41. ISBN: 1044-5803 Publisher: Elsevier.

[WHE 09] Wheeler J., Mariani E., Piazolo S., Prior D., Trimby P., Drury M.
The weighted Burgers vector: a new quantity for constraining dislocation densities and types using electron backscatter diffraction on 2D sections through crystalline materials. *Journal of microscopy*, vol. 233, n° 3, 2009, p. 482–494, Wiley Online Library.

[WIL 93] Wilkinson A. J., Anstis G. R., Czernuszka J. T., Long N. J., Hirsch P. B.
Electron channelling contrast imaging of interfacial defects in strained silicon-germanium layers on silicon. vol. 68, n° 1, 1993, p. 59–80. ISBN: 0141-8610 Publisher: Taylor & Francis.

[WIL 96] Williams D. B., Carter C. B.
The transmission electron microscope. *Transmission electron microscopy*, p. 3–17 Springer, 1996.

[WIL 06] Wilkinson A. J., Meaden G., Dingley D. J.
High-resolution elastic strain measurement from electron backscatter diffraction patterns: new levels of sensitivity. vol. 106, n° 4, 2006, p. 307–313. ISBN: 0304-3991 Publisher: Elsevier.

[WIL 10] Wilkinson A. J., Randman D.
Determination of elastic strain fields and geometrically necessary dislocation distributions near nanoindents using electron back scatter diffraction. *Philosophical magazine*, vol. 90, n° 9, 2010, p. 1159–1177, Taylor & Francis.

[WIN 07] Winkelmann A., Trager-Cowan C., Sweeney F., Day A. P., Parbrook P.
Many-beam dynamical simulation of electron backscatter diffraction patterns. vol. 107, n° 4, 2007, p. 414–421. ISBN: 0304-3991 Publisher: Elsevier.

[WIN 10] Winkelmann A.
Principles of depth[U+2010]resolved Kikuchi pattern simulation for electron backscatter diffraction. vol. 239, n° 1, 2010, p. 32–45. ISBN: 0022-2720 Publisher: Wiley Online Library.

[YAM 21] Yamasaki S., Deguchi M., Mitsuhara M., Nakashima H., Ota Y., Kubushiro K.
Evaluation of depth of dislocation visibility in SEM electron channeling contrast imaging in Ti-6Al-4V alloy using serial sectioning method. vol. 70, n° 3, 2021, p. 265–277. ISBN: 2050-5698 Publisher: Oxford University Press UK.

[ZAE 00] Zaefferer S.
New developments of computer-aided crystallographic analysis in transmission electron mi-

croscopy. vol. 33, n° 1, 2000, p. 10–25. ISBN: 0021-8898 Publisher: International Union of Crystallography.

[ZAE 14] Zaefferer S., Elhami N.-N.
Theory and application of electron channelling contrast imaging under controlled diffraction conditions. vol. 75, 2014, p. 20–50.

[ZHA 21] Zhang X., Wang P., Li D., Li Y.
Multi-scale study on the heterogeneous deformation behavior in duplex stainless steel. *Journal of Materials Science & Technology*, vol. 72, 2021, p. 180–188, Elsevier.

[ZHE 15] Zheng C., Li L., Wang Y., Yang W., Sun Z.
Micromechanical behavior of eutectoid steel quantified by an analytical model calibrated by in situ synchrotron-based X-ray diffraction. *Materials Science and Engineering: A*, vol. 631, 2015, p. 181–188, Elsevier.

[ZHI 20] Zhi H., Zhang C., Antonov S., Yu H., Guo T., Su Y.
Investigations of dislocation-type evolution and strain hardening during mechanical twinning in Fe-22Mn-0.6 C twinning-induced plasticity steel. *Acta Materialia*, vol. 195, 2020, p. 371–382, Elsevier.

[ZRI 19] Zribi Z., Ktari H. H., Herbst F., Optasanu V., Njah N.
EBSD, XRD and SRS characterization of a casting Al-7wt%Si alloy processed by equal channel angular extrusion: Dislocation density evaluation. vol. 153, 2019, p. 190–198.

FOLIO ADMINISTRATIF

THESE DE L'INSA LYON, MEMBRE DE L'UNIVERSITE DE LYON

NOM : Gallet

DATE de SOUTENANCE : Le 06 mars 2023

Prénoms : Julien

TITRE : Towards an automated dislocation density measurement in the SEM: benefits and limits of the R-ECCI method

NATURE : Doctorat

Numéro d'ordre : 2023ISAL0017

Ecole doctorale : ED Matériaux

Spécialité : Matériaux

RESUME :

In order to predict the mechanical behavior of metallic materials, it is important to determine several physical quantities, including the dislocation density which has a major impact on mechanical properties. Recent work has shown that it is possible to make these observations using a Scanning Electron Microscope. Indeed, this method has the advantage of being applied on bulk samples and of allowing the observation of larger areas. However, a sample orientation step is necessary, and the image processing is done manually. This makes the approach long and tedious. The R-ECCI method is based on the acquisition of a series of images at different rotation angles and allows to avoid the sample orientation step. An intensity profile is obtained, which is representative of the nature of the considered pixel (dislocation, defect or matrix).

The objective of this thesis project was to develop a method of automatic characterization of the dislocation density, using a clustering type algorithm applied on the profiles. The images are processed in an automated way and the dislocation density is calculated. The first part of the project focused on the development of the image acquisition methodology and the data processing software and allowed to determine the limits and the strengths of the method. In a second part, a quantitative comparison with existing measurement methods (TEM, DRX, HR EBSD ...) was performed. In addition to the fact that each of these methods does not detect the same populations of dislocations, complementary results in terms of limits of detectability have been obtained. Finally, results obtained on a known alloy were compared to those obtained by a micro-mechanical prediction model, and a good compromise was found, which allows to validate the global approach of R-ECCI.

MOTS-CLÉS : ECCI, density dislocation, clustering.

Laboratoire (s) de recherche :
MatéIS - UMR CNRS 5510 - INSA de Lyon
25 avenue Jean Capelle
69621 Villeurbanne Cedex (FRANCE)

Directeur de thèse : Michel Perez (Professeur INSA-Lyon) , Sophie Cazottes (Maître de conférence INSA-Lyon) et Thibaut Chaise (Maître de conférence INSA-Lyon)

Président de jury : Xavier Sauvage (Professeur Univ. Rouen, Président)

Composition du jury : Muriel Véron (Professeur Univ. Grenoble Alpes, Rapporteur)
Alexandre Mussi (Maître de Conférence Univ. Lille, Rapporteur)